

Louisiana Tech University

Louisiana Tech Digital Commons

Doctoral Dissertations

Graduate School

Spring 5-2023

Peptide Carriers to Improve Uptake and Functionality and to Cross BBB to Arrest Secondary Injury Post TBI

Yashwanthi Yanamadala

Follow this and additional works at: <https://digitalcommons.latech.edu/dissertations>

**PEPTIDE CARRIERS TO IMPROVE UPTAKE AND
FUNCTIONALITY AND TO CROSS BBB TO
ARREST SECONDARY INJURY POST TBI**

by

Yaswanthi Yanamadala, B.S. M.S.

A Dissertation Presented in Partial Fulfillment
of the Requirements for the Degree
Doctor of Philosophy

COLLEGE OF ENGINEERING AND SCIENCE
LOUISIANA TECH UNIVERSITY

May 2023

LOUISIANA TECH UNIVERSITY

GRADUATE SCHOOL

November 15, 2022

Date of dissertation defense

We hereby recommend that the dissertation prepared by

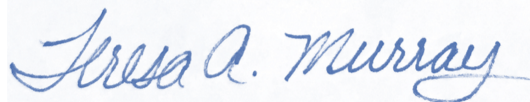
Yashvanthi Yanamada, B.S., M.S.

entitled **Peptide Carriers to Improve Uptake and Functionality and to Cross**

BBB to Arest Secondary Injury Post TBI

be accepted in partial fulfillment of the requirements for the degree of

Doctor of Philosophy in Molecular Sciences and Nanotechnology



Teresa Ann Murray

Supervisor of Dissertation Research



Gergana Nestorova

Head of Molecular Sciences and Nanotechnology

Doctoral Committee Members:

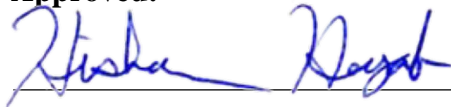
Prabhu Arumugam

Gergana Nestorova

Yuri Lvov

David K. Mills

Approved:



Hisham Hegab

Dean of Engineering & Science

Approved:



Ramu Ramachandran

Dean of the Graduate School

ABSTRACT

Cell-penetrating peptides (CPP) possess the ability to transport different cargos efficiently across the cell membrane. In this study, the ability of a CPP to cross the blood-brain barrier (BBB) and stably carry therapeutic components across the plasma membrane was assessed. The therapeutic efficacies were determined by the ability of the KFAK conjugated anti-inflammatory peptide drug to inhibit the progression of secondary neuronal damage in a traumatic brain injury (TBI) model at 7-day post-injury (DPI) by inhibiting the production of inflammatory cytokines. A related study with minocycline and Pgp-rolipram was conducted to improve the outcome in TBI models at 14 DPI. Similarly, the ability of halloysite nanotubes (HNTs) to cross the BBB was investigated. Improving the BBB-crossing carrier library is the primary objective of this study, which seeks to identify reliable carrier molecules that can transport therapeutic compounds to the brain to treat brain injury and disorders.

Initially, two peptides were synthesized: (1) an anti-inflammatory peptide (AIP-1) that specifically target the MK2 pathway (mitogen-activated protein kinase) to regulate the inflammatory response (control), and (2) KFAK, a CPP conjugated to AIP-1. The intracellular delivery, therapeutic efficacy, and cytotoxicity of these peptides were compared in rodent primary BBB cells (primary brain microvascular endothelial cells (BMVEC's)) and four cell lines (macrophages (RAW, J774), neuronal cells (SHEP-1),

and hepatocytes (HEP G2)). KAFAK did not induce cell toxicity at concentrations below 250 μM in primary BMVEC cells and below 1000 μM in the cell lines. Subsequently, the CPP conjugate was validated in vivo for its uptake and localization in the brain and its therapeutic efficacy in a TBI mouse model following non-invasive intranasal administration for six days. The results showed that KAFAK was primarily localized in the olfactory bulbs. Some diffused throughout the cortex, and it reduced cytokine (IL-1 β , IL-6, and TNF- α) production in TBI mice as compared to vehicle-treated mice.

Halloysite nanotubules (HNTs), naturally available nanoparticles, were also explored for their ability to penetrate the BBB. HNTs were loaded with rhodamine isothiocyanate (RITC) to determine their uptake and localization in the brain at 4, 24, and 48 hours after a single noninvasive intranasal administration. Another group of mice received HNTs loaded with diazepam intranasally for six days and was evaluated for behavioral changes versus mice that received HNTs alone. Fluorescence from RITC was observed in the brain tissue of mice treated intranasally with HNTs loaded with RITC but not in mice treated with RITC alone. The intensity of fluorescence decreased over time, and no HNTs-associated behavioral changes were observed. Mice treated with HNT-diazepam exhibited diazepam-associated behavioral changes, indicating that HNTs could penetrate the BBB and release the drug into the brain. In summary, HNTs and CPPs have demonstrated that they have the potential to transport drugs across the BBB.

APPROVAL FOR SCHOLARLY DISSEMINATION

The author grants to the Prescott Memorial Library of Louisiana Tech University the right to reproduce, by appropriate methods, upon request, any or all portions of this Dissertation. It is understood that “proper request” consists of the agreement, on the part of the requesting party, that said reproduction is for his personal use and that subsequent reproduction will not occur without written approval of the author of this Dissertation. Further, any portions of the Dissertation used in books, papers, and other works must be appropriately referenced to this Dissertation.

Finally, the author of this Dissertation reserves the right to publish freely, in the literature, at any time, any or all portions of this Dissertation.

Author _____

Date _____

DEDICATION

This dissertation is dedicated to Amma, Daddy, Pranith, my grandparents (thathagaru, papamm(A), and Teja for their unwavering patience and support and for being my everlasting sources of strength and love, also, to my adoring son Karthi, whose endearing smile has been a stress reliever. With the deepest gratitude, I would dedicate this to my PI, Dr. Murray, as none of this would have been possible without her.

TABLE OF CONTENTS

ABSTRACT.....	iii
APPROVAL FOR SCHOLARLY DISSEMINATION	v
DEDICATION	vi
LIST OF FIGURES	xv
LIST OF TABLES	xxiv
ACKNOWLEDGMENTS	xxv
CHAPTER 1 INTRODUCTION	1
1.1 Research Need	1
1.2 Current State of Research	2
1.3 Research Hypothesis and Specific Aims	4
CHAPTER 2 BACKGROUND	6
2.1 Traumatic Brain Injury	6
2.1.1 Primary and Secondary Brain Injury	7
2.1.2 Diffuse Axonal Injury in TBI	8
2.1.3 Role of Inflammation in TBI	10
2.1.4 Blood Brain Barrier Disruption in TBI.....	11
2.2 Therapeutics and Carriers to Shuttle Drugs Across BBB to Treat TBI.....	13
2.2.1 Current Strategies in TBI.....	13
2.2.2 Drug Repurposing	14

2.2.3 CPP Carriers to the Brain.....	16
2.2.4 Nanoparticle Carriers	19
2.3 Animal Models in Brain Injuries	20
CHAPTER 3 SYNTHESIS, CHARACTERIZATION, AND OPTIMIZATION OF THE DRUGS FOR BBB PENETRATION CLINICALLY RELEVANT ROUTES OF ADMINISTRATION	21
3.1 Choice of Drugs for the Study	21
3.2 Synthesis of Peptides by Solid Phase Peptide Synthesis	24
3.2.1 Deprotection.....	27
3.2.2 Coupling Amino Acid Residues	29
3.2.3 Incoming Amino Acid Activation and Acylation of the Amino Group	29
3.2.4 Washing and Filtration.....	30
3.2.5 Labeling with Fluorescent Dye	30
3.2.6 Cleavage of the Peptide from the Resin and Isolation.....	31
3.2.7 Removal of TFA Acetate Counter Ion.....	32
3.3 Characterization of Peptide.....	33
3.4 Synthesis of Nanoparticles and Rolipram Loading for 14-Day Trial	39
3.5 Synthesis of Halloysite Nanotubules and Loading Them with Diazepam and Ritc Dye	41
3.5.1 Thermogravimetric Analysis	42
3.6 Drug Administration Routes and Considerations	44
3.6.1 Anatomy and Rationale for Intranasal Administration.....	47
CHAPTER 4 CELL-PENETRATING MK2 INHIBITORY PEPTIDE BLOCKS LPS-INDUCED EXPRESSION OF PRO-INFLAMMATORY CYTOKINES IN HEPG2 HEPATOCYTES.....	50
4.1 Abstract.....	50

4.2 Extended Abstract.....	51
4.3 Introduction.....	52
4.4 Methods.....	53
4.4.1 Anti-inflammatory Peptide Synthesis	53
4.4.2 Cell Culture.....	54
4.4.3 Cell Viability.....	55
4.4.4 RNA Isolation and RT-qPCR	55
4.4.5 ELISA	56
4.4.6 Fluorescence Microscopy	57
4.4.7 Statistical Analysis.....	57
4.5 Results.....	57
4.5.1 Cell Viability.....	57
4.5.2 Gene Expression	58
4.5.3 ELISA	60
4.5.4 Intracellular Uptake	61
4.6 Discussion.....	63
CHAPTER 5 CELL PENETRATING ANTI-INFLAMMATORY PEPTIDE (KAFAK) PROMOTES EFFICIENT UPTAKE AND INHIBITION OF PRO-INFLAMMATORY CYTOKINES IN PRIMARY BRAIN CELLS IN VITRO: A PROMISING CNS CANDIDATE	65
5.1 Introduction.....	65
5.2 Materials and Methods.....	69
5.2.1 Materials.	69
5.2.2 Animal Care.....	69
5.2.3 Harvesting Primary Cells.....	69

5.2.4 Cell Culture.....	70
5.2.5 Peptide Uptake and Localization	70
5.2.6 ATP Assay	71
5.2.7 Quantification of Intensity	71
5.3 Results.....	72
5.3.1 Fluorescent Peptide Internalization.....	72
5.3.2 Quantification of Peptide Uptake.....	77
5.3.3 Cell Viability.....	78
5.4 Discussion.....	79
CHAPTER 6 CELL PENETRATING ANTI-INFLAMMATORY PEPTIDE (KAFAK) EFFICIENTLY CIRCUMVENT THE BLOOD BRAIN BARRIER AND CURTAIL THE INFLAMMATION IN TRAUMATIC BRAIN INJURY MICE MODEL IN VIVO	81
6.1 Abstract.....	81
6.2 Introduction.....	82
6.3 Materials and Methods.....	84
6.3.1 Materials	84
6.3.2 Animal Preparation and Handling	85
6.3.3 Surgeries for Mice.....	85
6.3.4 Midline Fluid Percussion Injury (mFPI).....	88
6.3.5 Administration of the Drug.....	90
6.3.6 Behavioral Test	92
6.3.7 Rotarod.....	93
6.3.8 Modified Neurological Severity Score (mNSS)	95
6.3.9 Open Field (OF).....	96

6.3.10 Novel Object Recognition (NOR)	97
6.3.11 Elevated Plus Maze (EPM)	98
6.3.12 Video Analysis.....	99
6.3.13 Extraction and Processing Brains	99
6.3.14 Cryo-Preservation of Brains	100
6.3.15 Sectioning of Brains for Visualization of Peptide	101
6.3.16 Slide Preparation	102
6.3.17 Imaging of Sample.....	103
6.3.18 Cytokine Assay	103
6.3.18.1 Homogenization of Brain Sample.....	103
6.3.18.2 Protein Assay	103
6.3.18.3 Enzyme-linked Immunosorbent Assay (ELISA) Test	104
6.3.19 Statistical Analysis.....	104
6.4 Results.....	105
6.4.1 Preliminary Uptake Studies	105
6.4.2 Rotarod.....	107
6.4.3 Modified Neurological Severity Score	109
6.4.4 Weights of Mice.....	110
6.4.5 Elevated Plus Maze.....	110
6.4.6 Novel Object Recognition.....	111
6.4.7 Cytokine Assay	114
6.4.8 Power Analysis	114
6.4.9 ELISA	115

6.5 Discussion.....	116
CHAPTER 7 DIAZEPAM LOADED CLAY NANOTUBES PERMEATE THE BRAIN THROUGH INTRANASAL ADMINISTRATION AND SHOWS NO BEHAVIORAL CHANGES IN MICE.....	118
7.1 Abstract.....	118
7.2 Introduction.....	118
7.3 Materials and Methods.....	122
7.3.1 Materials	122
7.3.2 Preparation of HNTs	123
7.3.3 Preparation of HNTS with RITC and Diazepam	123
7.3.4 TGA	124
7.3.5 Animal Care and Handling	124
7.3.6 Intranasal Administration.....	125
7.3.7 Intraperitoneal Administration.....	125
7.3.8 Rotarod Test.....	126
7.3.9 Modified Neurological Severity Score (mNSS)	126
7.3.10 Open Field (OF).....	126
7.3.11 Elevated Plus Maze (EPM).....	127
7.3.12 Novel Object Recognition (NOR)	127
7.3.13 Behavioral Video Analysis (MATLAB).....	128
7.3.14 Perfusion and Extraction of Brain.....	128
7.3.15 Vibratome Sectioning	129
7.3.16 Preparation of Samples for Imaging	130
7.3.17 Imaging	130

7.4 Results.....	130
7.4.1 Rotarod Score.....	135
7.4.2 Modified Neurological Severity Score	136
7.4.3 Weights of the Mice.....	137
7.4.4 Elevated Plus Maze.....	138
7.4.5 Novel Object Recognition.....	138
7.4.6 Open Field.....	139
7.4.7 TGA	140
7.5 Discussion.....	141
CHAPTER 8 SYNERGETIC EFFECT OF MINOCYCLINE AND ROLIPRAM TO ARREST PROGRESSION OF SECONDARY INJURY POST TBI IN RODENT MODELS	143
8.1 Introduction.....	143
8.1.1 Materials and Methods.....	144
8.1.1.1 Treatments.....	144
8.2 Results.....	145
8.2.1 Behavioral Analysis.....	145
8.2.2 Rotarod.....	146
8.2.3 Mnss.....	147
8.2.4 EPM	147
8.2.5 NOR	148
8.2.6 IHC Staining	149
8.3 Discussion.....	151
CHAPTER 9 CONCLUSIONS AND FUTURE WORK.....	153

9.1 Additional Work	156
9.1.1 Implanting Silicone Probes for Detection of Glutamate and GABA.....	156
APPENDIX A REAGENT RECIPES	158
REFERENCES	160

LIST OF FIGURES

Figure 2-1: Schematic of the response of the brain to traumatic brain injury. The candidate drugs discussed in this review exert their effects through inhibiting specific injury pathways that are activated post-TBI. BBB= blood-brain-barrier; ROS=reactive oxygen species [62].....	15
Figure 2-2: Coronal cross section of blood brain barrier showing transport mechanisms [56]	18
Figure 3-1: Illustration of N-terminus peptide synthesis using solid phase peptide vessel under inert atmosphere.	25
Figure 3-2: Illustrates solid phase peptide synthesis steps using Fmoc chemistry. The deprotection process contains piperidine to remove the Fmoc protective group from the resin or amino acids, allowing for the attachment of the subsequent amino acid. Followed by a coupling reaction along with activators for next amino acid addition. Once the complete chain has been produced, the peptide is separated from the resin using TFA.	27
Figure 3-3: A. Fmoc group. B. Rink Amide resin protected at the NH group by Fmoc (represented as (F)).	28
Figure 3-4: Deprotection of the N-Fmoc group of an amino acid using piperidine. After deprotection, the primary adducts and dibenzofulvene intermediates are produced.....	28
Figure 3-5: AIP-1 peptide HPLC data demonstrating the purity of the peptide synthesized after lyophilization. A gradient of water and acetonitrile was employed to elute the peptide. The sample peak was isolated and sent for MALDI-TOF MS, which showed a pure sample. KAFK, R8, and AIP were synthesized in the lab and purchased from AAPTEC (AIP-FITC) and Biomatik, as described in earlier chapters (KAFK-FITC, KAFK-RITC).....	34
Figure 3-6: MALDI-TOF MS spectrum of anti-inflammatory peptide (AIP-1) unprotected peptide sequence FITC-Ahx-NH-KKKALNRQLGVAA-COOH. Expected mass: 1857.13, analyzed mass: 1858.13 (aaptec)	35

Figure 3-7: MALDI-TOF MS spectrum of anti-inflammatory peptide (AIP-1) peptide sequence KKKALNRQLGVAA-COOH. Expected mass: 1418, analyzed mass: 1417.83 (LSU, Baton Rouge)	36
Figure 3-8: MALDI-TOF MS spectrum of CPP+anti-inflammatory peptide (RITC- KAFAK) peptide sequence rhodamine RITC-KAFAKLAARLYRKALARQLGVAA. Expected mass: 2911.59 (Biomatik).....	37
Figure 3-9: MALDI-TOF MS spectrum of CPP+anti-inflammatory peptide (FITC-KAFAK) peptide sequence FITC-Ahx-KAFAKLAARLYRKALARQLGVAA. Expected mass: 2989.95 (Biomatik)	37
Figure 3-10: MALDI-TOF MS spectrum of CPP+anti-inflammatory peptide (FITC-KAFAK) peptide sequence FITC-Ahx-KAFAKLAARLYRKALARQLGVAA. Expected mass: 2989.95 (LSU, Baton Rouge)..	38
Figure 3-11: MALDI-TOF MS spectrum of R8 peptide sequence RRRRRRRR Expected mass: 1488.76 (LSU, Baton Rouge)	39
Figure 3-12: Rhodamine Isothiocyanate release profile using 10 mL of endothelial cell culture media, 3.3 mg of HNT-rhodamine was taken and stirred at 250 rpm for 24 hrs. Readings were taken after 1, 4, 8, and 24 hrs. Displays the rate at which the dye is released over a period of 24 hs.	41
Figure 3-13: (A) TEM and (B) SEM images of Halloysite nanotubes. The images were acquired by Mahdi Saleh (Dr. Yuri Lvov Lab, Louisiana Tech University).	42
Figure 3-14: Thermogravimetric curves of pristine halloysite with no material loaded inside burns at roughly 450-500 °C. The images were acquired by Mahdi Saleh (Dr. Yuri Lvov Lab, Louisiana Tech University).	43
Figure 3-15: Thermogravimetric curves of diazepam loaded inside halloysite displaying the drug burning at 350-400 °C and halloysite at 450-500 °C. The images were acquired by Mahdi Saleh (Dr. Yuri Lvov Lab, Louisiana Tech University).	43
Figure 3-16: Thermogravimetric curves of RITC loaded inside halloysite displaying the substance burning at 350-400 °C and halloysite at 450-500 °C. The images were acquired by Mahdi Saleh (Dr. Yuri Lvov Lab, Louisiana Tech University).	44
Figure 3-17: The mechanism of transport of therapeutic molecules across the BBB [122]. Abbreviations: Cell penetrating peptide (CPP), tight-junction (TJ), monoclonal antibody (mAB), conventional enhanced delivery (CED), P-glycoprotein (P-gp).....	45

- Figure 3-18:** Intranasal drug transport pathways in rodents and the anatomy of the rodent nasal cavity [130]. Different color arrows indicate the routes that the yellow substance travels to reach different brain regions, including the hippocampus, the hindbrain, and 3rd and 4th ventricles after IN administration.48
- Figure 4-1:** Cellular ATP was assayed as a measure of cell viability after 24-hour treatment with the indicated concentrations of peptides. Data are expressed as % of untreated control. (* indicates $p < 0.0001$). $n = 3$ 58
- Figure 4-2:** The suitability of three potential reference genes was assessed by RT-qPCR after 24 hour incubation with the indicated treatments (100 μ M AIP-1, 100 μ M CPP-AIP-1, 1 ng/mL LPS, or combination). $n = 3$59
- Figure 4-3:** Expression of CXCL8 (left) and TNF (right) mRNA was quantified by RT- qPCR after 24 hour incubation with the indicated treatments (100 μ M AIP-1, 100 μ M CPP-AIP-1, 1 ng/mL LPS, or combination). Data are normalized to 3 reference genes and expressed as relative fold-change of untreated control (horizontal dash represents control expression). Bars with different letters indicate a statistically significant difference ($p < 0.05$). $n = 3$ 60
- Figure 4-4:** Secreted CXCL8 was quantified by ELISA after 24-hour incubation with the indicated treatments (100 μ M AIP-1, 100 μ M CPP-AIP-1, 1 ng/mL LPS, or combination). Data are expressed as relative fold-change of untreated control (horizontal dash represents control level). Bars with different letters indicate a statistically significant difference ($p < 0.05$). $n = 3$ 61
- Figure 4-5:** Fluorescence image reader (Biotek- Cytation image reader)62
- Figure 4-6:** Fluorescence images of HEP G2 cells treated with 200 μ M concentration AIP-1 (left image), KAFK-AIP-1 (CPP conjugate) (middle image), and R8 (positive control) (right image) for 4hours. AIP-1 treated cells showed no uptake of the peptide while KAFK-AIP-1 showed enhanced uptake. R8 at this concentrations has shown high cytotoxicity in the cells.62
- Figure 4-7:** J774 (macrophages), RAW (macrophages), and SHEP (neuronal cells) treated with 200 μ M concentrations of AIP-1 (first row), KAFK-AIP-1 (CPP conjugate) (second row), and R8 (positive control) (third row) for 4 hours. AIP-1 treated cells exhibited less peptide absorption than KAFK treated cells, although R8 at the dose exhibited severe cytotoxicity in the cells.63

Figure 5 -1: Fluorescein-labeled peptide FI-KAFAK uptake in primary BMVEC cells after 4 hours of treatment. Representative images are shown, and each row depicts the same cells. Panels A, B, and C are images of cells treated with 20 μM of FITC-KAFAK, panels D, E, and F were treated with 30 μM , G, H, and I with 50 μM , and panels J, K, and L with 75 μM . The first column (A, D, G, J) are phase contrast images, the second column (B, E, H, K) are images acquired with the DAPI filter to visualize nuclei stained with DAPI, and the third column (C, F, I, L) are images acquired with the GFP filter. The length of the scale bar is 30 μm73

Figure 5-2: Fluorescein-labeled peptide FI-L57-AIP uptake in primary BMVEC cells after 4 hours of treatment. Representative images are shown, and each row depicts the same cells. Panels A, B, and C are images of cells treated with 20 μM of FITC-KAFAK, panels D, E, and F were treated with 30 μM , G, H, and I with 50 μM , and panels J, K, and L with 75 μM . The first column (A, D, G, J) are phase contrast images, the second column (B, E, H, K) are images acquired with the DAPI filter to visualize nuclei stained with DAPI, and the third column (C, F, I, L) are images acquired with the GFP filter. The length of the scale bar is 30 μm74

Figure 5-3: Fluorescein-labeled peptide FI-AIP uptake in primary BMVEC cells after 4 hours of treatment. Representative images are shown, and each row depicts the same cells. Panels A, B, and C are images of cells treated with 20 μM of FITC-KAFAK, panels D, E, and F were treated with 30 μM , G, H, and I with 50 μM , and panels J, K, and L with 75 μM . The first column (A, D, G, J) are phase contrast images, the second column (B, E, H, K) are images acquired with the DAPI filter to visualize nuclei stained with DAPI, and the third column (C, F, I, L) are images acquired with the GFP filter. The length of the scale bar is 30 μm75

Figure 5-4: Representative images of the uptake levels FITC-labeled peptides in BMVECs after 4 hours of treatment with varying concentrations. The cells in the first column (A, D, G, J) were treated with FITC-KAFAK, the cells in the second column (B, E, H, K) were treated with FITC-L57-AIP, and the cells in the third column (C, F, I, L) were treated with FITC-AIP. The first row (A, B, C) of cells are treated with respective peptide concentrations of 20 μM , the second row (D, E, F) are treated with concentrations of 30 μM , the third row (G, H, I) are treated with concentrations of 50 μM , and the fourth row (J, K, L) are treated with concentrations of 75 μM . 30 μm is the length of the scale bar.76

Figure 5-5: Three peptides, FITC-KAFAK, FITC-L57-AIP, and FITC-AIP, show concentration-dependent cellular uptake. (A) BMVECs (10,000 per well) treated for 4 hours with 10 μ M, 20 μ M, 30 μ M, 50 μ M, and 75 μ M concentrations of FITC-KAFAK. (B) BMVECs (10,000/well) treated with peptides FITC-KAFAK, FITC-AIP, and FITC- L57-AIP at 50 μ M and 75 μ M concentrations. The mean fluorescence intensity is normalized and plotted. ImageJ software was used to analyze 20 cells per well, for a total of 120 cells (n=6 wells) per concentration of a peptide. * $P > 0.05$; ** $P \leq 0.001$; *** $P < 0.05$ ANOVA with Bonferroni correction with multiple comparisons was used to evaluate the effect of concentration for Panel A and of treatment condition and of concentrations in Panel (B)..	77
Figure 5-6: An ATP assay was used to measure cell viability in BMVECs with the indicated concentrations of peptide for 24 hours. AIP and L57 has not shown cytotoxicity on BMVECs until 500 μ M concentration. KAFAK treated BMVECs at 100 μ M has shown reduced cell viability and decreased viability with the increase in concentration. Data expressed as % of control (n=3) (* 0.0009).	78
Figure 6-1: Surgery table setup for performing craniectomy surgeries on mice.	87
Figure 6-2: Image representing the setup of a mouse on a surgical table, the craniectomy using a trephine to expose the brain dura, and the placement of an injury hub to connect to a fluid percussion instrument for injury.	88
Figure 6-3 Set up of Fluid Percussion Injury (FPI) injury system for achieving mild TBI in mice for the study.	90
Figure 6-4: (A) Intranasal administration of drug to the mouse (B) Intraperitoneal administration of drug to the mouse.	91
Figure 6-5: Configuration of the Rotarod device. During the test, the mice were separated into five lanes, as seen in the image, and their latency is automatically recorded using individual levers.	95
Figure 6-6: Illustrating mNSS tests: (A) represents different rods that were used for testing the mice (B) Hindlimb flexion of the mice.	96
Figure 6-7: Mouse during the open field test as viewed through the camera for recording	97
Figure 6-8: Mouse during the novel object recognition test as viewed through the camera for recording (A) NOR1 with two different objects (B) NOR2, one of the object replaced with the other.	98
Figure 6-9: Mouse during the elevated plus maze test as viewed through the camera for recording	99

Figure 6-10: Illustrating the extraction of mice brain post perfusion from the mice[191].	100
Figure 6-11: (A) Apparatus used for slicing the brains (B) brain glued onto mounting block in the ice cold buffer chamber.	102
Figure 6-12: Fluorescent pictures of brain slices taken with GFP and DAPI filters after 4 hours of treatment with 500 μ M of FI-KAFAK. A, B, and C are images of the olfactory bulb captured with different filters from the same location as D, E, and F from the prefrontal cortex and G, H, and I from the mid-cerebral cortex. The first column (A, D, G) shows brain slice images with the GFP filter, the second column (B, E, H) with DAPI after DAPI counterstaining the tissues, and the third column (C, F, I) with phase contrast images. The scale bar measures 100 μ m.	105
Figure 6-13: After 4 hours of treatment with 500 μ M of FI-KAFAK or Rh-KAFAK, fluorescent images of brain slices captured using GFP, TRITC, and DAPI filters. Images J-O depict the olfactory bulb, while images P,Q, and R depict the cerebral cortex. The pictures in the second column (K, N, Q) were obtained using the DAPI filter, whereas the images in the third column (L, O, R) were merged DAPI with GFP or TRITC images. J, K, and L pictures were taken from the same location but with different filters, similarly (M, N, O) and (P, Q, R). Scale bar for the first row J, K, and L is 31.5 μ m, whereas M-R is 100 μ m.	106
Figure 6-14: Normalised rotarod scores on day 2, 5 and 7. A represents the normalized rotarod data for all the Female mice added to each group, while B is the data of the male mice in the study and C represents the data of all the mice added to the study. Three groups sham (vehicle treatment), TBI, treated (500 μ M KAFAK) (n=8 for each group) are added to the study.	108
Figure 6-15: Normalised mNSS on day 2, 5 and 7. A represents the normalised mNSS for all the Female mice added to each group, while B is the data of the male mice in the study and C represents the data of all the mice added to the study. Three groups sham (vehicle treatment), TBI, treated (500 μ M KAFAK) (n=8 for each group) are added to the study.	109
Figure 6-16: Mean of total distance traveled by mice in each group during EPM test (n=8).	110
Figure 6-17: Mean of percentage time spent on open arm by each treatment group during EPM test (n=8). (* =P< 0.05)	111
Figure 6-18: Traces of mice during the novel object recognition test. Red color represents the familiar object (not changed). Yellow color represents the novel object (changed between the tests)	112

Figure 6-19: Novel object recognition test results on day 7 between sham, TBI and TBI treated with KAFAK peptide. The data (n=8) is represented as mean of discrimination index with ± 2 standard error. (* =P< 0.05)112

Figure 6-20: Open field mouse traces. The pink dots represent the open field's center (region of interest). White dots depict the edges of the open field wall. (A) trace of a mouse that is moderately stressed (eccentric value = 0.91 (in the most of frames) and speed (about 37.6% SAP. (B) Trace of mice that are severely stressed and remained primarily in the corners and along the walls113

Figure 6-21: Open field test results on day 7 between sham, TBI and TBI treated with KAFAK peptide. The data (n=8) is represented as mean of discrimination index with ± 2 standard error. The data is not significantly different.113

Figure 6-22: G*Power window showing the number of samples requires to achieve desired significance for the study.115

Figure 6-23: ELISA was used to quantify brain homogenate samples 12 hours after treatment (24 ul of 500uM concentration-IN and 10% w/v of 500uM concentration-IP). The treated groups differed significantly from the control untreated group (n=5). Standard error (* = P>0.05; ** = P< 0.05).116

Figure 7-1: Fluorescence images of the brain slices of the olfactory bulb at time points 4, 12, 24 and 48 hours after intranasal administration of HNT-Rhodamine. Images A, D, G, J (first column) are phase contrast images. B, E, H, K (second column) are images acquired through DAPI filter and C, F, I, L (third column) are acquired through TRITC filter. Images from A through F were acquired using 10x objective and G through L were imaged through 40x objective.132

Figure 7-2: Fluorescence images of the brain slices of the cortex region at time points 4, 12, 24 and 48 hours after intranasal administration of HNT-Rhodamine. Images A, D, G, J (first column) are phase contrast images. B, E, H, K (second column) are images acquired through DAPI filter and C, F, I, L (third column) are acquired through TRITC filter. Images from M through R were acquired using 10x objective and S through X were imaged through 40x objective. The scale bar is 100 μ m for images S-X and 31.5 μ m for M-R.133

Figure 7-3 Florescence images of the mice brains that were acquired 4 hours after treatment. The first column a1, d1, g1, j1 (first column) are phase contrast images while the second column b1, e1, h1, k1 are images acquired through DAPI filter and third column c1, f1, i1, l1 were acquired using TRITC filter. The first-row images are from the brain after intranasal treatment with HNTs only while second row with intranasal RITC treatment only, third row with intranasal HNT-Rhodamine administration and fourth row was HNT-Rhodamine treatment intraperitoneally. The images were acquired using 40x for a1-i1 and 10x for j1-l1. The scale bar for j1-l1 is 31.5 μ m and a1-i1 is 100 μ m.....134

Figure 7-4: Normalized data showing time of latency to the fall on day 2, 5 and 7. The mice were treated with vehicle (sham), HNTs only, and HNT-diazepam for 6 days. Mice were divided into three treatment groups: sham (n=6), HNT (n=6), and HNT-diazepam (n=6). Using pairwise comparison and Bonferroni correction, a T-test statistical analysis was performed. The data revealed a statistically significant difference between control and HNT-diazepam by day 7 (p=0.002). A and B represents the same data in different graph forms. (* =P< 0.05).135

Figure 7-5: Modified neurological severity scores on day 2, 5 and 7. The mice were treated with vehicle (sham), HNTs only, and HNT-diazepam for 6 days. Mice were divided into three treatment groups: sham (n=6), HNT (n=6), and HNT-diazepam (n=6). Using pairwise comparison and Bonferroni correction, a T-test statistical analysis was performed. The data revealed a statistically significant difference between placebo, HNT, and HNT-diazepam, but no difference between placebo and HNT (p = 1.0). A and B represents the same data in different graph forms. (* =P< 0.05)137

Figure 7-6: Elevated plus maze test results of control, HNT treated, and HNT-diazepam treated mice on day 7. (A) the percentage time spent on the open arm by each group (B) The total distance traveled by the mice in each group (n=6) standard error \pm 2.....138

Figure 7-7: Novel object recognition test results of control, HNT, HNT-diazepam on day 7. The data was represented as mean discriminative index and total time spent on open arms (n=6) standard error \pm 1. (* =P< 0.05).....139

Figure 7-8: Open field results of control, HNT, HNT-diazepam on day 7. The data was represented as mean discriminative index and total time spent on open arms (n=6) standard error \pm 1.140

Figure 8-1: Rotarod normalized mean latency time by each groups on day 2, 5 and 7 (n=10) (* = P>0.05; ** = P< 0.05).....146

Figure 8-2: mNSS normalized score by each group on day 2, 5 and 7 (n=10). (* = P>0.05; ** = P< 0.05).....147

Figure 8-3 Elevated plus maze results of the mice on day 14 between TBI (vehicle) treated and TBI rolipram and minocycline treated.....148

Figure 8-4: Novel object recognition on day 14 across the groups TBI rolipram and minocycline treated, TBI minocycline treated, TBI vehicle treated, TBI rolipram treated, and TBI control. Average time each group spent in proximity to novel versus familiar objects. (* = $P > 0.05$).....149

Figure 8-5: GFAP IHC staining allows for the visualization of activated astrocytes. Brain slices (50 μm) were saturated with primary GFAP antibody to detect the highly expressed GFAP protein in activated astroglia. TBI (vehicle) (B) demonstrates greater activation of astroglia than sham (A), TBI (minocycline) (C), TBI (Rolipram) (D), and TBI (Rolipram and minocycline) (E).....150

Figure 8-6: IHC staining to visualize the microglial activation (A) sham (B) TBI vehicle (C) TBI (minocycline) (D) TBI (Rolipram) (E) TBI (Minocycline and rolipram)..151

LIST OF TABLES

Table 3-1: <i>The N-terminus of Each Peptide is Conjugated to a Fluorophore in the L Form of Amino Acids. As Spacers, Two Beta Alanine's are Coupled Between the Therapeutic Drug and Fluorophores.</i>	24
Table 4-1: <i>Primers used for the RT-PCR Test in Hepatocytes.</i>	56
Table 6-1: <i>Summary of Tests, Procedure, and Treatments for Each Mouse for the Biodistribution Study</i>	93

ACKNOWLEDGMENTS

I want to take this opportunity to show my appreciation to everyone in my life who has developed me into the person I am today. I attribute my success in life to the love, care, and encouragement I received from my parents and grandparents. My heartfelt thanks to my husband, who has supported me through the years and for believing in me. To my wonderful sister Teja, who has always been there for me and given me honest feedback, helping me take proper steps. I will be forever grateful to Mr. Prasad and Mrs. Padmakka for guiding me in the right direction and helping us when we needed it the most. This work would not have been possible without my principal investigator, mentor, and, indeed, a wonderful person, Dr. Teresa Murray. I will be eternally grateful to her for allowing me to work in her lab, providing guidance in my professional development, and nourishing my skills.

In addition, I'd like to take this opportunity to express my heartfelt gratitude to Dr. Nestorova for always being available to me when I needed it. I would also like to thank Dr. Lvov, Dr. Kim, Dr. Arumugam, Dr. Poh, and Dr. Decoster for their technical contributions to the projects on which we have collaborated. I am grateful to Dr. Ramu Ramachandran and Dr. Collin Wick for their guidance and to Louisiana Tech University for providing financial support.

A special thanks to Vivya Kalidindi for her assistance with behavioral analysis and Kevin Holly for teaching me how to use MATLAB for behavioral analysis. To Afrika

Williams, for helping me with statistics; Ritika Roy, for assisting me when necessary; Jolin Rodriguez, for her friendship, consistent help from the moment I joined tech, and putting up with my silly self; and Sanjeev, for collaboration and staying back in the lab with me when I was working late hours. For their contributions to this work, I am grateful to everyone in my lab and colleagues from the collaboration lab. I am grateful to Havisha Nadendla, Sai Rudrashetty, Natasha Singh, and Lahari Kakani for all the support they've given me and for being such wonderful friends.

Finally, I'd like to thank all the previous researchers who laid the groundwork for this study and Louisiana Tech University for giving me the tools I needed to thrive in a variety of fields. Spending time at Louisiana Tech has been tremendously rewarding for me; I've developed many relations, expanded my scientific knowledge and skillset, and grown professionally.

CHAPTER 1

INTRODUCTION

1.1 Research Need

The pharmaceutical industry has seen tremendous advancements, with new technologies and advanced medicines entering the market every year[1]. Despite these advancements, many candidates fail to translate to the clinic as these molecules could not rapidly traverse into the target cells, limiting their effectiveness. Notably, neurodegenerative central nervous system (CNS) disorders like Alzheimer's disease and amyotrophic lateral sclerosis (ALS) are on the rise, and they lack effective treatments. The BBB is essential for maintaining homeostasis it stands as an arduous soldier preventing the therapeutic molecules from entering the brain and limiting the development of successful neuro pharmaceuticals.

In addition to neurodegenerative disorders, trauma to the brain due to injury or intracranial hemorrhages leads to a second phase of injury (secondary injury) causing neurodegeneration of healthy surrounding cells which compounds the initial injury, resulting in poor outcomes post-injury[2]. Secondary injury is triggered by an inflammatory response from cells surrounding damaged cells, further aggravating the condition. Despite our understanding of pathophysiological functions, most CNS conditions lack effective, safe, and non-invasive pharmacological treatments[3]. There is an urgent need for the development of new drugs and effective carriers for existing drugs

that could help these therapeutic molecules to rapidly cross the cell membrane and BBB in therapeutically functional concentrations without damaging cell membranes. Peptides and nanoparticle drug carriers provide a potential means for drugs to access cellular and molecular targets inside the brain that would otherwise be blocked by the BBB.

1.2 Current State of Research

Over the past decade, CNS diseases and traumatic brain injury (TBI) research has proliferated extensively due to innovations in rehabilitation, advancements in imaging techniques, and advanced models for cognitive and translational research [4]. Subsequently, enormous clinical failures tempered the advancements and enthusiasm of pharmaceutical companies to develop non-invasive medicines with potent therapeutic effects and minimal adverse effects. Post-TBI effects continue to plague millions of individuals around the world, and the number of TBI survivors with psychological disabilities due to secondary injury continues to rise. There is a paucity of effective treatments for recovery. To improve the outcome, both physically and psychologically calls for major research focus on neuronal restoration and to prevent neuronal degeneration post-injury[5]–[7].

In addition to small molecule drugs, peptides that originally entered the market as supplemental therapeutic molecules have evolved dramatically. Today more than 60 different synthetic therapeutic peptides are available and their numbers and types continue to trend upward with their enormous potential to treat various disease conditions [8], [9]. These peptides are biologically active molecules and closely mimic molecules that activate physiological pathways. Further, peptide sequences can be easily modified to optimize their pharmacokinetic properties [10]. In contrast, native peptides are

typically unstable and rapidly degraded by digestive and blood enzymes, resulting in poor bioavailability and a short half-life. However, engineered peptide drugs typically lack target cell selectivity. This could be circumvented by conjugating peptide medicines to vectors such as nanoparticles, antibodies, or other peptide moieties with particular receptor affinity [8], [11].

Peptide drugs that exhibit efficient therapeutic properties are not readily permeable to the cell membrane and the BBB. Given that peptides are easily modified and degraded, it is challenging to deliver peptide drugs into the cell in the right functional concentrations and with no adverse effects. Modification of peptide sequences by conjugating them to cell-penetrating peptide (CPP) sequences enhances the cellular permeability of the cargo. CPPs are cationic short amino acid sequences that rapidly transport cargos intracellularly into a vast variety of cells [12]. They can be formed endogenously and exert biological activities. Several studies revealed the ability of CPP to transport different cargos across the BBB efficiently. CPPs traverse into the cells by endocytosis or by an energy independent mechanism like direct diffusion. These peptides are coiled in solution, and upon interaction with the membrane interface, they transform their shape to be cross the membrane. pVEC and TP10 are cationic CPPs that adopt β -sheet and α -helical structures, respectively, at the BBB endothelial membrane interface and traverse through a non-saturable mechanism. SynB3 and Tat 47-57 remain coiled and are transported by adsorptive-mediated transcytosis. Adsorptive-mediated transcytosis is a non-specific mechanism that is initiated by an electrostatic interaction between the negatively charged cell membrane and positively charged peptides. Most of the CPP's are cationic and arginine rich, resulting in high charge density that favors the influx of

peptides into the brain [13]. In vivo studies of these cationic peptides showed that about 80% of them reached the brain parenchyma while 15-20% of the peptides were trapped in the endothelial cells[13].

The other common method for increasing permeability is to use peptide drugs that transport cargos by receptor-mediated endocytosis that are specific to cells with the target receptors. This Trojan horse technique allows impermeable compounds to cross the BBB. While this approach appears promising and has been demonstrated to effectively transport peptide cargos, a significant amount of the peptide is degraded by lysosomes, resulting in low therapeutic drug concentrations[14], [15]. This proposed study will compare two distinct peptide conjugates with two different BBB-crossing transport pathways.

1.3 Research Hypothesis and Specific Aims

Peptides have great potential in the pharmaceutical industry, and they have proved their mettle as carriers for different pharmaceutical molecules. It is important to explore their ability to cross the BBB and their cargo-carrying capability across these membranes. It is also essential to understand their biodistribution and functionality in the brain so ideal BBB delivery candidates can be added to the pharmaceutical library. The primary objective of this study is to find a suitable functional carrier for therapeutic molecules with BBB-penetrating capability that would be useful to treat TBI and to understand the utility of these peptide carriers.

The following aims has been investigated to test the hypothesis that KAFAK, a CPP conjugate improves the cellular uptake and therapeutic efficiencies of drugs.

- (1) Evaluate the intracellular uptake, efficacy, and cytotoxicity of KAFAK a CPP vector, conjugated to a therapeutic peptide in an in vitro brain model.
- (2) Demonstrate and compare the ability of KAFAK and receptor mediated peptide vector (L57) conjugated with a therapeutic peptide to traverse the BBB in an in vitro BBB model and assess its efficacy and potential cytotoxicity.
- (3) Demonstrate the ability of the KAFAK CPP vector conjugated to a therapeutic peptide to cross the BBB and reduce secondary injury after TBI using a mouse model of moderate TBI.
- (4) Demonstrate the ability of minocycline and rolipram conjugated to cationic nanoparticles to reduce the inflammatory response and induce neuroprotection by 14 days after injury in a mouse model of moderately TBI.
- (5) Determine if HNTs can cross the BBB, and can effectively deliver a drug. Make a preliminary assessment of potential effects of HNTs on brain function.

In Chapter 2 of the dissertation, background information on BBB, TBI, and CPP is presented, while subsequent chapters describe the synthesis and characterization of peptides, creation of HNTs, and the results of the objectives mentioned above.

CHAPTER 2

BACKGROUND

2.1 Traumatic Brain Injury

Traumatic brain injury (TBI) is one of the main causes of mortality and morbidity in the United States and around the world, affecting people of all ages [16]–[18]. More than 50 million people are impacted by TBI annually [16], [19]. After the year 2020, TBI will be the third leading cause of mortality and permanent impairments [20]. Automobile collisions, falls, assaults, wars, traffic-related accidents, and contact sports are among the leading causes of TBI [17]. Many TBI survivors have permanent disability, significant brain damage, and many even with mild and moderate injuries have permanent problems [21]. The resulting damage is complex, with a wide spectrum of symptoms, and current diagnostic tools make identifying the source and extent of the problem extremely challenging, making this a silent epidemic [17]. TBI not only affects the victims but also their families and has a profound impact economically (approximately \$56 billion every year in the US alone) and socially. In spite of extensive research and development of diagnostics and medicine over decades TBI lacks effective treatment measures [17].

TBI is the temporary or permanent disruption of normal brain function induced by any external mechanical force [17], [22]. TBI has emerged as a major concern, especially in developing countries with inadequate diagnostic and treatment options and with

increased automobile accidents [23]. According to the Glasgow coma scale (clinical observations and self-report technique), TBIs are classified as mild, moderate, or severe [21]. Mild injuries are more prevalent and challenging to identify compared to moderate and severe injuries [24]. TBI survivors may experience significant physical, cognitive, and learning impairments, as well as long-lasting health repercussions. Depending on the degree of the damage, some of these disorders may be temporary and some may be chronic. Recent research indicates that TBI is associated with the development of several neurological disorders, including dementia, epilepsy, and Alzheimer's, and Parkinson's diseases [17].

2.1.1 Primary and Secondary Brain Injury

TBI is caused by a primary injury and can be exacerbated and prolonged by secondary injury mechanisms [19], [25]. The initial traumatic insult sustained at the point of contact with an external mechanical force is known as the primary injury [26]. The primary injury may or may not be a penetrating injury, although the cellular integrity of the brain is compromised in both instances. In penetrating traumas, the skull is fractured, causing damage to the brain's interior; this is known as an open head injury. These injuries are difficult to cure with drugs alone and frequently require surgical interventions. In closed head injuries, the skull remains intact, but fast acceleration and deceleration induced by sudden, uncontrolled head motions cause brain injury [20], [26], [27]. Primary injuries are permanent and induce direct mechanical damage to cells, such as axons, glia, neurons, and blood vessels, through tearing, shearing, or stretching. This may result in bleeding (hemorrhages), lacerations, contusions, or diffuse-axonal damage [19].

Secondary damage is the result of a cascade of cellular, metabolic, and neurochemical changes that occur after the initial injury. The appearance of secondary damage is contingent on a number of variables, including the degree and nature of the initial injury, as well as the injured person [28]. Primary injury causes many disruptions in the normal functioning of the brain including increased intracranial pressure due to edema, hypoxia due to vascular injury, and inflammation due to cell damage. Due to the massive ion fluxes caused by the initial traumatic shock, the afflicted cells may release unusually high quantities of neurotransmitters and undergo prolonged depolarization across neuronal membranes. In addition, mitochondrial dysfunction, excitotoxic cascades, inflammatory responses, and oxidative stress may stimulate the production of pro-inflammatory cytokines, toxins, free radicals including reactive oxygen species, nitric oxide, prostaglandins, and inflammatory cytokines that contribute to the development of self-perpetuating secondary injury. These biochemical reactions can be activated within minutes, days, or even months after the original impact and may result in delayed neurological impairments and neurological disorders in people with TBI [17], [19], [26].

2.1.2 Diffuse Axonal Injury in TBI

Diffuse axonal damage (DAI) is a structural condition and a prevalent pathology of TBI, affecting 40-50% of patients [20], [29]–[31]. Every TBI is accompanied by a component of DAI, which later manifests as functional and/or psychological deficits [32]. It is a multi-focal injury characterized frequently by prolonged coma due to axonal damage in the brain parenchyma induced by inertial shear strain [30], [33], [34]. Contrary to the phrase diffuse, the injury is not widespread but rather prevalent in distinct parts of the brain, particularly in regions with varying tissue densities, such as gray and white

matter junctions [30], [33], [35]. The parasagittal white matter of cortex, cerebrum, corpus collosum, brain stem, and cerebellum are the most common damage sites linked with axonal degeneration caused by DAI [35]. Despite the prevalence of DAI and the impairments it causes in motor, cognitive, autonomic, and sensory functioning, the disease cannot be diagnosed with current imaging techniques before the development of lesions [31].

The axons in white matter are not built to resist mechanical shear [31]. When the brain is exposed to extended inertial shear as a result of rotational, translational, fast acceleration and deceleration, compressive and tensile stresses cause axon damage and blood vessel straining [20]. Axons are generally flexible and display viscoelastic properties; however, they become brittle under rapid, traumatically stressful situations, and their structural proteins distort, resulting in the undulation of damaged axons from the structural changes in the axon cytoskeleton. The change in the cytoskeleton causes swelling (sodium influx) and the formation of bulbs and varicosities due to the accumulation of transport vesicles resulting from impaired axoplasmic transport due to cytoskeletal damage. The depletion of ATP, hypoxia, and sodium produces an influx of calcium into these axons, which could accelerate the damage and result in severed axons that contribute to several neurological disorders [35], [36]. Damage to axons is proportional to the rate and magnitude of the strain, and axonal disconnections occur over time. With the correct intervention, some of these axons may heal, thereby avoiding disconnection. DAI can also develop from secondary axotomies, such as calcium homeostasis disruption, increased glutamate neurotransmitter release, and inflammatory cytokines [20].

2.1.3 Role of Inflammation in TBI

Inflammation became a research focus and a potentially effective therapeutic target since it is a crucial and important factor in the development of secondary damage [28]. In healthy individuals, inflammation serves as a critical defense mechanism against infections for healthy cells [28], [37]. Although in some pathological conditions, the immune system's activation results in excessive inflammatory signals that could exacerbate and accelerate the damage to healthy tissue [28]. One such pathogenic condition where inflammation plays a significant role in the neuronal pathophysiology is TBI, which can result in excessive cytokine production and subsequent secondary tissue damage [28], [38], [39]. Recent studies have revealed that neuronal inflammation following a TBI is linked to a poor prognosis, and accumulating evidence suggests that it plays a role in subsequent development of neurological diseases.

The BBB separates the brain from the bloodstream and regulates the flow of immune cells and other chemicals, distinguishing the central nervous system (CNS) from the rest of the body [37], [39]. However, the activation and sequestering of the immune response are comparable to those of other organs. Damaged neurons emit damage-associated molecular patterns (DAMPs) and matrix metalloproteinases (MMPs), which activate microglia, following the initial brain injury [7], [40]–[42]. Microglia are the brain's innate immune cells and its first responders. Activated microglia release cytokines, chemokines, and small signaling molecules that activate endothelial cells, astrocytes, and the peripheral immune system to recruit immune cells such as monocytes, neutrophils, and leukocytes to the site of inflammation [7], [37], [39], [42]. These inflammatory cells can signal the secretion of more inflammatory chemicals, adhesion

molecules, and growth factors, as well as induce cellular infiltration, which facilitates cellular regeneration or cell death [39].

Most cytokines have overlapping functions and are tiny proteins with a very short half-life [37]. Human TBI patients exhibit significant levels of tumor necrosis factor (TNF), interleukin 6 (IL-6), interleukin 10 (IL-10) and interleukin 8 (IL-8), while rodents express TNF, interleukin 1 (IL-1), IL-6 and interleukin 4 (IL-4) [43]–[47]. Individual cytokine expression profiles in TBI patients can be used to evaluate the degree of tissue damage. Interleukin-1 beta (IL-1), a pro-inflammatory cytokine, is detected to a minor degree in the brains of healthy individuals. However, recent investigations have demonstrated an elevated level of IL-1 in the cerebrospinal fluid (CSF) of TBI patients [37], [48]. In addition, greater than normal IL-1 levels are associated with worse outcomes and increased intracranial pressure in TBI patients. According to a study by Nekludov et al., there is a hundred-fold rise in IL-6 expression in the CSF and blood of TBI patients [49]. TNF, formerly believed to be a pro-inflammatory cytokine, has been found to also possess anti-inflammatory characteristics, making it a multifunctional cytokine. Increased TNF expression has negative consequences on the outcome of TBI [37], [38], [45].

2.1.4 Blood Brain Barrier Disruption in TBI

BBB is a cerebrovascular endothelial microstructure with tight connections that plays a crucial function in normal brain physiological control [50], [51]. In a normally functioning brain, the endothelial cells of the BBB are bordered by astrocytes and microglia, which communicate via paracrine communication. These cells, along with pericytes and smooth muscle cells, interact physically to form the neurovascular unit

(NVU) [52]. Astrocytic processes extend to the parenchymal micro capillaries of endothelium, which contribute to the maintenance and function of the BBB and the transport of molecules in a differentiated manner [50]. The BBB barrier is structured such that the endothelial cells lining the barrier metabolize the majority of neuroactive chemicals and hazardous substances that enter the brain [50], [53]. In addition, transcellular transport within the brain is regulated by luminal and abluminal membranes, and brain endothelial cells exhibit lower endocytosis and transcytosis compared to peripheral endothelial cells [50].

The CNS system restricts the admission of immune cells and other components, such as ions, solutes, and large molecules [40]. This phenomenon is referred to as "immunologic privilege" and is dependent on the BBB. Typically, pathogenic conditions and moderate to severe TBI compromise this privilege [7], [40]. Bidirectional movement of immunological components between the brain and systemic circulation initiates a systemic response when the BBB is disrupted [7]. The rupture of the BBB is associated with a poor prognosis and is fully initiated within first few hours after injury and may persist for many years [54].

The compromise of the BBB is observed in both traumatic and non-traumatic TBI, and it is related with increased morbidity, mortality, and the development of neurological pathologies [7], [40], [55]. Immunoglobulin G, fibrinogen, and serum proteins extravasation have been observed in all patients who died immediately or within a year following TBI, indicating a loss of barrier integrity [54]. Loss of tight junctions causes biological failure of the barrier by permitting the movement of proteins and immune cells through the membrane, which initiates the inflammatory response. Second,

the endothelial cells that ordinarily inhibit transcytosis no longer do so, resulting in an increase in serum protein, albumin, and large molecule transport into the parenchyma. In addition, it produces cerebral edema, intracranial pressure, and cerebral blood flow (CBF) abnormalities. These changes, if not restrained, could cause irreversible brain damage, and increase morbidity and mortality [54], [56].

2.2 Therapeutics and Carriers to Shuttle Drugs Across BBB to Treat TBI

2.2.1 Current Strategies in TBI

TBI is a complex pathophysiological process, and any prospective treatment must not only target the physiological derangements but also numerous stages of downstream biochemical processes [57], [58]. Current therapy options are confined to symptom management and patient stabilization. Among the interventions are head elevation, hyperventilation, hyperosmolar therapy, intracranial pressure (ICP) monitoring, seizure prevention, therapeutic cooling, and, as a last resort, medically induced coma, or decompressive surgery [49]. Given to the intricacy of TBI, guidelines for medical therapy vary significantly between individuals and situations. TBI also lacks defined treatment strategies that could prevent progressive cell death following primary damage, inflammatory cascades, oxidative stress, and BBB disruption. It lacks therapeutic drugs that could promote neurovascular regeneration and neuroprotection along with targeting the afore mentioned damaging cascades [59]–[61]. In addition, despite developments in imaging technology, the noninvasive imaging modalities used today are not capable of identifying the microstructural damage that causes subsequent injury in mild and moderate TBI.

Recent advances in TBI research have led to the development of new therapeutic targets, treatment techniques, and an understanding of the mechanisms that contribute to secondary injury. Despite the advancement of in vivo research, the majority of drugs under study fail to demonstrate efficacy in clinical trials. This is due to the complexity of TBI in humans relative to in vivo models, as well as the BBB modifying the structure of molecules entering the brain, hence lowering their efficacy, or restricting their transport. In addition, several of these medications fail FDA (Food and Drug Administration) clearance, and the approval procedure is lengthy, delaying the potential drug's availability to patients. There are no FDA-approved medications for treating TBI [62]. All these criteria motivate aspiring researchers to search for CNS pathology-treating medications that are already available on the market that would halt the cascade of biological processes that cause secondary damage [63]. As such, medication repositioning and repurposing are showing promise in the development of CNS drugs.

2.2.2 Drug Repurposing

Minocycline, rolipram, N-acetyl cysteine, edaravone, glyburide, ceftriaxone, progesterone, and levetiracetam are among the repurposed pharmaceuticals being studied for the treatment of traumatic brain injury [62], [64]. To successfully target multiple injury pathways, drug combinations are frequently investigated. Anti-inflammatory medications, neuroprotective pharmaceuticals, phosphodiesterase (PDE) inhibitors, calpain inhibitors, and therapies to increase the integrity of the BBB are being studied for their synergistic effects [62], [64], [65]. Combination therapy has demonstrated efficacy in several preclinical animal studies. Figure 2-1 presents a schematic of the response of the brain to traumatic brain injury.

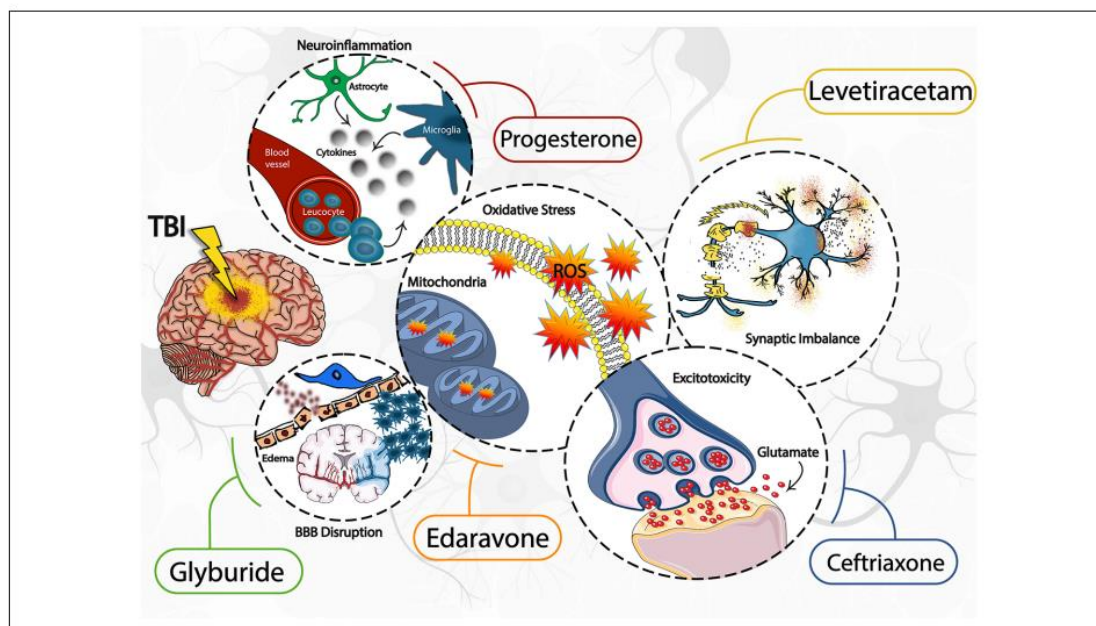


Figure 2-1: Schematic of the response of the brain to traumatic brain injury. The candidate drugs discussed in this review exert their effects through inhibiting specific injury pathways that are activated post-TBI. BBB= blood-brain-barrier; ROS=reactive oxygen species[62]

Minocycline, an extensively used second-generation tetracycline antibiotic, exhibits anti-inflammatory, anti-apoptotic, and neuroprotective properties at levels higher than required for antibiotic effects [66], [67]. Additionally, it acts as an iron chelator to reduce iron accumulation in brain injuries following intracerebral hemorrhage. Minocycline offers a broad therapeutic window for the treatment of neurodegenerative disorders, such as ischemia, Parkinson's disease, and multiple sclerosis, as well as high tolerance and the ability to pass through the BBB. It exerts its neuroprotective benefits by preventing chronic microglial activation, reducing the expression of caspase-1 and -3, inhibiting cytochrome c release from mitochondria, and suppressing metalloprotease

activity, although the exact mechanism remains unknown. It is also involved in immune cell activation signaling pathways and other secondary cascades [68], [69].

Phosphodiesterase's (PDEs) are known to degrade both cAMP (cyclic adenosine monophosphate) and cGMP (cyclic guanosine monophosphate), which are necessary for intracellular signaling in numerous cellular activities [49], [70], [71]. There are around eleven distinct PDEs in the PDE superfamily that are specifically expressed in the various brain regions [65], [72]. The highly expressed PDE4 in the human brain has an inverse relationship with cAMP [65]. cAMP is a secondary messenger molecule that is produced by adenylyl cyclase (AC). It is crucial for synaptic activity, neuronal activation and regulation, and plasticity [73]. cAMPs are degraded by PDEs, which are upregulated following TBI. Researchers are aiming to inhibit the production of PDEs to restore normal cAMP levels and improve patient outcomes. In the early stages of TBI, PDE inhibitors can reduce neuronal inflammation and neuronal mortality, whereas in later stages, they can improve circuit reorganization and reduce synaptic dysfunction [74]. Rolipram is a specific inhibitor of PDE 4. PDE4 is expressed by both immune and neuronal cells [75]. It also possesses anti-inflammatory effects by inhibiting IL-1 and TNF- α production [76] Rolipram treatment also increases the synthesis of norepinephrine, which boosts noradrenergic transmission and decreases secondary injury-associated depression [75].

2.2.3 CPP Carriers to the Brain

There are various drugs available today that might be used to treat neurological diseases. Due to their inability to penetrate the BBB, however, most of these compounds are ineffective in treating CNS diseases. Many strategies have been explored to shuttle

therapeutic drugs over the BBB into the brain. These include molecular vectors, NPs, and trojan horse molecules. Despite these efforts, the majority of these carriers have not demonstrated adequate efficiency and safety in transporting pharmaceuticals without compromising the integrity of the BBB [56]. In addition, direct drug administration to the brain may induce unwanted damage, especially in cases of diffuse TBI. Therefore, there is a paucity of effective drug carriers to treat neurological disorders such as TBI. In this study, we examined and evaluated the ability of two distinct peptides (CPP and receptor mediated peptide) and NPs (cationic nanoparticles and nanotubule HNTs) to transport drugs to the brain.

Peptides are small proteins consisting of up to 50 amino acid sequences, and multiple peptides can be transferred across the brain capillary wall via simple diffusion. Unlike proteins, synthetic peptides enable easy characterization, derivatization, and inexpensive production [56]. The saturable transport system carries the majority of endogenous peptides [77], [78]. Peptides are a source of information in the brain about peripheral occurrences, and the brain also transmits peptide signals to the peripheral system [77]–[79]. Peptides may be transferred to the brain via transcellular passive diffusion, restricted paracellular diffusion, adsorptive-mediated transcytosis (AMT), carrier-mediated transport (CMT), or receptor-mediated transcytosis (RMT) [56]. Viruses, nanocarriers, proteins, and a wide range of macromolecules are predominantly carried via AMT or RMT. Transcytosis helps prevent molecular breakdown caused by the creation of vesicles. Transport of small peptides and other simple compounds are transported via CMT or passive diffusion [56]. Figure 2-2 shows transport mechanisms of the brain.

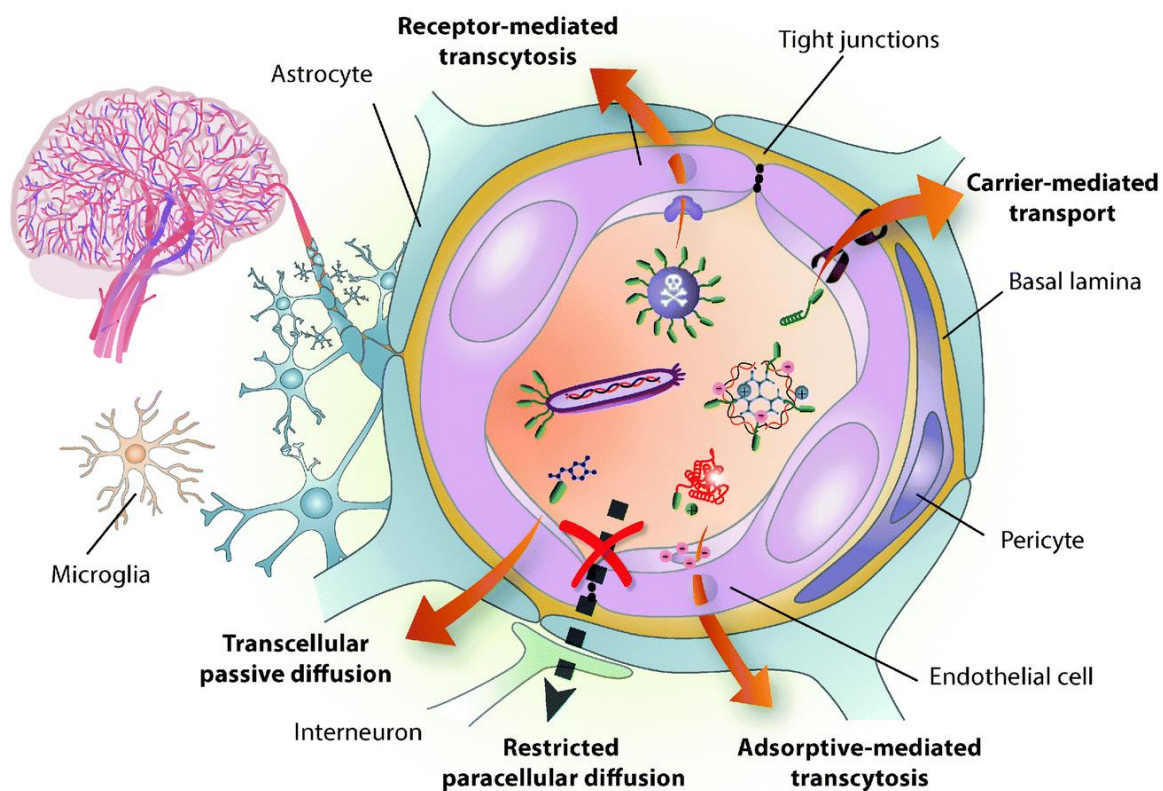


Figure 2-2: Coronal cross section of blood brain barrier showing transport mechanisms [56]

Cell-penetrating peptides (CPPs) are arginine- and lysine-rich peptides that can efficiently traverse cellular membranes without causing membrane damage [13]. The exact mechanism by which these peptides traverse the cells is not known. However, they are thought to transport into the cells by direct penetration or endocytosis. CPPs are mostly naturally derived peptides with diverse chemical structures; cationic, hydrophobic, and amphipathic. Recently, testing the potential of these peptides to cross the BBB has gained more attention. However, there are limited studies on the cargo-carrying capacity of CPP, the effect of cargo on CPP during transit and vice versa, the adverse effects of these peptides, and their transport mechanisms [13]. CPPs are ideal candidates and have the potential to serve as theranostics for the treatment of CNS

diseases that can cross the BBB. Similarly, receptor-mediated peptides use receptor-ligand binding abilities for transcytosis inside the brain. The peptides are designed to mainly target the receptors low-density lipoprotein receptor-related protein (LRP) that is highly expressed in the endothelial cells of the BBB [80]–[83]. The RMT mechanism utilized by these peptides offers excellent selectivity and facilitates the transport of peptides unmodified. However, RMT peptides require larger dosages than CPP peptides [84].

2.2.4 Nanoparticle Carriers

HNTs are biocompatible aluminum silicate kaolin (clay) tubular structures around 50 nm in length and 15 nm in diameter. Its structures allow for the modification of surface charge and drug loading within the hollow lumen. In addition, they are abundantly available, inexpensive, and simple to modify. HNTs have demonstrated great potential in the loading and slow release of a wide variety of drugs, antiseptics, proteins, DNA, and anticorrosive treatments [85]–[87]. Despite substantial research on HNTs, there are no studies examining their capacity to circumvent the BBB and to show toxicity within the brain.

Similar to HNTs, nanoparticles (NP) are nanometer-scale structures of varying sizes and shapes. Numerous investigations have demonstrated that NPs can penetrate the BBB and deliver the drug. These carbon nanotubes are less hazardous than multi-walled carbon nanotubes and can be substantially manipulated to deliver medications to the brain [88]. Additionally, the surface of these molecules is modified to covalently attach the ligands for RMT-mediated targeted drug delivery. In this study, amphiphilic NPs comprised of poly (lactide co-glycolide)-graft-polyethylenimine (Pgp) with a

hydrophobic core and hydrophilic outside are utilized [89]. Both HNTs and Pgp NPs are nanosized carriers that provide a sustained, gradual release of drug.

2.3 Animal Models in Brain Injuries

Animal models are crucial to study the cellular, molecular and biochemical aspects of the pathology, especially neuro pathologies considering they cannot be fully mimicked in vitro [2]. Regardless the efforts of the academic scientists to replicate the conditions in animal models most of the TBI drugs under study that showed promise in animal models failed in phase II or III clinical trials [2]. This could be because of poor translation of the effects of clinical TBI to the animal models. However, owing to their short life cycle, using animal models can be good start for testing drugs in in vivo conditions. Many animal models have been developed over the past decade to replicate the diverse human brain injuries where one model is not enough to address all injuries [90]. There are different models of TBI, and the most common ones are: fluid percussion injury, weight drop impact acceleration injury, blast injury and cortical injury [91]. The choice of model depends on the objective of the study and the research goal [92]. Rodents are the most popular animal models due to cost effectiveness, reproducibility, and size. For this study a murine fluid percussion injury model was used to replicate the diffuse, non-penetrating TBI.

CHAPTER 3

SYNTHESIS, CHARACTERIZATION, AND OPTIMIZATION OF THE DRUGS FOR BBB PENETRATION CLINICALLY RELEVANT ROUTES OF ADMINISTRATION

3.1 Choice of Drugs for the Study

The drugs are chosen for this study based on cell penetrating abilities (KAFAK), specificity (RMT pathway (L57)), and anti-inflammatory and neuroprotective abilities (minocycline, rolipram). L57 offers specificity towards LRP-1 and subsequent receptor mediated transport which is lacking in the other three drugs. However, most of the drugs that transport into the brain are not easily up taken by the cells inside the brain. CPP conjugates (KAFAK) have an advantage since these molecules can easily traverse the physiological barriers and deliver the drug inside the cells. Furthermore, CPP can be easily modified or conjugated to other molecules (NPs, receptor binding peptides, antibodies) to increase their specificity. As discussed in Chapter 2 and based on the research conducted by the previous lab members, minocycline [93] and rolipram were chosen for the treatment of TBI.

At higher dosages, the antibiotic minocycline has been proven to reduce the secondary injury cascade [69], [94]. Chelsea Pernici's preliminary research in Dr. Murray's laboratory indicated that minocycline treatment following moderate mFPI reduced axonal damage [95]. Acute minocycline treatment (45 minutes, 24 hours, and 48 hours) after injury reduced the development of varicosities, while delayed treatment

beginning three days after injury reduced varicosities by 79.7% by 30 days post injury. However, minocycline takes 14-30 days to exert its therapeutic effect. Consequently, rolipram, a potential synergistic drug that has shown to reduce secondary injury in spinal cord injury rat models [89], will be tried alone and in combination with minocycline. Rolipram is an antidepressant and neuroprotective drug with anti-inflammatory characteristics. Rolipram inhibits phosphodiesterase 4 (PDE4), the enzyme responsible for degrading cyclic adenosine monophosphate (cAMP). cAMP is a secondary messenger molecule that is vital for synaptic activity, plasticity, cell survival, and neuronal regulation. However, rolipram causes nausea and gastrointestinal distress. To alleviate discomfort and ensure prolonged drug release, rolipram is loaded in poly(lactide-co-glycolide)-graft-polyethenimine (PgP) nanoparticles. These nanoparticles have shown to cross the BBB (Chelsea Pernici, Claire Jones, Jeoung Soo Lee, and Teresa Murray, unpublished).

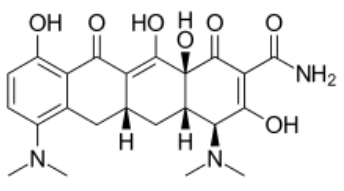
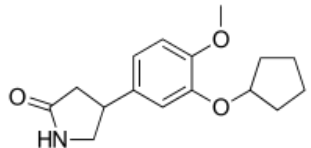
CNS disease treatment is an unmet medical concern despite the availability of different peptides and drugs due to their poor brain permeability [96]. CPP carriers have proven to be promising CNS carriers. CPP has the ability to translocate across membranes, effectively transporting molecules through physiological barriers and delivering cargoes [29]. L-penetratin, a CPP delivered intranasally, has been shown to successfully transport various peptides and proteins over the BBB and to improve their pharmacological activity [97]. Stalman et al., has shown that five CPP's (pVEC, Tat 47-57, TP10 (transportan 10), SynB3, and transportan 10-2 (TP 10-2)) delivered by the same route (IN) were able to penetrate the BBB, but their influx and efflux rates across the

membrane varied. Except for the pVEC peptide, all other peptides significantly effluxed from the brain [13].

KAFAK inhibits inflammation by targeting the MK2 pathway. After sustained intrathecal distribution of KAFAK-BDNF (brain-derived neurotrophic factor) from modified hyaluronan-methylcellulose (HAMC) hydrogels, Zhijiang et al. observed a reduction in inflammation and an improvement in the prognosis of spinal cord-injured animals [98]. Dr. Rodriguez's research in the laboratory of Dr. Murray demonstrates that L57, a peptide that traverses the brain via the RMT pathway by binding to LRP1 receptors, efficiently transported the anti-inflammatory peptide to the brain following IN delivery [80]. L57 is used for the study to compare the drug absorption with KAFAK and control anti-inflammatory peptide (AIP-1). CPP and RMT peptide are both conjugated to an anti-inflammatory peptide in order to minimize secondary inflammation in TBI. Upon conjugation to the carrier, N in the sequence (KKKALNRQLGVAA in AIP-1 was altered to A, which is critical for preserving the anti-inflammatory effects of the peptide [80].

The list of drugs used for the study are shown in Table 3-1.

Table 3-1: *The N-terminus of Each Peptide is Conjugated to a Fluorophore in the L Form of Amino Acids. As Spacers, Two Beta Alanine's are Coupled Between the Therapeutic Drug and Fluorophores.*

<i>Drug name</i>	<i>Chemical structure/sequence</i>	<i>Molecular weight</i>	<i>Use</i>
AIP-1	KKKALNRQLGVAA	1857 g/mol	Anti-inflammatory
KAFAK	KAFAKLAARLYRAKRLARQLGVAA	2911.51 g/mol	Cell penetrating abilities Carrier to cross BBB Anti-inflammatory
L57-AIP	TWPKHFDKHTFYSSILKLGKH-(Betaal(A)-LARQLGVAA-CONH ₂)	3936.75 g/mol	Receptor mediated carrier Anti-inflammatory
R8	RRRRRRRR	1488.76 g/mol	Cell-penetrating peptide
Minocycline		457.48 g/mol	Anti-inflammatory Anti-microbial Antibiotic
Rolipram		275.35 g/mol	Phosphodiesterase-4 inhibitor Neuroprotective Anti-depressant

3.2 Synthesis of Peptides by Solid Phase Peptide Synthesis

Solid phase peptide synthesis (SPPS) is one of the methods for synthesizing small peptide sequences up to 50 amino acids in length. Fmoc chemistry is the most prevalent method due to its economic feasibility, purity, and stability of amino acids [106]. For the peptide synthesis, individual amino acids protected by Fmoc on the N-terminus and side chains protected permanently during the experimental procedure are added to the solid resin. Once an amino acid is attached to the chain, its Fmoc group is removed, allowing

the succeeding amino acid to bind. After conjugating each of the sequence's amino acids, the peptide was separated from the solid substrate and purified.

The solid phase is an effective technique for multi-step procedures such as a peptide or short protein production [107]. This method involves synthesis on the surface of the solid support (polymers) and benefits from isolation at every stage. At each step, by-products and surplus reagents are drained via washings and filters, and intermediate peptides are easily eliminated using solvents. SPPS is based on the carboxyl group of the final amino acid connected to the sequences of insoluble inert resin beads [108]. The last amino acid is inserted first because peptides are synthesized from C to N, unlike biosynthesis. The resin provides support for synthesis during the entire procedure and protects the C terminus until the peptide is cleaved from the resin (Figure 3-1).



Figure 3-1: Illustration of N-terminus peptide synthesis using solid phase peptide vessel under inert atmosphere.

The selection of resin is based on the loading factor; the lower loading factor is appropriate for short peptides (<25 amino acids) since it allows for less substitution, enhancing purity. The peptides in this work were synthesized using Rink amide beads, which had a loading factor of 0.61 mmol/g, indicating the number of linkers accessible per gram of resin. The rink amide contains linkers with Fmoc protection groups that allow the insertion of amino acids following Fmoc deprotection. The protection of resin facilitates nonspecific addition and enhances specificity. In addition, the peptide amide bonds generated at the C terminus of the resin mimic the natural structure, thereby protecting the peptide from exopeptidases and enhancing its stability.

After weighing the resin, the resin is allowed to swell in DMF (dimethyl formamide), then the following steps are repeated for each amino acid addition. After completing peptide synthesis, the further steps include deprotection, washing, coupling, washing, and cleaving from the resin as shown in the Figure 3-2.

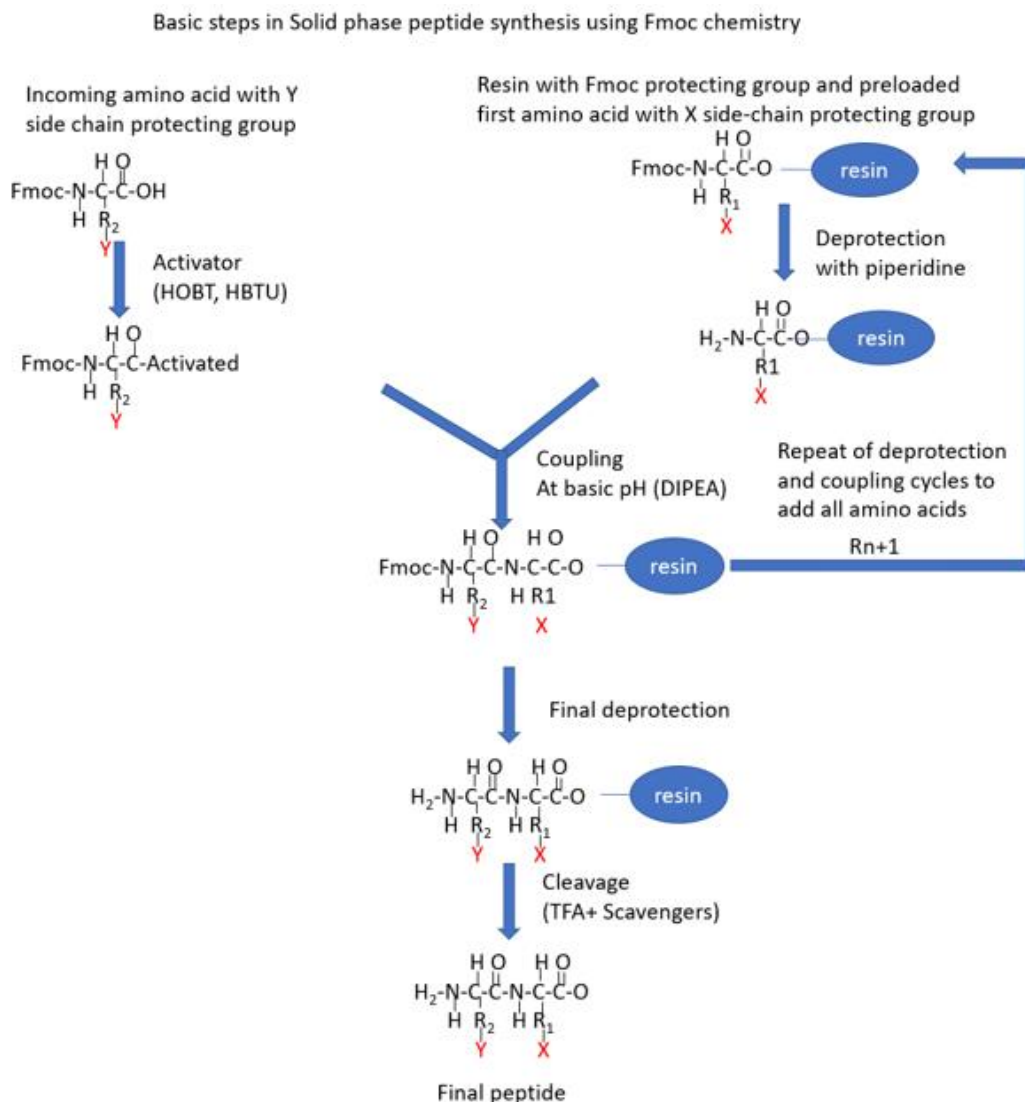


Figure 3-2: Illustrates solid phase peptide synthesis steps using Fmoc chemistry. The deprotection process contains piperidine to remove the Fmoc protective group from the resin or amino acids, allowing for the attachment of the subsequent amino acid. Followed by a coupling reaction along with activators for next amino acid addition. Once the complete chain has been produced, the peptide is separated from the resin using TFA.

3.2.1 Deprotection

The first step in peptide synthesis is deprotection, beginning with the deprotection of the Fmoc group on the resin. Fluorenyl-9-methoxycarbonyl (Fmoc) is a base-labile group that can be removed from the resin by administering strong bases. Deprotection in

peptide synthesis typically takes place in a 25% piperidine in DMF solution for 20–25 minutes. Piperidine is a strong secondary amine base capable of removing the N-Fmoc group via the E1cb mechanism (Figure 3-3 and Figure 3-4). Removing the protective group reveals the free amine group for coupling with the new amino acid or fluorophores. Carbamate salt and dibenzo fulvene are the two primary products obtained. The piperidine does not remove the side chain protecting groups since these groups are acid-labile and are only deprotected after the synthesis.

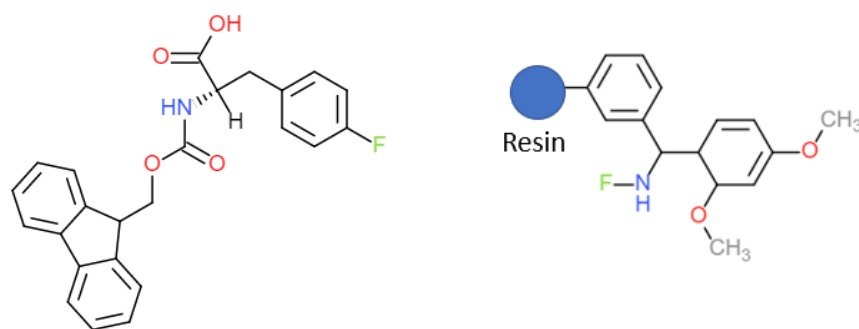


Figure 3-3: A. Fmoc group. B. Rink Amide resin protected at the NH group by Fmoc (represented as (F)).

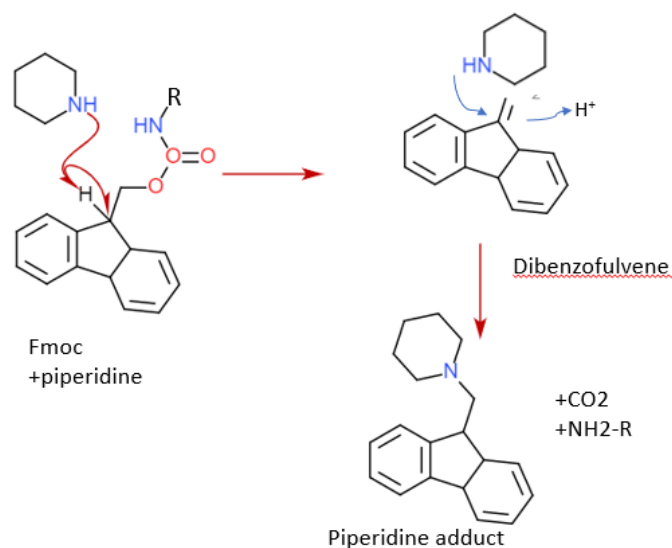


Figure 3-4: Deprotection of the N-Fmoc group of an amino acid using piperidine. After deprotection, the primary adducts and dibenzofulvene intermediates are produced.

3.2.2 Coupling Amino Acid Residues

The coupling of amino acids is an essential step in peptide synthesis since it facilitates the production of an amide bond between two amino acids under the appropriate conditions. This procedure can take three to four hours to complete in the peptide vessel. Continuous bubbling of nitrogen gas throughout this procedure helps to maintain inert conditions and mix the solution for uniform chemical distribution. Critical coupling stages include carboxyl group activation and amino group acylation.

3.2.3 Incoming Amino Acid Activation and Acylation of the Amino Group

The N-termini of amino acids added to the synthesis are protected until subsequent deprotection. Activating the amino acids' carboxyl end (C-terminus) prior to adding them to the peptide vessel for amide bond formation expedites the reaction. It protects the amino acids' structure [109], [110]. Additionally, extra reagents aid in accelerating the coupling process. For the activation of amino acids, the activator N-[(1H-benzotriazole-1-yl) (dimethylamino)methylene]-N-methylmethanaminium hexafluorophosphate N-oxide (HBTU) is employed at a ratio of 1:1. (2.5 equivalence of amino acid used). HBTU, an aminium/uronium-based reagent at the C terminus, transforms amino acids into OBt (Oxy benzotriazole in HOBT) esters, readily forming the link. After activation with HBTU, byproducts that are soluble in dimethylformamide (DMF) are produced, and HBTU also minimizes the formation of side chains. However, if the conditions are not inert, it may produce unwanted tetramethylguanidinium byproducts, that reduce the peptide yield [107].

In addition, two equivalents of 1-hydroxy benzotriazole HOBt were added to the mixture to avoid racemization and epimerization [107]. It also aids in stabilizing the

amine and enhancing the ester produced by HBTU's reactivity. These components (HBTU, HOBt, and the amino acid to be added) are weighed and dissolved in DMF to create a cocktail coupling mixture. The components were dissolved in 1.5 equivalents of DIPEA (diisopropylethylamine), which was added to the vial. The solution was transferred to the coupling vessel after 15 minutes, followed by adding 1.5 equivalents of DIPEA (DIPEA 1:3 ratio of the amino acid). Strong base DIPEA, a tertiary amine, aids HBTU in forming carboxylate. The use of DIPEA and DMF prevents the production of unwanted byproducts. Upon addition of the cocktail, the activated carboxylate forms a peptide bond with the accessible amino group.

3.2.4 Washing and Filtration

After each stage, including deprotection and coupling, unwanted soluble byproducts (ure(A) and unreacted reagents are removed by washing. The washing steps consist of three three-minute washes with DMF, two three-minute washes with isopropyl alcohol (IP(A), and three three-minute washes with DMF. After each stage, unreacted reagents are drained from the vessel, and the resin is washed with isopropyl alcohol (IP(A) to remove any chemical residue. Finally, DMF is used to clean the IPA and any other soluble byproducts.

3.2.5 Labeling with Fluorescent Dye

The peptides were labeled with FITC for in vitro research and RITC for in vivo experiments. After coupling the final amino acid (including two -alanine linkers) and washing the resin, the peptide is deprotected to remove the protective group from the -alanine at the N terminus in preparation for the addition of the fluorophore. Fluorescein (1.5 equivalence), N-Hydroxysuccinimide (1.3 equivalence), Dicyclohexylcarbodiimide

(1.3 equivalence), and N-[(dimethylamino)-1H-1,2,3-triazolo[4,5-b] pyridin-1-ylmethylene] -N-methylmethanaminium hexafluorophosphate N-oxide (HATU) (1.5 equivalence) and DIPEA (5.0 equivalence) were dissolved in DMF in a vial and allowed to sit in the dark for three hours. This amine-reactive fluorescein succinimide ester was added to the reaction vessel along with three equivalents of DIPEA and left to react for three hours.

3.2.6 Cleavage of the Peptide from the Resin and Isolation

Trifluoroacetic acid (TFA), a strong acid, was used to extract the peptide from the resin, which also removes the acid-labile side chain protecting groups. This procedure is conducted only once the peptide synthesis, and fluorophore addition has been completed. TFA addition results in the cationic species alkylating the exposed side chain functional groups. Water, TIPS (triisopropylsilane), and EDT (ethanedithiol) at 1% were introduced as scavengers to inhibit the attachment of the free species back to the peptide chain. Depending on the arginine and lysine groups in the peptide chain, 3 to 4 hours were required to cleave the peptide. More arginine or lysine groups in a peptide increase the time necessary to remove the peptide from the resin. After cleaving the peptide, the residue soaked in TFA is collected and evaporated using rotavapor to a volume of 1-2 ml. Diethyl ether was added drop by drop to the peptide-TFA cocktail at a ratio of 1:10, resulting in the formation of a white precipitate. The precipitate was centrifuged to remove the supernatant, and then the crude peptide was dried and dissolved in water in preparation for lyophilization. The lyophilized peptide was stored at -20°C.

3.2.7 Removal of TFA Acetate Counter Ion

The cationic peptide obtained after Fmoc synthesis is TFA salt, which can affect the viability of the cells [111]–[113]. In addition, studies conducted by Ma et al. demonstrated that TFA stimulates glioma cell proliferation and protein synthesis. In a separate study, Cornish et al. showed that TFA has detrimental effects on all cell types at a concentration of 10^{-9} M [112]. Therefore, selecting a residue that minimally interferes with the experiment is optimal. Most researchers opt for substituting the TF acetate salt with the acetate anions. However, the number of acetate anions should also be minimized for pharmaceutical purposes, as this impurity has no pharmacological benefit [111]. We have used HPLC to determine the purity of the peptides synthesized in the lab, and HPLC-purified peptides are TFA salts.

As proposed by Roux et al., the peptides are treated with a counter-ion exchange cycle. This includes repeatedly freeze-drying the sample while replacing the ions with a stronger acid [113]. At 4°C , 15mg/ml of peptide TFA salt was dissolved in DI water at a concentration of 1mg/ml, and 1M NaOH was added slowly to precipitate the solution. The solution was allowed to settle for 30 minutes. The supernatant was then extracted using centrifugation at 4°C , 2500 rcf for 5 minutes while the pellet was maintained. This procedure was repeated approximately six times until a neutral, salt-free peptide was achieved. The COO^- counter ions finally neutralize the peptide by replacing the positive charges of the side chains [113]–[115]. To reduce the amount of excess acid, the neutral peptide was dissolved in a 2:1 acetate solution. Due to a lack of resources for this preliminary research, peptides were utilized as TF acetate salts, which exhibit cytotoxicity, particularly with the KAFK peptide. Depending on the intended usage, the

peptide was lyophilized, weighed, and aliquoted in Eppendorf tubes (2-5mg/tube) before being stored at -80°C or -20°C. Peptides dissolved in appropriate buffers (stock solutions) are stored at 4° C to prevent freeze-thaw cycles.

3.3 Characterization of Peptide

After the addition of every few amino acids (about 7 amino acids), a few resin beads are collected into an Eppendorf tube containing TFA for matrix-assisted laser desorption ionization-time of flight mass spectrometry (MALDI-TOF MS) analysis. This is repeated with each peptide. MALDI-TOF MS aids in determining the mass of the compound, which can then be compared to the theoretical mass of the synthesized sequence. The acquired data also provides a glimpse of the side chains and contaminants created during the procedure. The amount of sample required for analysis is really small, which serves as a great advantage. For analysis, the Bruker UltrafleXtreme MALDI TOF/TOF MS from Louisiana State University in Baton Rouge was used. In addition, HPLC analysis was performed to determine the impurities in the samples. Due to the absence of separation columns, HPLC was not used for purification for the peptides synthesized in the lab. The HPLC data is presented in Figure 3-5, Figure 3-6, Figure 3-7, Figure 3-8, Figure 3-9, Figure 3-10, and Figure 3-11.

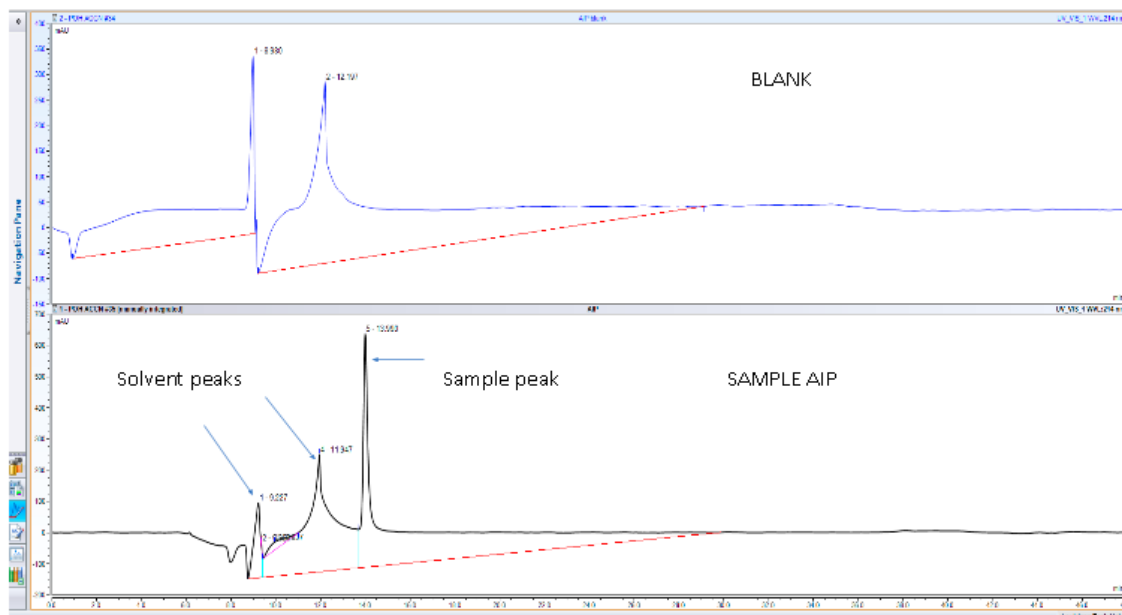


Figure 3-5: AIP-1 peptide HPLC data demonstrating the purity of the peptide synthesized after lyophilization. A gradient of water and acetonitrile was employed to elute the peptide. The sample peak was isolated and sent for MALDI-TOF MS, which showed a pure sample. KAFK, R8, and AIP were synthesized in the lab and purchased from AAPTEC (AIP-FITC) and Biomatik, as described in earlier chapters (KAFK-FITC, KAFK-RITC).

Mass Spectrometry Report

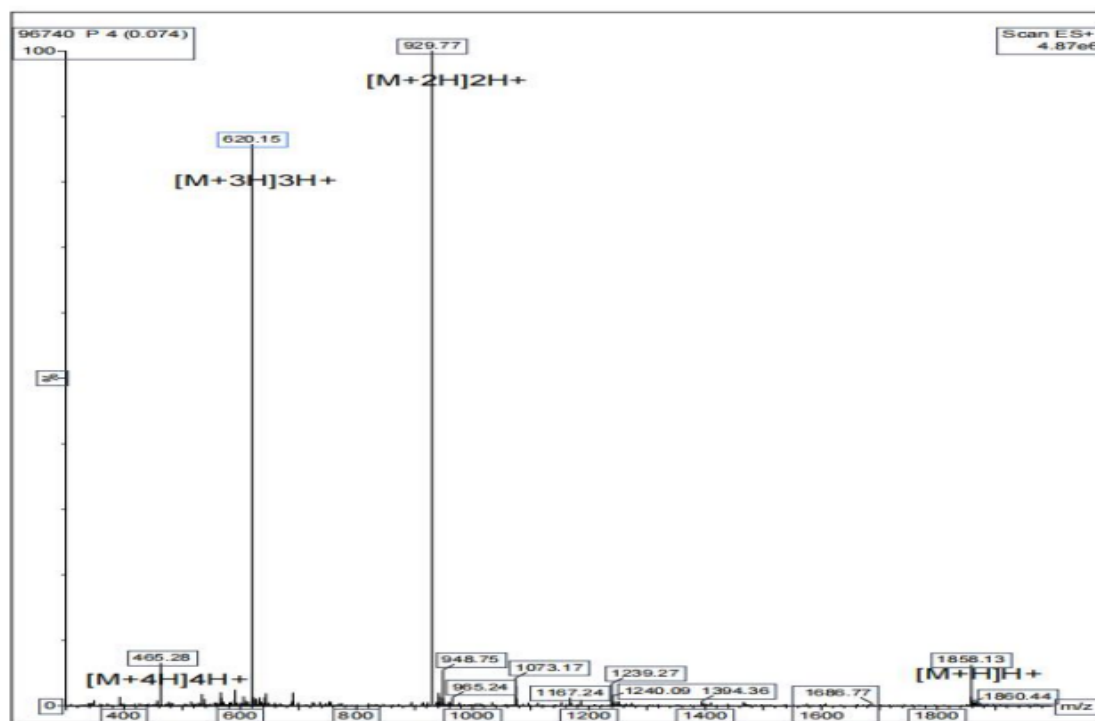


Figure 3-6: MALDI-TOF MS spectrum of anti-inflammatory peptide (AIP-1) unprotected peptide sequence FITC-Ahx-NH-KKKALNRQLGVAA-COOH. Expected mass: 1857.13, analyzed mass: 1858.13 (aaptec)

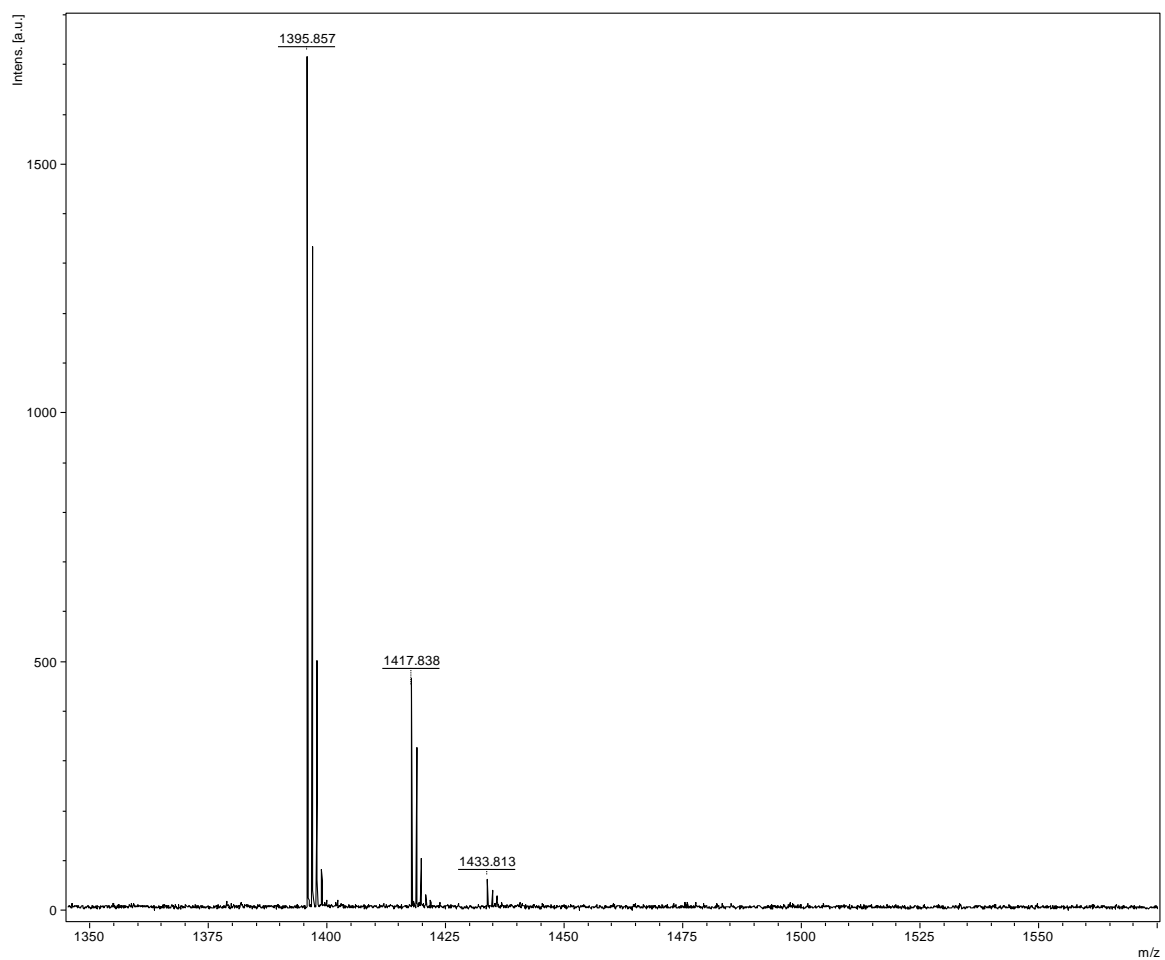


Figure 3-7: MALDI-TOF MS spectrum of anti-inflammatory peptide (AIP-1) peptide sequence KKKALNRQLGVAA-COOH. Expected mass: 1418, analyzed mass: 1417.83 (LSU, Baton Rouge)

MS REPORT

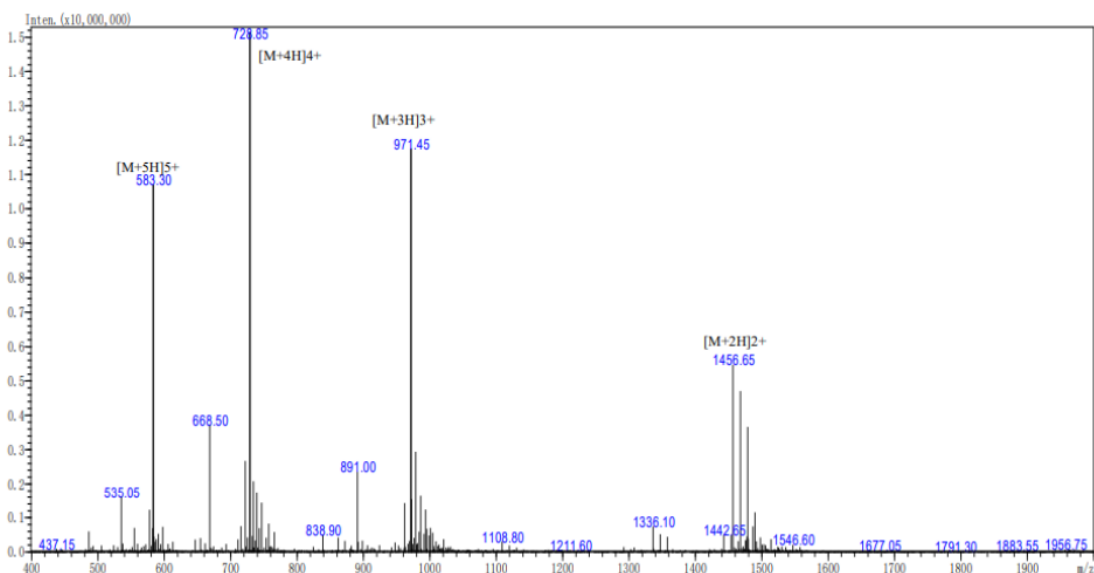


Figure 3-8: MALDI-TOF MS spectrum of CPP+anti-inflammatory peptide (RITC-KAFAK) peptide sequence rhodamine RITC-KAFAKLAARLYRKALARQLGVAA. Expected mass: 2911.59 (Biomatik).

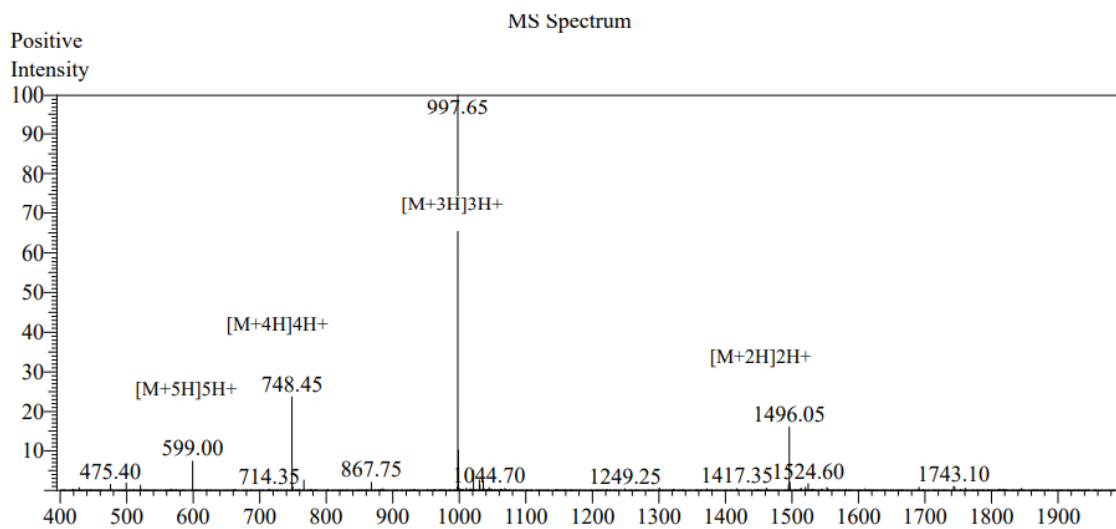


Figure 3-9: MALDI-TOF MS spectrum of CPP+anti-inflammatory peptide (FITC-KAFAK) peptide sequence FITC-Ahx-KAFAKLAARLYRKALARQLGVAA. Expected mass: 2989.95 (Biomatik)

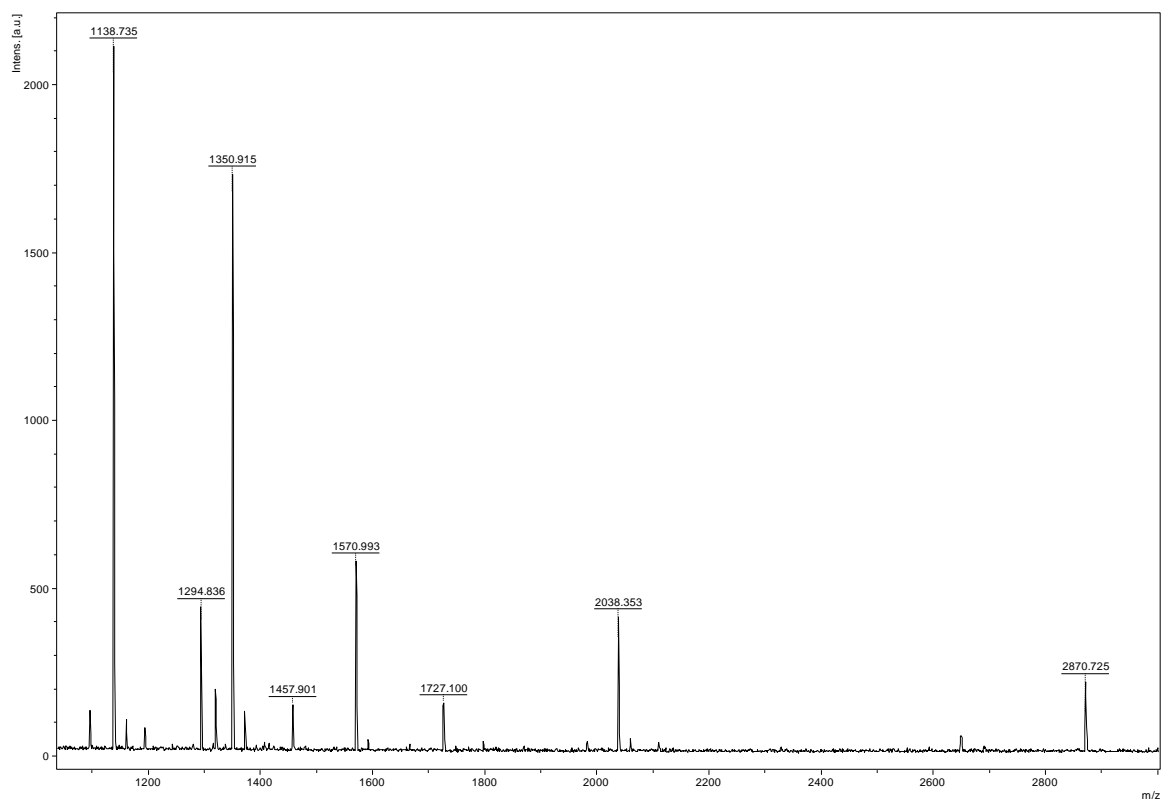


Figure 3-10: MALDI-TOF MS spectrum of CPP+anti-inflammatory peptide (FITC-KAFAK) peptide sequence FITC-Ahx-KAFAKLAARLYRKALARQLGVAA. Expected mass: 2989.95 (LSU, Baton Rouge).

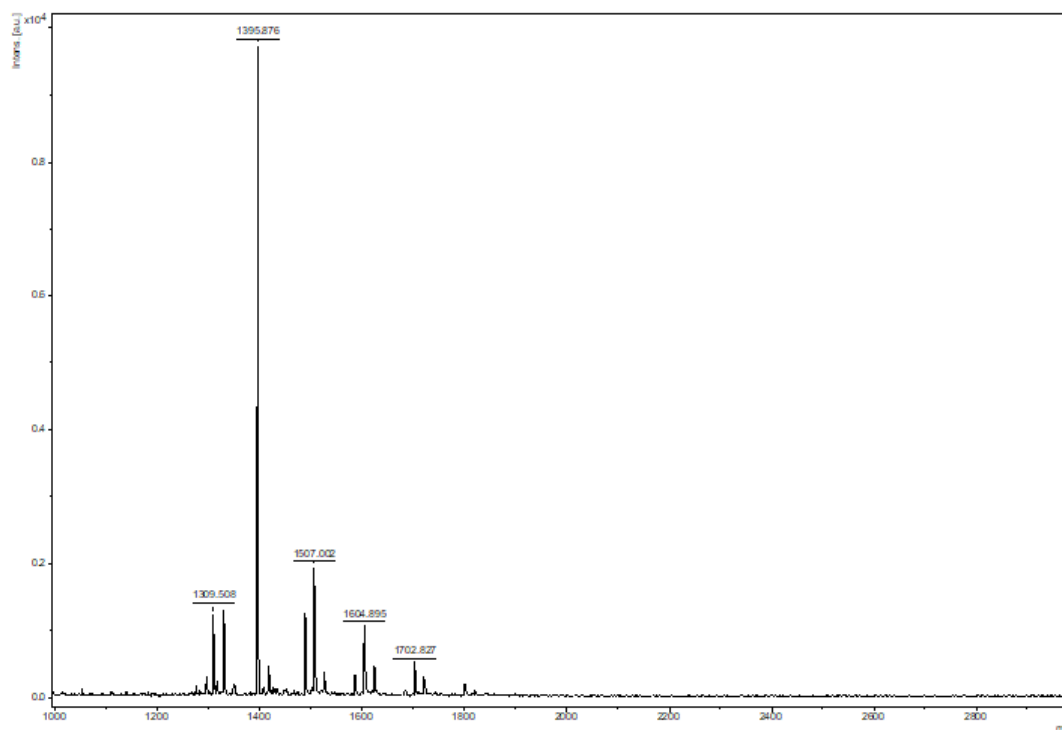


Figure 3-11: MALDI-TOF MS spectrum of R8 peptide sequence RRRRRRRR Expected mass: 1488.76 (LSU, Baton Rouge)

All peptides were successfully synthesized in the lab for preliminary investigations and studies on HEP, RAW, J774, and SHEP-1 cell lines. For in vitro experiments on primary endothelium cells and microglial cells, Biomatik and Aaptec peptides were purchased. The peaks in the MS spectrum outside of the intended mass represent contaminants, which are removed using HPLC columns.

3.4 Synthesis of Nanoparticles and Rolipram Loading for 14-Day Trial

For the 14-day time point study, P_gP NPs synthesized and loaded with rolipram in Dr. Lee's lab (Clemson university) were used to treat mice after a moderate, diffuse TBI. P_gP NPs are cationic, amphiphilic copolymers with a hydrophilic shell and a hydrophobic core. The hydrophilic shell assists in the binding of therapeutic particles through electrostatic interactions, whereas the hydrophobic core assists in the binding of

hydrophobic molecules within the core. In addition, ligands, antibodies, or fluorophores can be used to identify the surface of these particles. Studies conducted by Lee et al. demonstrated that these nanoparticles were efficiently loaded with rolipram, restored cAMP levels after spinal cord injury (SCI), and decreased inflammation in a rat model of spinal cord damage [89].

PgP NPs are synthesized by activating the carboxyl ends of 60 μ moles of poly (lactide-coglycolide) (PLG(A) with 72 μ moles of N, N'-dicyclohexylcarbodiimide (DCC), and N-hydroxysuccinamide (NHS). This solution is refined to remove contaminants and byproducts such as dicyclohexylurea. The filtered solution is added dropwise to 50 μ moles of bPEI (branched polyethylenimine) and stirred continuously at room temperature for 24 hours. The obtained PgP is purified by membrane dialysis (MWCO: 50,000) against DI water and changing water when necessary. The solution of PgP NP is centrifuged for 10 minutes at 5000 rpm before being lyophilized.

The lyophilized PgP nanoparticles were dissolved in water (1mg/ml), and 100 μ l of various concentrations of rolipram dissolved in ethanol was added to each ml of PgP nanoparticles and incubated for 4 hours. Overnight, the ethanol solvent was evaporated (solvent evaporation method), and the sample is filtered through a syringe filter to eliminate free rolipram. HPLC is used to assess the amount of loaded rolipram in the PgP NPs, whereas DLS (dynamic light scattering) was used to determine the particle size [89].

3.5 Synthesis of Halloysite Nanotubes and Loading Them with Diazepam and Ritc Dye

Halloysites were bought from Applied Minerals and were loaded with RITC dye in Dr. Lvov's lab by Mahdi Saleh. Halloysite samples were loaded with 0.5, 1, and 2 mg of RITC and ionomycin at various concentrations, including 10 mg halloysite/1mL in DI water, using continuous stirring, centrifugation, and sonication. After adding RITC, the sample solutions were sonicated and vortexed for at least one minute, followed by 24 hours of mixing on a stir plate at room temperature. The mixture is centrifuged for 2.5 minutes at 4500RPM to remove unbound RITC from the solution. The samples were dried for 24 hours at 70°C in an oven or vacuum pump. The materials were evaluated, weighed, and utilized in the study. Figure 3-12 shows the release profile of rhodamine isothiocyanate.

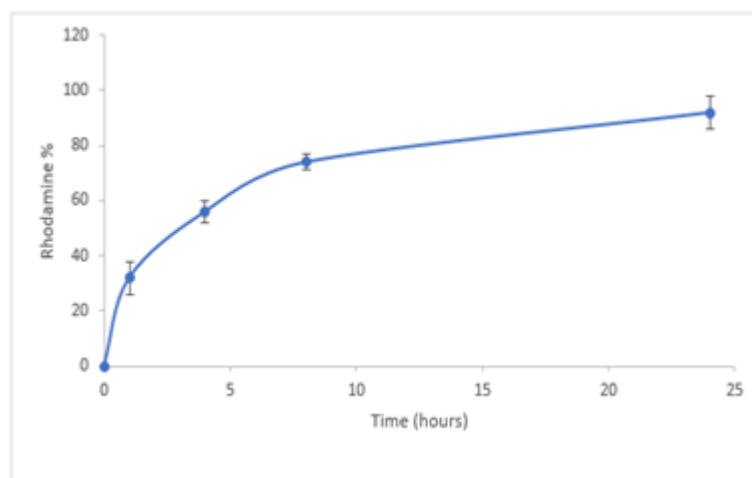


Figure 3-12: Rhodamine Isothiocyanate release profile using 10 mL of endothelial cell culture media, 3.3 mg of HNT-rhodamine was taken and stirred at 250 rpm for 24 hrs. Readings were taken after 1, 4, 8, and 24 hrs. Displays the rate at which the dye is released over a period of 24 hs.

The results show that there is an initial burst of rhodamine release of roughly 25 % within the 1 h time frame which is an expected characteristic when utilizing halloysite nanocontainers (Figure 3-13). Figure 3-12 and Figure 3-13 were acquired by Mahdi Saleh (Dr. Yuri Lvov Lab, Louisiana Tech University).

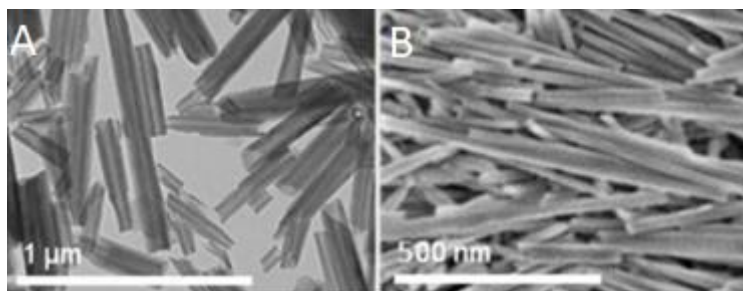


Figure 3-13: (A) TEM and (B) SEM images of Halloysite nanotubes. The images were acquired by Mahdi Saleh (Dr. Yuri Lvov Lab, Louisiana Tech University).

3.5.1 Thermogravimetric Analysis

Thermogravimetric analysis (TG(A)) was used to determine the changes in the sample's mass caused by its combustion. The TGA (Thermal Advantage Q50, New Castle, Delaware, United States) study was performed to demonstrate that the material was loaded and to estimate the percentage of RITC loaded in the nanotubes. HNTs loaded with RITC demonstrated a significant phase transition at 490°C compared to pure HNTs. The changes in mass during heating between loaded HNTs and unloaded HNTs yielded an estimated RITC loading of 5 ± 1 wt%. A Thermogravimetric analysis is shown in Figure 3-14, Figure 3-15, and Figure 3-16.

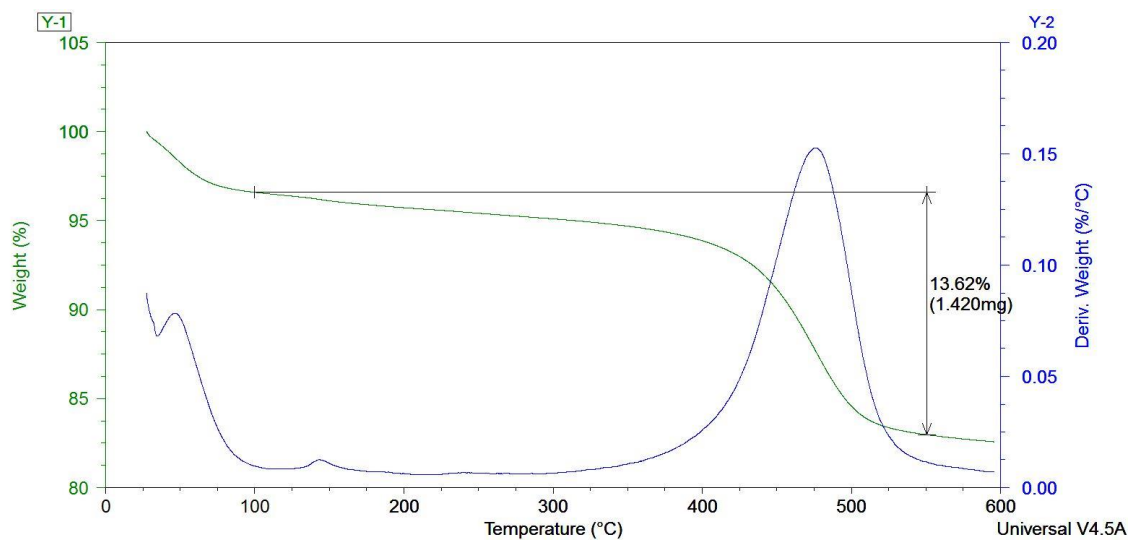


Figure 3-14: Thermogravimetric curves of pristine halloysite with no material loaded inside burns at roughly 450-500 °C. The images were acquired by Mahdi Saleh (Dr. Yuri Lvov Lab, Louisiana Tech University).

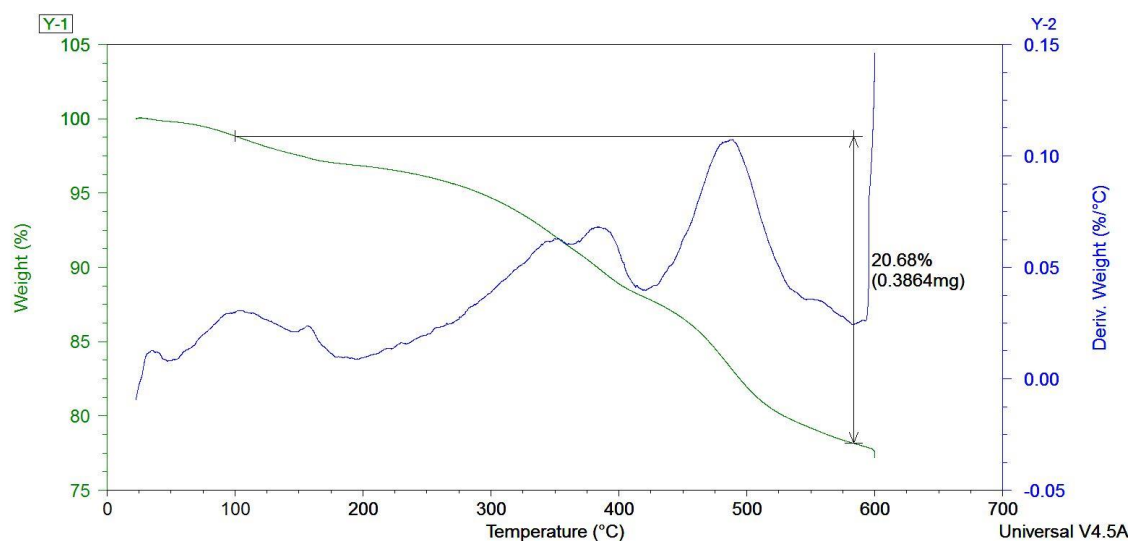


Figure 3-15: Thermogravimetric curves of diazepam loaded inside halloysite displaying the drug burning at 350-400 °C and halloysite at 450-500 °C. The images were acquired by Mahdi Saleh (Dr. Yuri Lvov Lab, Louisiana Tech University).

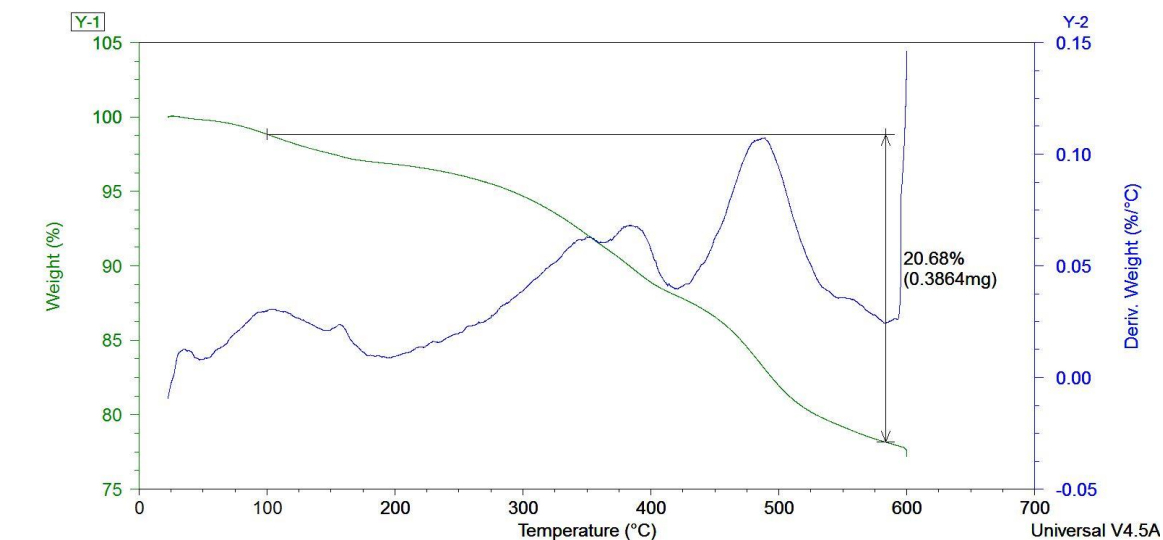


Figure 3-16: Thermogravimetric curves of RITC loaded inside halloysite displaying the substance burning at 350-400 °C and halloysite at 450-500 °C. The images were acquired by Mahdi Saleh (Dr. Yuri Lvov Lab, Louisiana Tech University).

3.6 Drug Administration Routes and Considerations

The method of drug administration is an important component that defines the drug's fate and governs its effectiveness and pharmacokinetic features [116]. To produce systemic pharmacological effects, the drug can be delivered in a variety of ways, including peroral, intranasal, intramucosal (buccal, vaginal, rectal), ophthalmic, parental (intravenous, intraperitoneal, intramuscular) and transdermal administration [117]. Medications can be delivered to mice by injections through the tail vein and, intraperitoneally, via infusion through a canula, by oral gavage, intranasal administration, intracerebroventricular (ICV), and other stereotaxic injection locations, and intrathecal injection [42], [117]–[120]. Despite the availability of different routes of drug administration, neurological disorders remain difficult to treat. Of all the potential ways oral and parental routes are the two most prominently used drug administration routes by researchers. Low bioavailability, rapid metabolism and enzymatic degradation or albumin

binding, restricted brain exposure, alteration of drugs at the BBB endothelial cells, administration of higher doses to meet the need, and adverse effects are some of the challenges encountered by oral and parental administrations [116], [121]. Figure 3-17 shows the mechanism of transport of therapeutic molecules across the BBB.

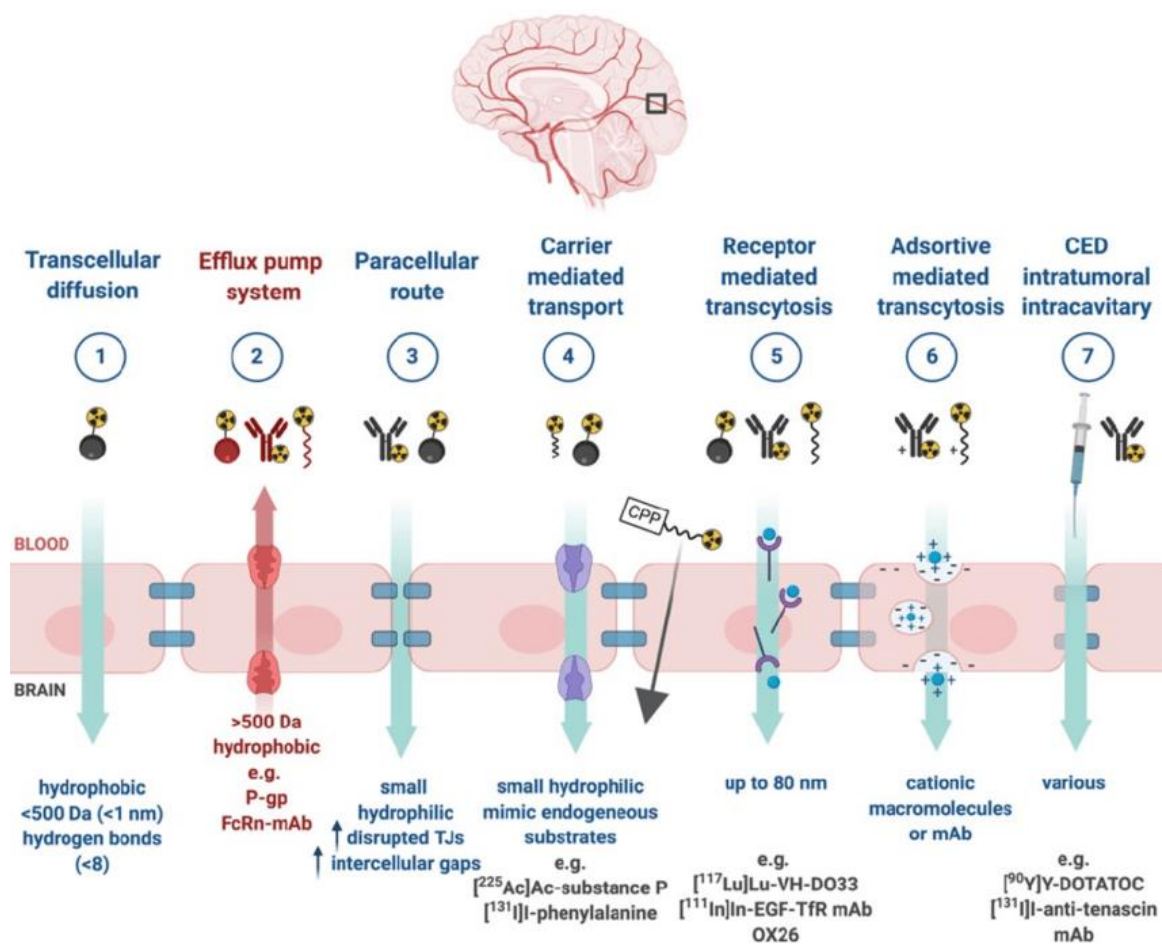


Figure 3-17: The mechanism of transport of therapeutic molecules across the BBB [122]. Abbreviations: Cell penetrating peptide (CPP), tight-junction (TJ), monoclonal antibody (mAb), conventional enhanced delivery (CED), P-glycoprotein (P-gp).

Intraperitoneal (IP) administration is a typical route of delivery in laboratory animals. It is a popular method of administration because it is simple, rapid, and easy to master, as well as less stressful for rodents. The main concern with IP administration is

that the pharmacokinetics and distribution mechanism of the medication are poorly understood [123]. Most medications that enter systemic circulation (parental administration) or the gastrointestinal tract (oral administration) undergo enzymatic breakdown, resulting in a shortened half-life [124]. Proteins and small peptides are primarily absorbed in the small intestine; however, stomach acids degrade peptides even before reaching the small intestine [116], [124]. ICV and other direct administrations necessitate a high level of competence or surgery, and there is a high likelihood of undesirable scarring and mild injuries at the site, jeopardizing patient safety [118]. However, direct delivery makes treatments available in high concentrations and minimizes drug metabolism [120]. Despite the presence of metabolic enzymes in the lungs, medicines delivered via the pulmonary route are more readily absorbed due to the enormous surface area of the lungs for absorption [125].

Due to the limited bioavailability of the peroral and mucosal routes, the parental route is the well-established method of administration for peptide medicines. The peptide disintegration by gastric acids, poor permeability, hepatic clearance, brush boundary of intestines, luminal and cytosolic metabolism, and poor permeability all contribute to the decision to provide the peptide via the parental route in this study. However, the short half-lives of the peptides necessitate repeated dosage, adding to the discomfort and pain already caused by needles [116], [126]. This motivates scientists to discover innovative methods for delivering these peptides with reduced side effects and enhanced bioavailability. Before selecting the route of administration, it is essential to comprehend the mechanisms of absorption of each medicine. NP's such as P_gP, and HNTs are utilized in this study to selectively deliver the medicine to minimize solubility, degradation,

metabolism issues, and specificity. Studies indicate that NPs delivered via parental, oral, and intravenous routes successfully reach the brain and other organs [127]. Furthermore, these enable controlled drug release which reduces the number of times a drug is delivered.

3.6.1 Anatomy and Rationale for Intranasal Administration

Intranasal administration of drugs to the brain comes with numerous advantages that outweigh many drawbacks associated with parental, oral, and transmucosal administrations. IN administration is a noninvasive route that absorbs medication from the nasal cavity to the brain parenchyma via the trigeminal and olfactory [121]. IN has numerous advantages, including self-administration (for humans) and ease of administration, noninvasiveness, BBB-passage, and quick onset of the action. Additionally, the high vasculature in the nasal cavity and the exclusion of first-pass clearance and gastric acids breakdown make IN advantageous to other routes[128]. However, some of the medications may induce nasal discomfort, and the supply of large-molecule drugs is limited [129]. Recent research has demonstrated that most small peptide medicines and nano molecules when formulated correctly are readily absorbed via nasal administration.

Figure 3-18 depicts the anatomy of the rodent nasal cavity and the pathways of drug transport to the CNS [130]. The intranasally injected drug (represented in yellow) is absorbed by the sensory neurons of nearby organs, including the Gruenberg ganglion, septal organ (shown by green arrows), ventro nasal organ (represented by red arrows), and olfactory epithelium (blue arrows). All substances absorbed through organs other than the ventro-nasal organ travel directly to the granule cells of the olfactory lobe, from

there the drug enter the rostral migratory stream (RMS) (yellow arrows) and some medication through the olfactory track (blue and red arrows at the base of the midbrain) to reach the third ventricle close to the hippocampus. Materials absorbed through the ventro-nasal organ directly reach the olfactory lobe and follow the olfactory track depicted by the red arrows, whereas materials absorbed by the trigeminal nerve merge directly into the olfactory track and reach the 4th ventricle through the pons and hind brain [130]. Molecules ranging between 100-700 nm are transported through intracellular epithelium and neuronal pathways while molecules smaller than 20 nm are transported through extracellular transport [131].

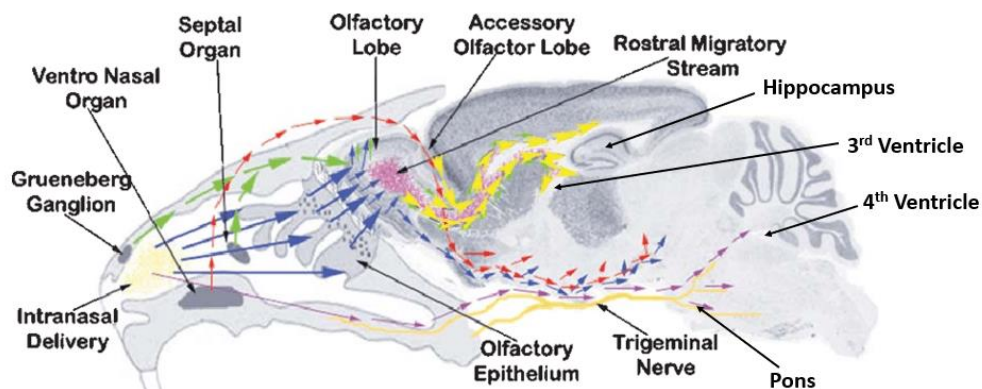


Figure 3-18: Intranasal drug transport pathways in rodents and the anatomy of the rodent nasal cavity[130]. Different color arrows indicate the routes that the yellow substance travels to reach different brain regions, including the hippocampus, the hindbrain, and 3rd and 4th ventricles after IN administration.

It is optimal to choose the administration of a drug based on its physiochemical properties and drug interaction [126]. The choice of route also depends on the amount of medication that must be supplied, the drug's solubility, its pH, and the delivery site. Since the therapeutic outcome of drug depends on route of administration, the research team must select a method, understand the rationale behind its selection, and be well-trained to

confidently employ it [132]. In addition, head posture, surgical interventions, distribution mechanism, and volume influence the pathway and deposition of the drug in the nasal passages [133]. This study used mice, whose nasal cavities have a surface area of 0.032cm^2 ; a total volume of $24\mu\text{l}$ can be supplied using around $6\mu\text{l}$ drops at a time and by switching nostrils until the entire volume is administered. A supine position with an angle of 70° or 90° is optimal for IN, and the volume of individual drops should not be excessively large, as small volume drops deposit the supplied materials in the respiratory epithelium, whereas large drops end in the nasopharynx and cause respiratory distress [121], [133], [134]. Given the size, dosage, and solubility of the medicines utilized in the study, non-invasive intranasal (IN) administration has been selected to enhance efficacy and bioavailability.

CHAPTER 4

CELL-PENETRATING MK2 INHIBITORY PEPTIDE BLOCKS LPS-INDUCED EXPRESSION OF PRO-INFLAMMATORY CYTOKINES IN HEPG2 HEPATOCYTES

This chapter in full is a previously published undergraduate conference paper cited as: Tiffany Francis¹, Durina Dalrymple², Yaswanthi Yanamadala³, Victor Carriere⁴, Scott Poh⁵, Audrey Kim⁶, Paul Kim⁷, The FASEB journal 34 (S1):1-1 doi:10.1096/fasebj.2020.34.s1.09121. This paper is reproduced here with permission from Dr. Paul Kim with minor modifications.

4.1 Abstract

Mitogen-activated protein kinase-activated protein kinase 2 or MK2 plays an important role in inflammation. We synthesized and evaluated the functionality of two selective MK2 inhibitors: anti-inflammatory peptide (AIP-1) and AIP-1 conjugated to a novel cell-penetrating peptide (CPP-AIP-1). CPP-AIP-1 reduced the expression of CXCL8 and TNF in HepG2 human hepatoma cells challenged with lipopolysaccharides (LPS), whereas AIP-1 had no significant inhibitory effect. Our results demonstrate the application of a cell-penetrating peptide to enhance drug delivery in an in vitro model of liver inflammation.

4.2 Extended Abstract

Mitogen-activated protein kinase-activated protein kinase 2 (MAPKAPK2) or MK2 is a downstream effector of the MAPK family member p38. The p38-MK2 signaling axis is well known to regulate the inflammatory response, thus it is an important target of anti-inflammatory drugs. For MK2, as with other intracellular targets, delivering the drug across the plasma membrane barrier represents a major challenge. Here we conjugate an anti-inflammatory peptide (AIP-1) selective for MK2 to a novel cell-penetrating peptide (CPP-AIP-1) to enhance intracellular delivery. We evaluated the cytotoxicity, efficacy, and intracellular uptake of these therapeutic peptides in an in vitro model of liver inflammation using HepG2 human hepatoma cells challenged with lipopolysaccharides (LPS).

HepG2 cells were treated with 0.1–1000 μM AIP-1 or CPP-AIP-1 for 24 hours to assess cytotoxicity. A significant decrease in cell viability was observed in response to 1000 μM CPP-AIP-1, whereas 1000 μM AIP-1 had no significant effect on cell viability. Treatment with either peptide at 300 μM did not alter cell viability relative to untreated control. We selected the next highest noncytotoxic dose tested - 100 μM - as the therapeutic dose.

HepG2 cells were treated for 24 hours with 1 ng/mL LPS to induce an inflammatory response and co-incubated with 100 μM AIP-1 or 100 μM CPP-AIP-1. We observed no changes in mRNA expression of the housekeeping genes ACTB, B2M and RPLP0 under any of the treatment conditions. We found that LPS significantly upregulated the mRNA expression of the pro-inflammatory cytokines CXCL8 and TNF, and that CPP-AIP-1 (but not AIP-1) co-incubation decreased expression to basal levels.

Consistent with these mRNA expression data, LPS significantly increased CXCL8 secretion, and this was inhibited by CPP-AIP-1 only. Inflammation clearly plays an important role in the development and progression of many diseases. Our results demonstrate the functionality of a cell-penetrating peptide in inhibiting the MK2-mediated inflammatory response.

4.3 Introduction

Inflammation is a normal immunological response to infection or injury. The acute inflammatory response is characterized by increased vascular dilation and permeability, leukocyte recruitment from circulation into the affected site, neutralization, or destruction of the insult, and return to homeostasis. Although inflammation is a protective response, unresolved inflammation is responsible for numerous chronic inflammatory diseases including inflammatory bowel disorder, rheumatoid arthritis, atherosclerosis, neurodegeneration, type 2 diabetes, cancer, and liver disease, to name just a few.

Inflammation is regulated by complex signaling networks within innate immune cells and resident cells that orchestrate immune responses through the release of inflammatory mediators [135]. Mitogen-activated protein kinases (MAPKs) play significant roles in this process by linking the receptors that sense insults to downstream effectors [136]. The present study focuses on inflammation regulated by the p38 MAPK family. Once activated by inflammatory mediators or environmental stresses, p38 can phosphorylate and activate numerous substrates to promote the inflammatory response. Because p38 regulates multiple cellular processes, p38 inhibitors tend to have adverse side effects. The p38 substrate MAPK-activated protein kinase 2 (MAPKAPK2) or MK2

has attracted attention as a potential anti-inflammatory drug target. A recent review of the literature [137] summarizes the pathological role of MK2 in chronic inflammatory diseases.

To act on intracellular targets such as MK2, inhibitors need to cross the plasma membrane barrier. Cell-penetrating peptides (CPP) are short sequences (5–30 amino acid residues) that have been widely used to carry diverse cargo (proteins, nucleic acids, chemotherapeutic drugs, and other compounds) into cells [138]. The aim of this study was to investigate the effects of conjugating a novel CPP to a selective peptide inhibitor of MK2 described previously by Hayess and Benndorf (1997)[139], which we refer to as anti-inflammatory peptide-1 or AIP-1. We evaluated the cytotoxicity, efficacy, and intracellular uptake of the therapeutic peptides in an in vitro model of liver inflammation using the HepG2 human hepatocellular carcinoma cell line challenged with lipopolysaccharides (LPS) to induce an inflammatory response. Our results demonstrate the functionality of the cell-penetrating peptide in inhibiting the MK2-mediated inflammatory response.

4.4 Methods

4.4.1 Anti-inflammatory Peptide Synthesis

Therapeutic peptides (AIP-1 and CPP-AIP-1) were synthesized on Knorr resin by 9-fluorenylmethoxycarbonyl (Fmoc) solid phase methodology (Poh, Lin, Panitch 2015). Knorr resin was swollen with dichloromethane (DCM) followed by dimethylformamide (DMF). A solution of 25% piperidine in DMF was added to the resin, and argon was bubbled for 15 minutes. The resin was washed with DMF (3×) and isopropyl alcohol (i-PrOH, 3×). A solution of Fmoc-amino acid (3 equiv), (1H-

benzotriazole-1-yl)-1,1,3,3-tetramethyluronium hexafluorophosphate (HBTU, 3 equiv), N-hydroxybenzotriazole (HOBT, 3 equiv) and N,N-Diisopropylethylamine (DIPEA, 5 equiv) in DMF was added for amino acid coupling. Argon was bubbled for 2 hours, and the resin was washed with DMF (3×), DCM (3×) and i-PrOH (3×). To deprotect Fmoc, a solution of 25% piperidine in DMF was added to the resin, and argon was bubbled for 20 minutes, the solvent was removed, and the resin was washed with DMF (3×) and i-PrOH (3×). The above sequence was repeated for coupling of amino acid sequence. Final compound was cleaved from the resin with a cocktail of trifluoroacetic acid (Sigma-Aldrich), triisopropyl silane (TCI Americ(A), ethane dithiol (Alfa Aesar), and Milli-Q water. The cleaved mixture was concentrated under vacuum. The concentrated product was immediately precipitated in ether, recovered by centrifugation, solubilized in Milli-Q water, and lyophilized. Peptides were purified on FPLC AKTA Explorer (GE Healthcare) with a 22/250 C18 prep-scale column (Grace Davidson) and an acetonitrile gradient with 0.1% trifluoroacetic acid. Peptide molecular weight was confirmed by matrix-assisted laser desorption ionization time-of-flight (MALDI-TOF) mass spectrometry with a 4800 Plus MALDI TOF/TOF Analyzer (Applied Biosystems).

4.4.2 Cell Culture

HepG2 liver cells (ATCC) were cultured in EMEM containing 10% FBS at 37 °C and 5% CO₂. Cells between passage numbers 7–11 were seeded into 96-well plates for cell viability (15,000 cells/well) and microscopy (10,000 cells/well) studies and 6-well plates (450,000 cells/well) for RT-qPCR and ELISA studies. Cells were allowed to rest for 48 hours and reach approximately 80–90% confluence prior to treatment.

4.4.3 Cell Viability

Cells were treated for 24 hours with doses of AIP-1 and CPP-AIP-1 ranging from 0.1–1000 μ M or 1 ng/mL LPS from *E. coli* O55:B5 (Calbiochem). Cell viability was measured using Cell-TiterGlo 2.0 (Promega). Only cells in the inner wells were assayed in order to minimize edge effects.

4.4.4 RNA Isolation and RT-qPCR

Cells were treated for 24 hours with 100 μ M AIP-1 or CPP-AIP-1, alone or in combination with 1 ng/mL LPS. Cells were harvested in Trizol (Invitrogen) and total RNA was isolated using PureLink RNA Mini kit (Invitrogen). Total RNA concentration and purity were quantified by measuring A260/280 using a SimpliNano spectrophotometer (GE Healthcare Life Sciences). All sample A260/280 values were 1.9–2.1. Total RNA was treated with DNase I and 250 ng were reverse transcribed in a 20 μ L reaction volume using gDNA Clear cDNA synthesis kit (Bio-Rad). For no-RT control, all RNA samples were pooled, and 250 ng of the pooled RNA was used in the reaction. The expression of CXCL8 and TNF mRNA was measured by qPCR using SsoAdvanced Universal SYBR green supermix on a CFX Connect instrument running CFX Manager 3.1 (Bio-Rad). The equivalent of 1 μ L of the produced cDNA (or no-RT control or no-template control) was amplified in a 20 μ L reaction volume using specific primers (Integrated DNA Technologies). Thermocycling conditions were as follows: initial denaturation at 95 °C for 30 seconds followed by 40 cycles of 95 °C for 10 seconds and 58 °C for 30 seconds. After amplification, primer specificity was verified by melting curve analysis of amplicons. There were no amplification products in the no-RT and no-template controls. Cq values were determined by auto-calculation of threshold using CFX

Manager. Cq values of target genes were normalized to 3 stably expressed reference genes. Fold-change in mRNA expression relative to control was calculated as $2^{-\Delta\Delta Cq}$. Primer sequences are listed in Table 4-1. Primers were designed to span exon-exon junctions (not possible for B2M) and screened in-silico using BLAST.

Table 4-1: Primers used for the RT-PCR Test in Hepatocytes

<i>Gene symbol</i> <i>Gene name (alias)</i>	<i>Accession No.</i>	<i>Primer sequences</i> <i>Forward</i> <i>Reverse</i>	<i>Amplicon size (bp)</i>
<i>CXCL8</i> C-X-C motif chemokine ligand 8 (IL-8)	NM_000584.4	F: CTTGGCAGCCTTCCTGATTT R: GGGTGGAAAGGTTTGGAGTA TG	111
<i>TNF</i> tumor necrosis factor (TNF α)	NM_000594.4	F: CCAGGGACCTCTCTCTAATCA R: TCAGCTTGAGGGTTTGCTAC	106
<i>ACTB</i> actin beta (β -actin)	NM_001101.5	F:CACTCTTCCAGCCTTCCTTC R:GTACAGGTCCTTTCGGGATGT	104
<i>B2M</i> beta-2- microglobulin	XM_005254549.3	F:CCAGCGTACTCCAAAGATTC A R:TGGATGAAACCCAGACACA TAG	94
<i>RPLP0</i> ribosomal protein lateral stalk subunit P0	NM_001002.4	F:GGAGAAACTGCTGCCTCAT ATC R:CAGCAGCTGGCACCTTATT	107

4.4.5 ELISA

Cell culture media supernatants from the RT-qPCR studies were collected at 4 °C and stored in aliquots at -80 °C until later analysis. Detection of CXCL8 and TNF cytokines in the supernatant was carried out using ELISA kits (Boster Bio, Cayman

Chemical). Sample aliquots were thawed on ice and assayed on one 96-well plate for each assay.

4.4.6 Fluorescence Microscopy

Cells were incubated for 24 hours with 100 μ M fluorescein-labeled AIP-1 (AIP-1F) or fluorescein-labeled CPP-AIP-1 (CPP-AIP1-F). After washing with medium to remove any unbound peptides, cells were imaged via fluorescence microscopy (BioTek Cytation Multi-Mode Imaging Reader) and fluorescence intensity was quantified using ImageJ.

4.4.7 Statistical Analysis

Assays were conducted with triplicate (cell viability) or duplicate (RT-qPCR and ELISAs) technical replicates for each of 3 biological replicates ($n = 3$). Data were analyzed by two-way ANOVA followed by Sidak's multiple comparisons test (cell viability) or ordinary one-way ANOVA followed by Tukey's multiple comparisons test (RT-qPCR and ELISAs) using GraphPad Prism 7.05. Data are shown as mean with SEM.

4.5 Results

4.5.1 Cell Viability

After 24 hour treatment, a significant decrease in cell viability was observed with 1000 μ M CPP-AIP-1 (Figure 4-1). There was a slight decrease with 1000 μ M AIP-1 that was not statistically significant. Treatment with LPS at 1 ng/mL had no effect on cell viability (data not shown).

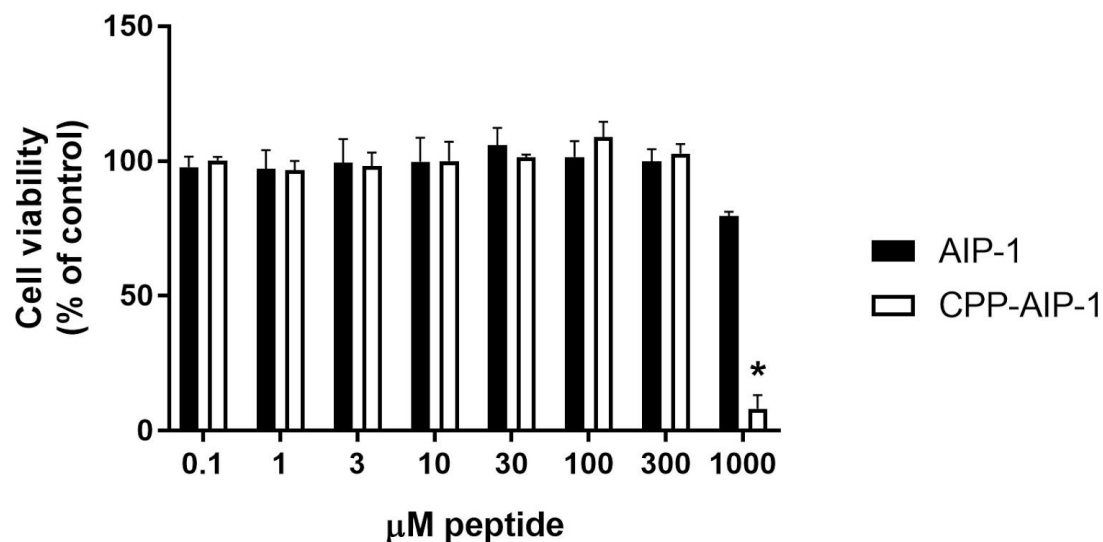


Figure 4-1: Cellular ATP was assayed as a measure of cell viability after 24-hour treatment with the indicated concentrations of peptides. Data are expressed as % of untreated control. (* indicates $p < 0.0001$). $n = 3$

4.5.2 Gene Expression

Based on the dose-response where peptide concentrations $\leq 300 \mu\text{M}$ had no effect on cell viability or morphology (data not shown), we selected $100 \mu\text{M}$ as the treatment dose. After 24 hour treatment with $100 \mu\text{M}$ of the peptides alone, or in combination with 1 ng/mL LPS, there was no effect on the mRNA expression of the reference genes ACTB, B2M, and RPLP0 (Figure 4-2).

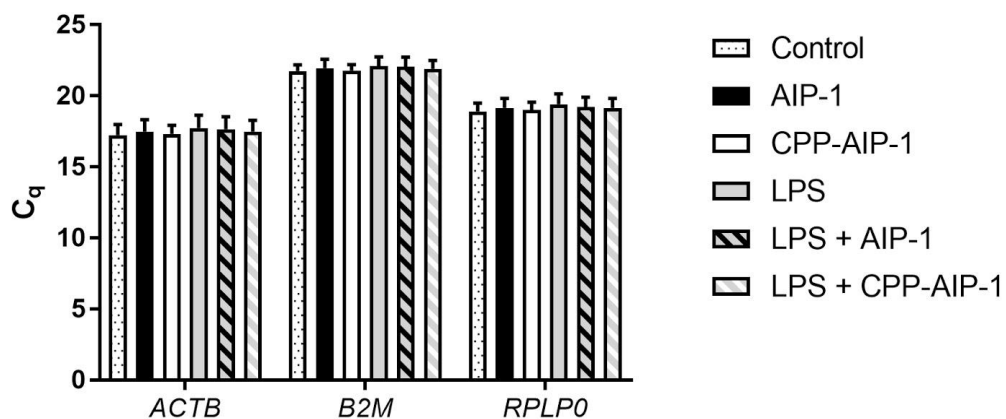


Figure 4-2: The suitability of three potential reference genes was assessed by RT-qPCR after 24 hour incubation with the indicated treatments (100 μ M AIP-1, 100 μ M CPP-AIP-1, 1 ng/mL LPS, or combination). $n = 3$

In contrast, LPS significantly upregulated expression of both CXCL8 (2.41-fold) and TNF (13.72-fold) mRNA relative to untreated control after normalization to the reference gene panel (Figure 4-3). LPS induction of CXCL8 and TNF mRNA was blocked by co-incubation with 100 μ M CPP-AIP-1. Co-incubation with 100 μ M AIP-1 blunted the induction but this did not reach statistical significance. The peptides without LPS had no effect on the expression of these genes.

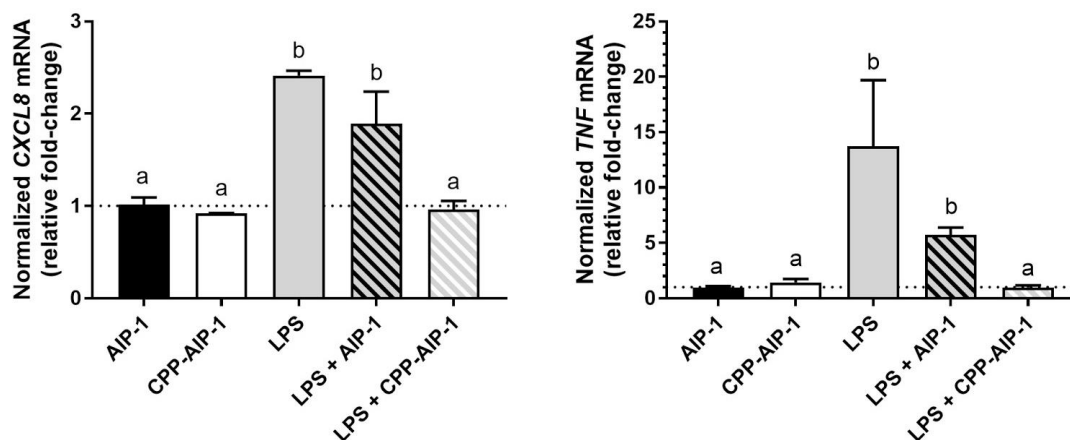


Figure 4-3: Expression of *CXCL8* (left) and *TNF* (right) mRNA was quantified by RT-qPCR after 24 hour incubation with the indicated treatments (100 μ M AIP-1, 100 μ M CPP-AIP-1, 1 ng/mL LPS, or combination). Data are normalized to 3 reference genes and expressed as relative fold-change of untreated control (horizontal dash represents control expression). Bars with different letters indicate a statistically significant difference ($p < 0.05$). $n = 3$

4.5.3 ELISA

We measured cytokine levels in the cell culture media supernatants collected from the same cell cultures analyzed by RT-qPCR. LPS significantly increased CXCL8 detected in the media (1552 pg/mL) relative to untreated control (985 pg/mL) (Figure 4-4). Similar to the results for CXCL8 mRNA expression, CPP-AIP-1 (but not AIP-1) at 100 μ M inhibited CXCL8 secretion to control levels. TNF was not detected in any of the samples.

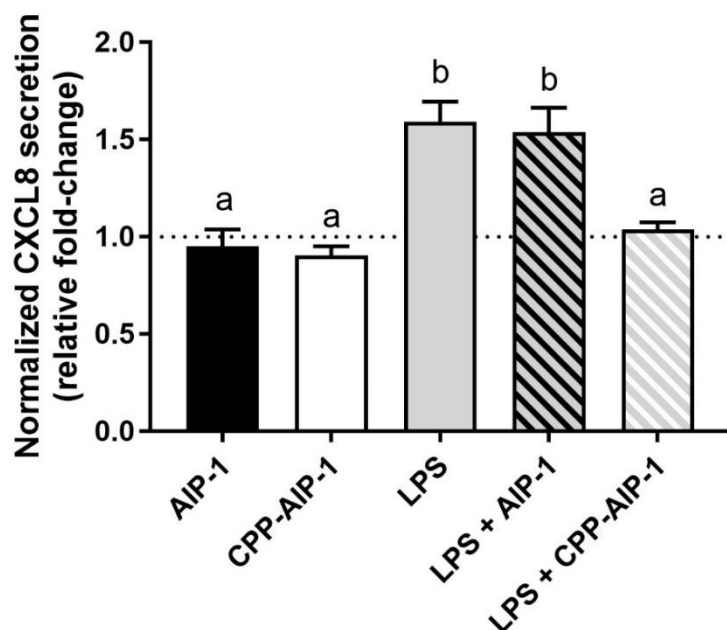


Figure 4-4: Secreted CXCL8 was quantified by ELISA after 24-hour incubation with the indicated treatments (100 μ M AIP-1, 100 μ M CPP-AIP-1, 1 ng/mL LPS, or combination). Data are expressed as relative fold-change of untreated control (horizontal dash represents control level). Bars with different letters indicate a statistically significant difference ($p < 0.05$). $n = 3$

4.5.4 Intracellular Uptake

The ability of the cell-penetrating peptide (CPP) to deliver the therapeutic peptide (AIP-1) across the plasma membrane was tested by comparing AIP-1 and CPP-AIP-1 tagged with fluorescein. Enhanced intracellular uptake of CPP-AIP-1 was visually confirmed using fluorescence microscopy (Figure 4-5 and Figure 4-6).

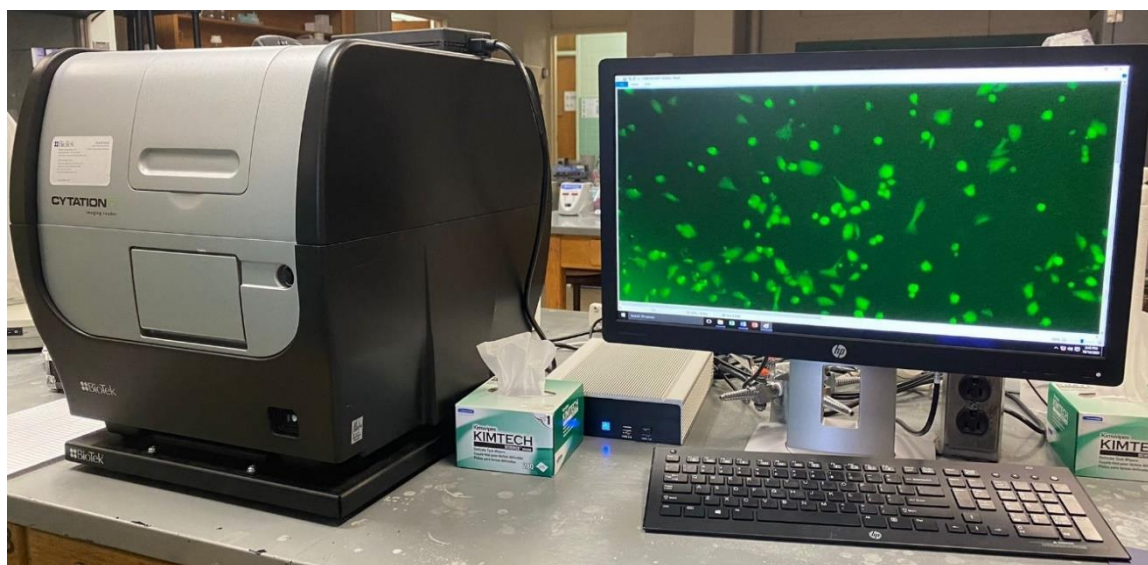


Figure 4-5: Fluorescence image reader (Biotek- Cytation image reader)

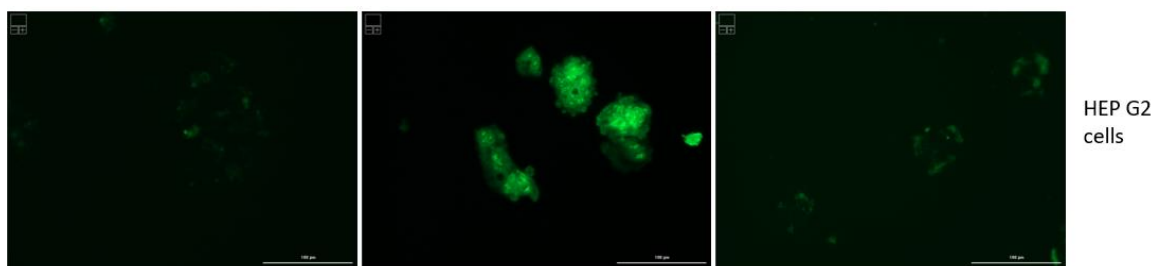


Figure 4-6: Fluorescence images of HEP G2 cells treated with 200 μ M concentration AIP-1 (left image), KAFAK-AIP-1 (CPP conjugate) (middle image), and R8 (positive control) (right image) for 4hours. AIP-1 treated cells showed no uptake of the peptide while KAFAK-AIP-1 showed enhanced uptake. R8 at this concentrations has shown high cytotoxicity in the cells.

These peptides are examined in a few other cell lines to evaluate their intracellular uptake and localization. Various cell lines, including macrophages (RAW, J774), neuronal cells (SHEP), and hepatocytes (HEPG2), were investigated in vitro to compare the uptake of CPPs to the therapeutic peptide. The therapeutic efficacy of the CPP-conjugate is evaluated to ensure that the conjugation of the therapeutic peptide to the cell-penetrating sequence does not compromise the peptide's therapeutic efficacy. To

visualize and image the uptake and translocation of fluorescently labeled peptides, a fluorescent microscope (Biotek-Cytation image reader; see Figure 4-7) was utilized.

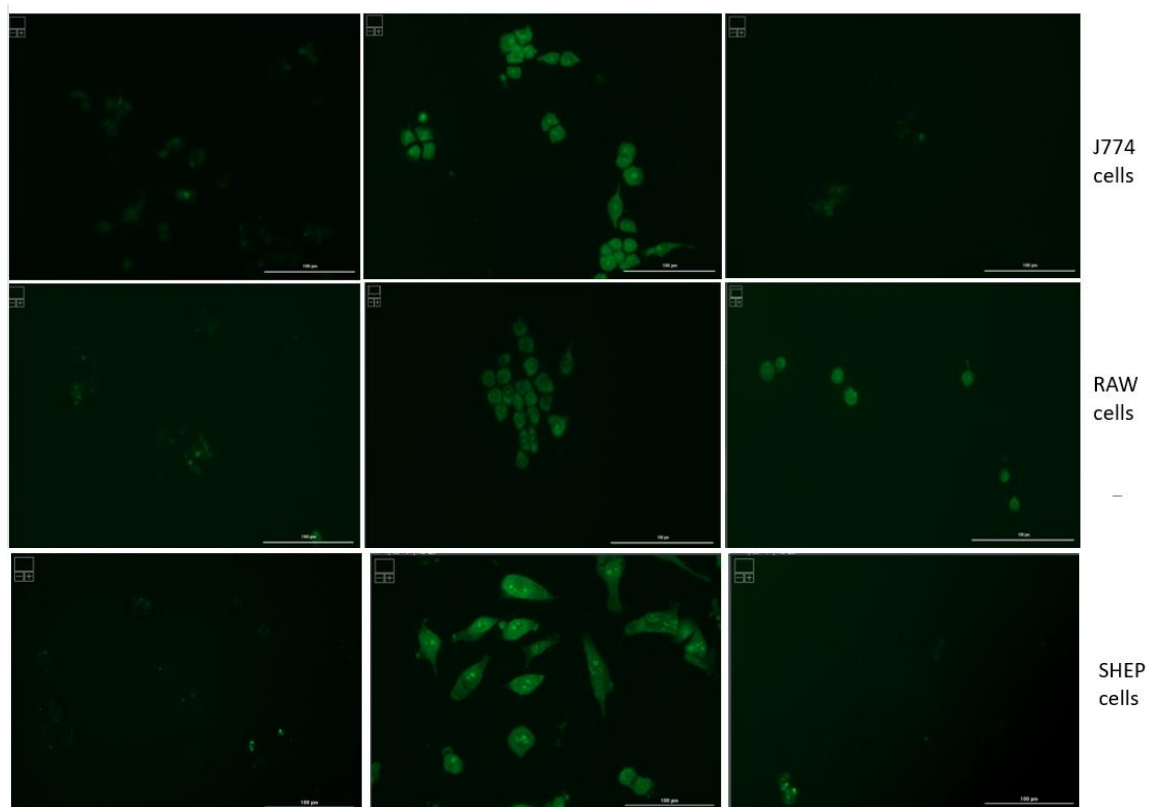


Figure 4-7: J774 (macrophages), RAW (macrophages), and SHEP (neuronal cells) treated with 200 μ M concentrations of AIP-1 (first row), KAFAK-AIP-1 (CPP conjugate) (second row), and R8 (positive control) (third row) for 4 hours. AIP-1 treated cells exhibited less peptide absorption than KAFAK treated cells, although R8 at the dose exhibited severe cytotoxicity in the cells.

4.6 Discussion

LPS-induced inflammation is mediated by toll-like receptor 4 (TLR4), which recognizes the pathogen-associated molecule and triggers a signaling cascade that eventually activates the mitogen-activated protein kinase (MAPK) p38. MAPK-activated protein kinase 2 or MK2 is an effector kinase downstream of p38 that has been shown to be central to LPS induction of TNF [140]. MK2 promotes proinflammatory cytokine

biosynthesis by phosphorylating and inactivating tristetraprolin (TTP), a protein that binds and destabilizes many cytokine mRNA. Both TNF and CXCL8 are known to be regulated post-transcriptionally in this manner [141], [142]. Consistent with this LPS/TLR4/p38/MK2/TTP pathway, we found that LPS significantly increased CXCL8 and TNF mRNA expression and that this was blocked by a cell penetrating MK2 inhibitory peptide (CPP-AIP-1). The inhibitory peptide by itself (AIP-1) did not significantly inhibit expression, highlighting the effectiveness of cell penetrating peptides as a drug delivery mechanism.

We quantified both basal and LPS-induced TNF mRNA in the cell lysate but did not detect secreted TNF in the cell culture media using a commercial ELISA kit (Cayman Chemical TNF- α (human) ELISA kit 589201) within the limit of detection (3.9 pg/mL TNF). This result was unexpected because LPS has been shown to induce TNF expression and secretion in liver tissue and liver cell lines including HepG2 [143], [144]. However, others have also reported TNF mRNA expression in LPS-stimulated HepG2 in the absence of detectable cytokine in the media [145]. The discrepancy may simply be due to differences in detection methods or may be related to the kinetics of inflammation. A limitation of the present study is that gene expression and cytokine secretion were measured at a single time point 24 hours after LPS challenge.

CHAPTER 5

CELL PENETRATING ANTI-INFLAMMATORY PEPTIDE (KFAK) PROMOTES EFFICIENT UPTAKE AND INHIBITION OF PRO-INFLAMMATORY CYTOKINES IN PRIMARY BRAIN CELLS IN VITRO: A PROMISING CNS CANDIDATE

5.1 Introduction

The CNS was thought to be immune privileged until a decade ago, not contributing to the inflammatory response and being resistant to inflammatory molecules. This assumption was revised as evidence demonstrated for the ability of the CNS to exhibit immune response to infection, injury, and diseases [146]. However, like systemic inflammatory mediators the CNS derived immune molecules also play a dual role, with both beneficial and deleterious effects [146]. Neuronal inflammation is known to play a key role in development of several neurodegenerative diseases including Alzheimer's disease, traumatic brain injury (TBI), Parkinson's disease, Huntington's disease, amyotrophic lateral sclerosis, multiple sclerosis, and spinocerebellar ataxia [41], [146]. Recent studies have also shown that inflammatory mediators have psychological effects, and developmental delays in infant brain and that they also play an essential part in brain development [146]. Despite the evidence of the involvement of inflammation, treating CNS diseases remains challenging as the BBB restricts the transit of most potential therapeutics.

Cell penetrating anti-inflammatory peptide (KAFAK) has a potential to inhibit pro-inflammatory cytokines $\text{TNF}\alpha$ (tumor necrosis factor) and IL-6 (interleukin-6). Excessive production of these cytokine molecules can participate in deleterious effects and cause inflammatory diseases like osteoarthritis, rheumatoid arthritis, ulcerative colitis, ischemic perfusion, atherosclerosis etc. [124]. The pro-inflammatory cytokines $\text{TNF}\alpha$, Interleukin-1 (IL-1), IL-6 under undesirable conditions accelerate the damage by disrupting the surrounding normal healthy cells [12], [124], [147]. KAFAK inhibits this inflammation by targeting the MK2 (mitogen activated protein kinase) pathway that is essential for pro-inflammatory cytokine production [12], [148]. Previous studies conducted in our lab have shown that KAFAK increased uptake and reduced the expression of LPS induced CXCL8 and $\text{TNF}\alpha$ in HEPG2 cells compared to AIP-1. Studies conducted by Zhijiang et al. (2019) has shown reduced inflammation and improved outcome in spinal cord injured mice after sustained intrathecal delivery of KAFAK-BDNF (brain derived neurotrophic factor) from modified hyaluronan-methylcellulose (HAMC) hydrogel implants [98].

Cell penetrating peptides (CPP) can effectively transport across biological membranes and possess the ability to carry varied therapeutic components across these membranes. CPP's can be formed endogenously and exert biological activity themselves [149]. Most of the synthetic CPP's are synthesized to mimic the naturally available peptides. Peptidomimetics offer less toxicity and immunogenicity, increased bioavailability, specificity, and ease of scaling up production and modification to improve the pharmacological and pharmacokinetic properties. Several CPP's like Tat 47-57, penetratin, pVEC, SynB3, and transportan 10 (TP10) have exhibited potential to

traverse the BBB. However, the influx and efflux rates of these peptides vary [13], [150], [151]. The exact mechanism of BBB permeability of most CPP's and the distribution of these peptides once the BBB is crossed are not clearly known and these appear diverse between each peptide. Potential mechanisms of these cationic molecules circumvent the BBB by transcellular transport include adsorptive mediated transcytosis (AMT), receptor mediated transcytosis (RMT), and passive transport [56], [122], [152]. The mechanism of transport depends on the choice of peptide vectors, physiochemical properties of the peptide and the route of administration [56], [129], [133]. For example, RMT peptides like L57 are transported by binding to the LRP1 (low-density lipoprotein receptor-related protein 1) receptor binding. LRP1 receptors are highly expressed in brain endothelial cells that line the BBB [80]–[82]. CPP's nonspecifically cross the BBB, generally by adsorptive mediated endocytosis [56], [151].

Neuropharmaceuticals are gaining much interest with the increase of CNS disease-related cases each year and understanding the mechanisms of CNS diseases is opening doors for development of therapeutics with more targeted approaches [30]. The therapeutics are aimed at multi-model disease targeting, as a majority of neuronal diseases are multifaceted. CNS diseases are in urgent need of therapeutics and potent vector that could effectively transport the drugs [151]. However, the BBB, poor pharmacokinetics of many drugs, and enzymatic degradation of the drugs by the endothelial cells of BBB still remain as major hurdles. There are more than 70 therapeutic peptides available in the market and many more in clinical trials [153]. Regardless, most of these peptides are not tested for the BBB permeating abilities. However, peptide therapeutics has proven their mettle in neuronal therapy as they have many effects within the CNS. The ability of some

endogenous peptides to shuttle across the BBB provides researchers with templates to mimic the natural peptides to develop neuropharmaceuticals[78], [151].

In this study, primary rat brain microvascular endothelial cells (BMVECs) were used to visualize the intracellular uptake and localization of three fluorescently labelled peptide drugs KFAK, L57-AIP-1, AIP-1 via fluorescence microscopy. Primary BMVECs are the first structural cells of the BBB, and they possess tight junctions between cells that prevent the transport of large molecules [154]–[156]. Primary BMVECs were chosen as a model because these cells retain characteristics of in vivo endothelial cells closely mimicking the conditions of BBB which are lost in immortalized cell lines. Hence, these cells would be ideal for in vitro testing of potential therapeutic peptides for cytotoxicity and their BBB transport capabilities [155], [157]. The three peptides AIP-1 (therapeutic sequence; KKKALNRQLGVA(A), KFAK (cell-penetrating peptide with AIP-1 sequence; KFAKLAARLYRAKRLARQLGVA(A), and L57-AIP-1 (receptor mediated peptide with AIP-1 sequence; TWPKHFDKHTFYLSILKLGKH-(Beta-al(A)-LARQLGVAA-CONH₂) are compared for the uptake ability and therapeutic efficiency. Research conducted in our lab by Rodriguez et al, showed the ability of the L57 peptide to localize in the cytosol of primary BMVECs which highly express LRP1 receptors [80], [158]. The anti-inflammatory peptide, AIP-1 was used as control and all three peptides are quantified for uptake using varied concentrations. Cytotoxicity studies were conducted for the KFAK peptide. Our results showed that compared to our control peptide (AIP-1) and receptor mediated peptide (L57-AIP-1), cell penetrating peptide (KFAK) has shown better uptake even at low concentrations (20 μ M).

5.2 Materials and Methods

5.2.1 Materials

The peptides KAFK-FITC (FITC-X-NH-KKKALNRQLGVAA-COOH), L57-AIP-1 (FITC-Ahx-TWPKHFDKHTFYLSILKLGKH-(Beta-al(A)-LARQLGVAA-Amide) were custom made by Biomatik (Cambridge, ON, Canada). AIP-1 -FITC peptide was custom made by Aaptec (US). The ELISA kits are obtained through Aspire program from ThermoFisher.

5.2.2 Animal Care

Sprague Dawley rats were fed and hydrated regularly during a 12-hour day-light cycle. Dams nourished pups until they were sacrificed for the study.

5.2.3 Harvesting Primary Cells

Sprague Dawley rat pups aged 1-3 days were separated from dams and sacrificed by the cervical disarticulation method. All procedures were performed according to the protocols by Louisiana Tech University Animal Care and Use Committee. Brain cells from the cortex of these pups were separated and cultured in Ham's F12 nutrient mixture along with L-glutamate, sodium bicarbonate, horse serum, heparin and 10% fetal bovine serum [159]. The glial cells can differentiate into endothelial cells, astrocytes and or microglia with specific growth factors and media as previously described [80], [159]–[161]. The glial cells were initially purified by using 5.51 μM Puromycin (MilliporeSigma, St. Louis, MO, US). Next, purified cells were cultured in rat endothelial growth medium with endothelial growth factors for their differentiation into BMVECs.

5.2.4 Cell Culture

Early cell passages were used for this study to maintain the characteristics of the BBB endothelial cells. BMVEC's were seeded onto poly-L-lysine -coated 96 well black walled plate at 10,000 cells per well. Plates were incubated for 24 hours or until 50%-80% confluent at 37°C in 5% CO₂. Followed by treatment with different concentrations of peptide drugs AIP-1, KAFAK and L57-AIP-1 for 4 hours the cells were visualized under fluorescent microscope. For the ATP assay (Promega CellTiter-Glo 1.0) cells were treated for 24 hours with different concentrations of all three peptides to assess the potential cytotoxicity following the manufacturer's instructions.

5.2.5 Peptide Uptake and Localization

All the peptides (FITC-AIP-1, FITC- KAFAK, FITC-L57-AIP-1) used for the study are soluble in phosphate buffered saline (PBS), and 2mg/ml of each peptide was dissolved in 50 µl of PBS to make stock concentration of each. Working concentrations of the peptides (10 µl, 20 µl, 30 µl, 50 µl, 75 µl) were prepared immediately prior to use by diluting the stock concentration in endothelial cell media. Two different passages of cells were used to test each concentration in triplicate. Cells with no peptide treatment were used as controls. The media in the wells was replaced with the corresponding peptide concentration media for the treatment of cells. After treatment the plate was incubated at 37°C for 4 hours in 5% CO₂ incubators. The plate was removed from the incubator after 4 hours and washed three times with warm PBS. Gentle washes were performed to prevent losing cells and to maintain the cell membrane integrity. One more wash with PBS was performed after fixing the cells for 10 minutes with paraformaldehyde. To visualize the individual nuclei cells are stained with DAPI nuclear

counter stain. Epifluorescence images at three random areas of the well were acquired by using consistent equipment settings at 10x and 20x magnification in phase contrast, FITC (excitation: 470nm, emission: 530nm) DAPI (excitation: 358nm, emission: 461nm) filters. Leica DMI 6000B inverted microscope with Leica DP71 color camera was used for imaging.

5.2.6 ATP Assay

BMVECs were used to test the cytotoxicity of peptides at varying concentrations. Endothelial media was used to dilute peptide concentrations from stock to 10 μ M, 30 μ M, 50 μ M, 100 μ M, 250 μ M, and 500 μ M for the three peptides FITC-AIP-1, FITC-KAFAK, and FITC-L57-AIP. The cells were treated with each concentration of peptide in triplicate, while three wells served as controls and received no peptide treatment. For the cell viability test, the plate was incubated for 4 hours at 37°C and 5% CO₂ according to the instructions on the ATP assay kit (Promega CellTiter-Glo 1.0). After 4 hours of incubation, the plate was equilibrated for 30 minutes at room temperature, the Celltiter-Glo substrate and buffer were combined, and 100 μ l of reagent was added to 100 μ l of peptide media. The plate was left on the shaker for two to three minutes to lyse the cells, and a Biotek Cytation image reader (Grambling state university) was used to record the luminescence.

5.2.7 Quantification of Intensity

ImageJ software was used to quantify fluorescence intensity in images of stained cells. TIFF images were acquired with the background fluorescence set to a consistent value. For each well, 20 cells were chosen at random and outlined to determine the mean fluorescence intensity in relative fluorescence units (rfu). The data were corrected by

subtracting the mean background fluorescence intensity. Each well's average mean fluorescence intensity was normalized with the mean of the negative control (vehicle treated cells). Rounded cells, which had bright autofluorescence, and undissolved fluorescently labeled peptide aggregates were excluded from the intensity measurements.

5.3 Results

5.3.1 Fluorescent Peptide Internalization

Three peptides FITC-KAFAK, FITC-L57-AIP, FITC-AIP were used to compare their uptake in the BMVEC's. Figure 5-1, Figure 5-2, Figure 5-3, and Figure 5-4 present images of BMVECs after 4 hours of incubation with the respective peptide concentrations. Phase contrast, DAPI, and GFP images were obtained from the same location. The cells internalize the FI-KAFAK peptide at concentrations as low as 20 μM . DAPI was used to counterstain the cells in order to visualize the nuclei. We observed that the KAFAK has diffused throughout the cell, including the nucleus. Observing BMVECs in real-time, we noticed that they took up FITC-KAFAK during the first few minutes. The concentrations beyond 75 μM were also measured, but the fluorescence intensity was too great to acquire unsaturated images, therefore they are not included here.

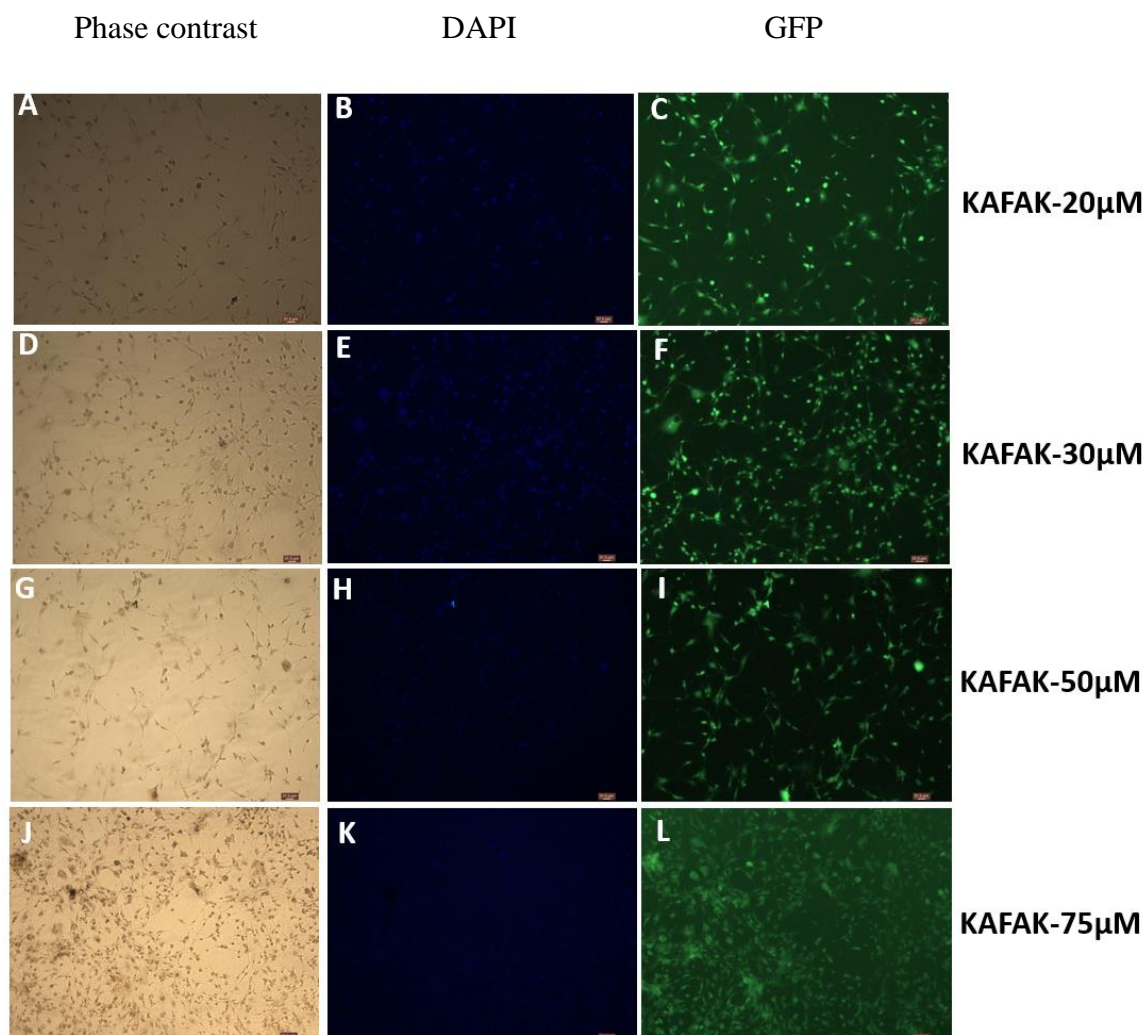


Figure 5-1: Fluorescein-labeled peptide FI-KAFAK uptake in primary BMVEC cells after 4 hours of treatment. Representative images are shown, and each row depicts the same cells. Panels A, B, and C are images of cells treated with 20 μ M of FITC-KAFAK, panels D, E, and F were treated with 30 μ M, G, H, and I with 50 μ M, and panels J, K, and L with 75 μ M. The first column (A, D, G, J) are phase contrast images, the second column (B, E, H, K) are images acquired with the DAPI filter to visualize nuclei stained with DAPI, and the third column (C, F, I, L) are images acquired with the GFP filter. The length of the scale bar is 30 μ m.

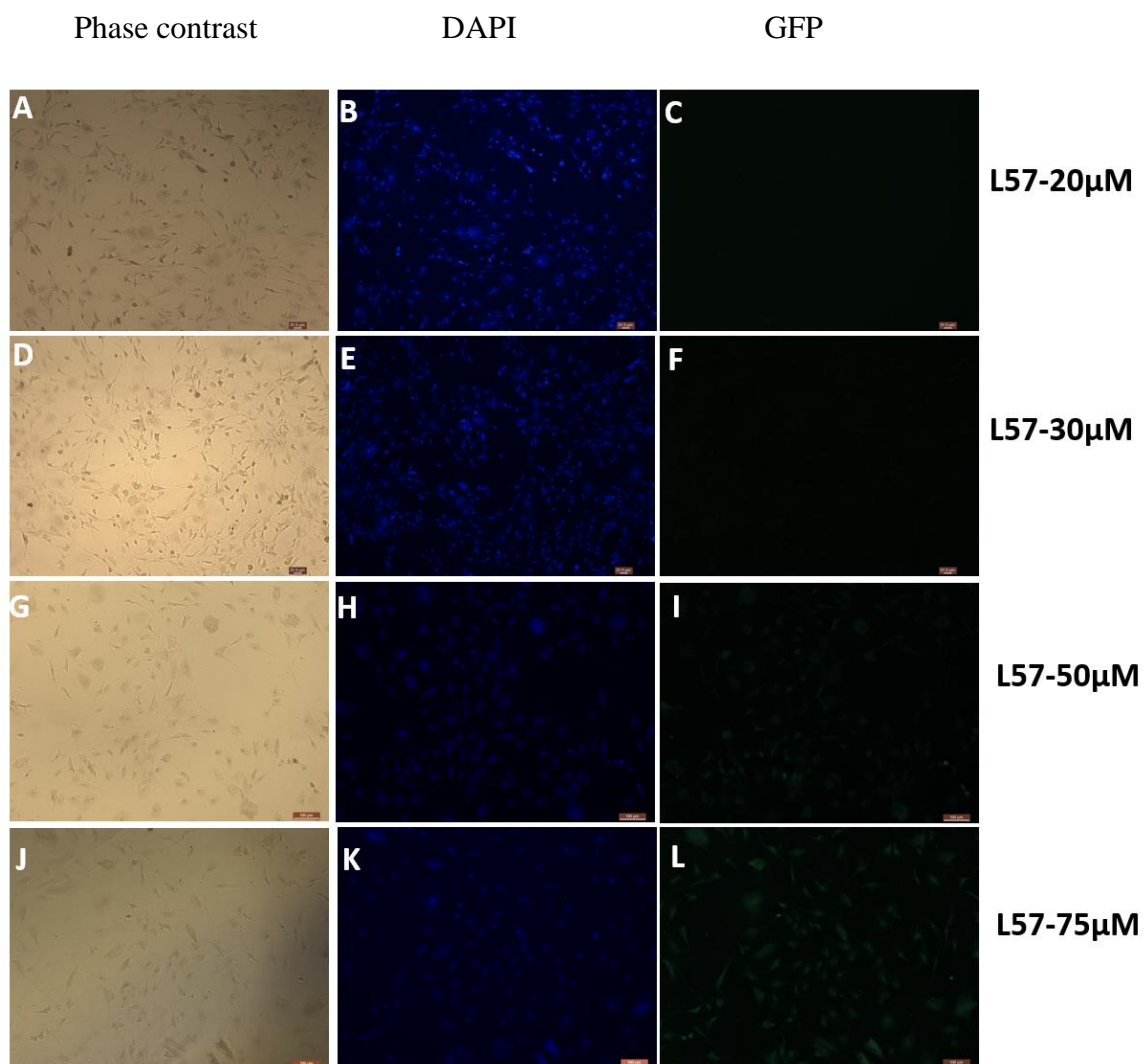


Figure 5-2: Fluorescein-labeled peptide FI-L57-AIP uptake in primary BMVEC cells after 4 hours of treatment. Representative images are shown, and each row depicts the same cells. Panels A, B, and C are images of cells treated with 20 μM of FITC-KAFAK, panels D, E, and F were treated with 30 μM , G, H, and I with 50 μM , and panels J, K, and L with 75 μM . The first column (A, D, G, J) are phase contrast images, the second column (B, E, H, K) are images acquired with the DAPI filter to visualize nuclei stained with DAPI, and the third column (C, F, I, L) are images acquired with the GFP filter. The length of the scale bar is 30 μm .

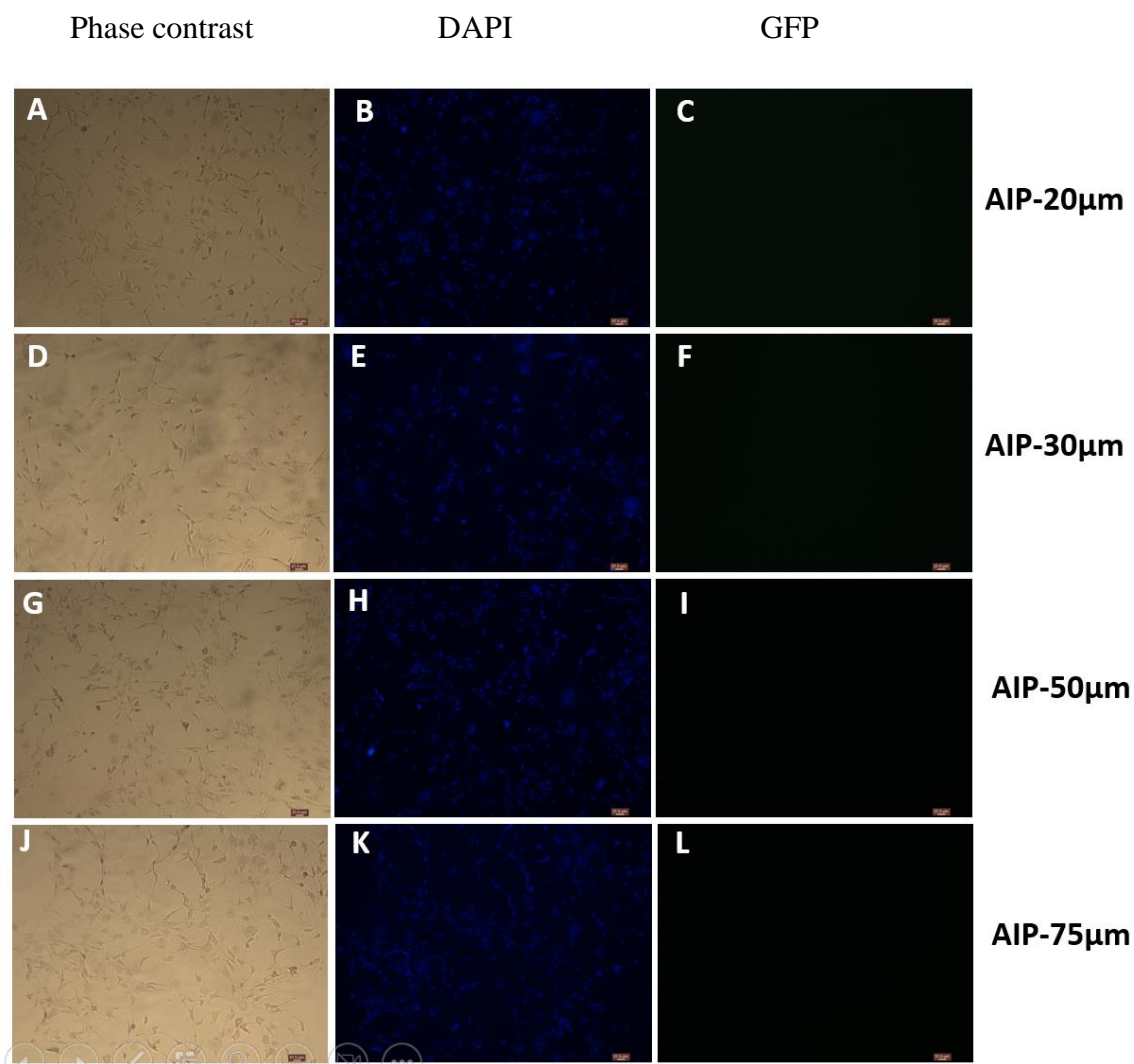


Figure 5-3: Fluorescein-labeled peptide FI-AIP uptake in primary BMVEC cells after 4 hours of treatment. Representative images are shown, and each row depicts the same cells. Panels A, B, and C are images of cells treated with 20 μM of FITC-KAFAK, panels D, E, and F were treated with 30 μM , G, H, and I with 50 μM , and panels J, K, and L with 75 μM . The first column (A, D, G, J) are phase contrast images, the second column (B, E, H, K) are images acquired with the DAPI filter to visualize nuclei stained with DAPI, and the third column (C, F, I, L) are images acquired with the GFP filter. The length of the scale bar is 30 μm .

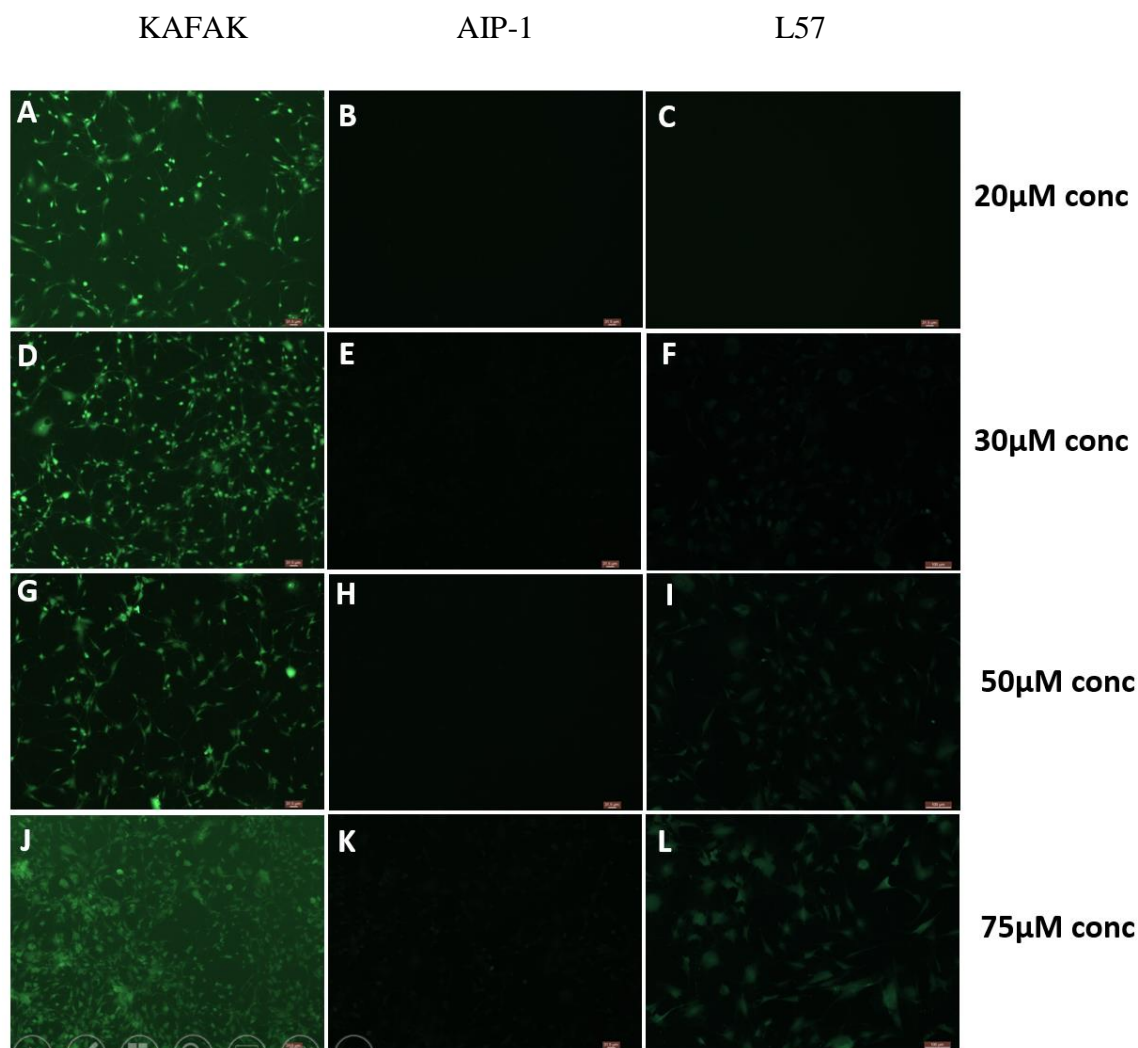


Figure 5-4: Representative images of the uptake levels FITC-labeled peptides in BMVECs after 4 hours of treatment with varying concentrations. The cells in the first column (A, D, G, J) were treated with FITC-KAFAK, the cells in the second column (B, E, H, K) were treated with FITC-L57-AIP, and the cells in the third column (C, F, I, L) were treated with FITC-AIP. The first row (A, B, C) of cells are treated with respective peptide concentrations of 20 μ M, the second row (D, E, F) are treated with concentrations of 30 μ M, the third row (G, H, I) are treated with concentrations of 50 μ M, and the fourth row (J, K, L) are treated with concentrations of 75 μ M. 30 μ m is the length of the scale bar.

FITC-L57-AIP and FITC-AIP exhibit minimal fluorescence intensity compared to FI-KAFAK when using the same image exposure time. FITC-L57-AIP displayed significant internalization when its exposure was altered. However, when consistent

settings were used to observe the fluorescence emitted by FITC-KAFAK, little was noticed. Despite high concentrations, FITC-AIP was not internalized enough to be observable. All three peptides exhibited an uptake proportional to concentration.

5.3.2 Quantification of Peptide Uptake

The fluorescence levels of FITC-KAFAK, FITC-L57-AIP, and FITC-AIP were quantified using the normalized mean intensity of FITC-KAFAK, FITC-L57-AIP, and FITC-AIP to the controls. For each peptide, four concentrations were used: 20 μM , 30 μM , 50 μM , and 75 μM . The graph illustrates the concentration-dependent fluorescence intensity of FITC-KAFAK and compares it to the other two peptides. The data suggests that the uptake is concentration dependent (Figure 5-5).

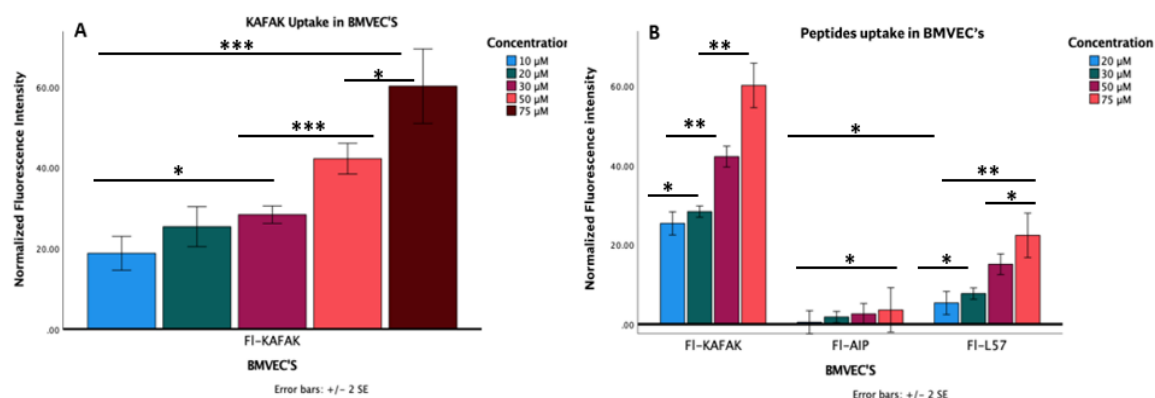


Figure 5-5: Three peptides, FITC-KAFAK, FITC-L57-AIP, and FITC-AIP, show concentration-dependent cellular uptake. (A) BMVEC's (10,000 per well) treated for 4 hours with 10 μM , 20 μM , 30 μM , 50 μM , and 75 μM concentrations of FITC-KAFAK. (B) BMVEC's (10,000/well) treated with peptides FITC-KAFAK, FITC-AIP, and FITC-L57-AIP at 50 μM and 75 μM concentrations. The mean fluorescence intensity is normalized and plotted. ImageJ software was used to analyze 20 cells per well, for a total of 120 cells ($n=6$ wells) per concentration of a peptide. ((* $P>0.05$; ** $P\leq 0.001$; *** $P< 0.05$ ANOVA with Bonferroni correction with multiple comparisons was used to evaluate the effect of concentration for Panel A and of treatment condition and of concentrations in Panel (B).

FITC-KAFAK exhibited greater internalization at 20 μM , than both FITC-L57-AIP and FITC-AIP at a higher concentration of 75 μM . FITC-L57-AIP, a receptor-mediated peptide, was successfully internalized at lower concentrations, however the uptake is modest compared to FITC-KAFAK, a CPP peptide. FITC-AIP (the therapeutic peptide in FITC-KAFAK) was, however, only marginally taken up by the cells at higher concentrations.

5.3.3 Cell Viability

As shown in the Figure 5-6 BMVECs are treated with different concentrations of the peptides AIP-1, KAFAK and L57. Both L57 and AIP has not shown any cytotoxicity until 500 μM concentration treatments for 24 hours in BMVECs. Interestingly, KAFAK treatment has reduced the cell viability of primary BMVECs at 100 μM concentration almost to 70% and further reduced the viability in a dose dependent manner.

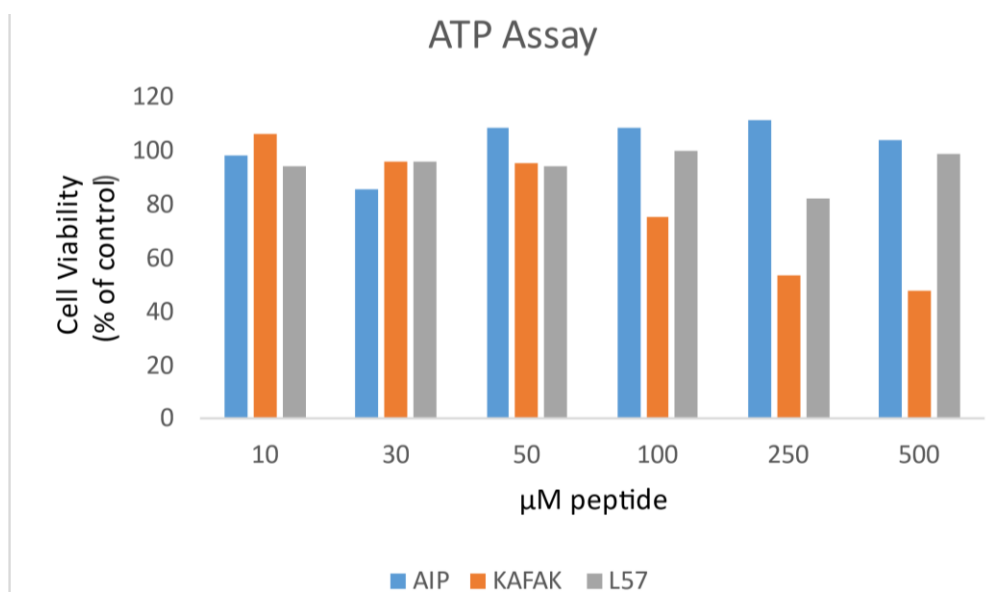


Figure 5-6: An ATP assay was used to measure cell viability in BMVECs with the indicated concentrations of peptide for 24 hours. AIP and L57 has not shown cytotoxicity on BMVECs until 500 μM concentration. KAFAK treated BMVECs at 100 μM has shown reduced cell viability and decreased viability with the increase in concentration. Data expressed as % of control (n=3) (* 0.0009).

5.4 Discussion

The BBB remains the most significant obstacle in drug development to this day [154], [162]. The KAFAK cell-penetrating anti-inflammatory therapeutic peptide has demonstrated a substantial decrease in inflammatory response (IL-6, TNF α) and a favorable effect on various illnesses, such as osteoarthritis and osteoporosis [98], [124], [163], [164]. KAFAK inhibits the production of the cytokines CXCL8 and TNF in HEP-G2 cells, as demonstrated by previous studies [165]. This peptide, when packaged in nanoparticles and hydrogels has recently demonstrated efficient anti-inflammatory abilities [98], [124], [147]. L57 is a receptor-mediated peptide that is rapidly taken up by cells with LRP1 receptors. BMVECs and primary astrocytes lining BBB express high levels of LRP1 receptors [80]. There have been numerous studies and comparisons between various CPPS and receptor-mediated peptides [164], [166]. This is the first attempt to compare CPP and RMT peptides. These peptides have been studied in our lab and compared to other peptides such as R8 and A7, they have demonstrated superior absorption in several cell lines [44]. This is also the first study to examine KAFAK uptake in an in vivo BBB model employing primary cells that closely resemble the systemic environment.

Conjugation of AIP-1 to the CPP (KAFAK) resulted in superior internalization compared to AIP-1 alone and when AIP-1 was conjugated to RMT peptide, (L57). None of the three peptides exhibited cytotoxicity until they were administered in higher concentration. In contrast to L57-AIP and AIP-1, KAFAK demonstrated some toxicity when administered in large dosages. This may be because, compared to the other two peptides, the cells quickly took up a larger amount of KAFAK as seen in its higher

fluorescence intensity at low concentrations. This suggests that CPP-conjugated peptide therapeutics may only need low concentrations for in vivo treatment cross the BBB and exert their action on the target tissue. In contrast, it was necessary to administer much higher concentrations of RMT-conjugated peptide [84]. Based on the rapid cellular penetration shown in cultured cells and low cytotoxicity at low concentrations, this study could be extended to in vivo studies. Overall, we established that KAFAK has the potential to be an effective carrier for crossing the BBB and assessing its influence on CNS-related illnesses.

CHAPTER 6

CELL PENETRATING ANTI-INFLAMMATORY PEPTIDE (KAFAK) EFFICIENTLY CIRCUMVENT THE BLOOD BRAIN BARRIER AND CURTAIL THE INFLAMMATION IN TRAUMATIC BRAIN INJURY MICE MODEL IN VIVO

6.1 Abstract

Incidence of traumatic brain injury (TBI) has been increasing worldwide affecting all age groups. The complex multifactorial secondary injury is throwing challenges to the pharmaceutical world. Despite many advancements in theragnostic agents' complexity of TBI, BBB, lack of understanding of underlying mechanisms and poor pharmacokinetics of most CNS targeted drugs further exacerbate the situation. Over the last decade, peptide molecules are taking lead in CNS therapy owing to their simplicity, low immunogenicity and toxicity, bioavailability, and ease of modifications. Arginine rich cell penetrating peptides are shown to be permeable to the BBB. However, these molecules (R11, TAT, CTP) are showing considerable levels of toxicity. This calls for peptide molecules that effectively carry therapeutic molecules escaping enzymatic degradation by BBB endothelial cells and with negligible cytotoxicity. Previous studies conducted in our lab showed KAFAK, a cell penetrating anti-inflammatory peptide has effectively up taken by the primary endothelial cells and showed promising therapeutic efficiency in in vitro BBB model. This study is extended to in vivo TBI model to test the results.

6.2 Introduction

Traumatic brain injury (TBI), man's most complex pathological disease is having great socioeconomic impact affecting millions of individuals and their families around the world [38], [159], [160]. Primary injuries caused at the time of traumatic event can only be prevented with caution and care. However, due to the lack of appropriate guidelines to assess the severity, except for use of grading scales and imaging tools that detect the minor disruptions in the brain that would later develop into major pathological conditions is a major challenge associated with secondary injuries. The development of secondary injury is multifactorial and require drugs that could not only potentially cross the BBB but also target multiple mechanisms of the injury processes [53], [160], [161]. Inflammation, edema, hypoxia, disruption of BBB, ROS, altered neurotransmitters production (excitotoxicity) and other biochemical changes are known to contributing factors [22], [55].

Inflammation is a vital biological response to protect the body from external stimuli. However, when these molecules are activated inappropriately or in certain pathological conditions, they participate in further aggravating the condition or accelerate the damage [97], [140]. Inflammatory response plays a key role in secondary TBI, it often disseminates within the first few hours and persists chronically to participate in neurodegeneration [38]. Inflammation is associated with fatigue, depression, anxiety, seizures, migraine, and suicidal tendencies apart from severe neurological conditions. However, inflammation is rather overlooked in context to secondary TBI [162]. Recent studies have shown that complete block down of inflammatory response right after injury has rather negative effect in the total outcome [38], [163], [164]. Minocycline treatment

in TBI mice showed reduced varicosities and suppressed microglial activation showed beneficial effects [165]–[167]. Conversely, another study showed that microglial processes are essential to close the BBB post disruption of barrier post TBI [168]. Most studies have shown cytokines like $\text{TNF}\alpha$, IL-1 have detrimental effects in TBI patients and suppression of these inflammatory molecules has shown improved results [39], [169], [170]. Hence, consistent research in this area is imperative to find the ideal time and level of restricting the inflammation with respect to the level of injury is ideal to arrest secondary injury and improve the prognosis of TBI patients.

The mitogen activated protein kinase- activated protein kinase II (MK2) of p38 mitogen activated protein kinase (MAPK) pathway plays a crucial role in neuronal inflammation [23], [171], [172]. Elevated activation and expression of this pathway has shown increased levels of $\text{TNF}\alpha$, IL-1, IL-6 that are correlated with development of several neurological diseases and pathogenesis post TBI [39], [171], [173]. IL-1 is also associated with sleep, feeding and memory in CNS pathologies and exerts neuroendocrine effects [139]. Studies conducted by Hallenbeck et al. have shown that $\text{TNF}\alpha$ has severe effects on brain with excessive production and direct administration of $\text{TNF}\alpha$ to brain has blocked the antibodies required for $\text{TNF}\alpha$ action reducing the injury [174]–[176]. Given the key role of IL-1 and $\text{TNF}\alpha$ targeting expression of these inflammatory can improve the outcome in TBI patients. Previous studies conducted in our lab have shown that KAFAK a cell penetrating anti-inflammatory peptide can inhibit the production of pro-inflammatory cytokines $\text{TNF}\alpha$, IL-1, IL-6 in vitro. A study conducted by shown that zhijiang et al, intrathecal delivery of KAFAK/BDNF modified

hyaluronan-methylcellulose (HAMC) hydrogels in rat spinal cord injury models reduced the expression of IL-1 and TNF α and shown neuronal protection [110].

In this study, for the first time we tested the ability of KAFAK to permeate the BBB and exercise its therapeutic potential to reduce the expression of pro-inflammatory cytokines in fluid percussion TBI mice models after intranasal administration. A comparative study to test therapeutic efficiency by using two different modes of administration has been conducted using intranasal and intraperitoneal administration. The localization of peptide KAFAK in the brain post IN administration was visualized using fluorescence microscopy. This study can be implicated to treat different neurological diseases associated with inflammation and the cell penetrating peptide sequence can be used as a vector molecule to carry different therapeutic moieties.

6.3 Materials and Methods

6.3.1 Materials

The peptide KAFAK-RITC and KAFAK-FITC were custom made and purchased from Biomatik, Canada. Anesthesia cocktail was made using ketamine hydrochloride (Vedco), 0.9% saline (Teknov(A), and xylazine (Vet One). Injury hub was installed using dental acrylic poly (methyl methacrylate) (Lang Dental) and capped with 2% agarose (VWR chemicals) post injury. Cardiac perfusions were performed using 4% formalin prepared from 37% formaldehyde (Ward's Science), monobasic sodium phosphate (MP Biomedicals), dibasic sodium phosphate (Sigm(A) and PBS (Gibco). Brains were saturated in 30% sucrose (sigm(A) and saturated brains were encased in low melting point agarose (IBI Scientific). For mounting the brain slices on to the slide antifade mounting media was formulated with glycerol (Himedi(A), Tris (VWR), and n-propyl

gallate (MP Biomedicals). Nuclear labelling using 4',6-Diamidino-2- 68 Phenylindole, Dilactate (DAPI, Roche Diagnostics). ELISA Kits IL-1, IL-6 and TNF α (mouse) were purchased from Boster and some acquired as part of aspire member program by thermofisher. Protein assay (Pierce Rapid gold BCA protein Assay kit, Thermoscientific) was used to determine the protein concentration in the mouse brain homogenates.

6.3.2 Animal Preparation and Handling

Animal handling, care and the experimental procedures were conducted owing to the guidelines and in conformity with Louisiana Tech University Institutional Animal Care and Use Committee-approved protocols. Wild type C57BL/6NHsd were purchased from Jackson Laboratory and bred according to the need. Animals were maintained under constant environment with 12 h dark/light cycle and cared for by providing food and water ad libitum. Randomly 4 female mice and four male mice between age groups 8-16 weeks and weight between 8-27 gms were chosen and assigned to each of the following groups. (1) Sham injury treatment with vehicle water, (2) TBI injury treatment with vehicle, (3) TBI injury treatment with KAFKAK 500 μ M. Treatments were given within the first hour after the injury. For ELISA tests randomly nine mice were selected for SHAM (no injury+ vehicle treatment), TBI (injury +vehicle treatment), and TBI (injury +500 μ M KAFKAK treatment). Another group of 18 mice were randomly added to the above groups post power analysis.

6.3.3 Surgeries for Mice

Mice were separated into individual cages, weighed, and sedated with 2% isoflurane in 500ml/min airflow using anesthesia chamber (Somnosuite digital vaporizer system (Kent Scientific Corporation, Torrington, CT, US(A))). Post sedation mice were

administered with 10% w/v of ketamine (10mg/kg)/xylazine (1mg/kg) in saline) intraperitoneally, with respect to their body weight. A 10% booster dose might be administered if necessary. Toe-pinching and eye gel (absence of blink response in anesthetized mice) were used to check the reflexes, mouse will be returned to caging to prevent the fight back response of the mice to anesthesia. The hair on the skull is carefully removed without cutting the whiskers and skin. The mouse will be placed on stereotactic frame with controlling temperature heating pad to prevent thermal shock. A nose cone apparatus that is fixed to the stereotactic frame nose bar helps in free airflow and low percent anesthesia upon need. The head is positioned using atraumatic ear bars and nose bar. The surgical area is sterilized by swabbing with betadine followed by 90% isopropyl alcohol. A microscope is used to visualize during surgery for proper positioning of the anchor, trephine and clearing the craniotomy. The mice are checked for reflexes and breathing regularly during the surgery to assess the depth of anesthesia and administered small dose of k/x if necessary.

A midline incision extending right behind the eyes to the neck was made on the skin using the surgical scalpel (blade 15). The connective tissue on the skull was carefully cleared and an anchor (~0.5-mm height, 1.7 mm-wide) made from disc of weed whacker line was glued between bregma and lambda corona sutures. The skull is carefully drilled using handheld 3mm trephine with minimal pressure until the skull looks transparent under the microscope in the drilled area. The utmost care is taken to prevent any kind of damage to the dura, pieces of skull around the craniotomy are removed and cleaned with saline and sterile cotton. If the dura is damaged or persistent bleeding occurs the mice were sacrificed and excluded from the study and replaced with another mouse.

A hub that is made from the female end of 20 G hypodermic Luer Lock needle is fixed using cyanoacrylate glue and Jet Denture dental acrylic/methyl methacrylate (Lang Dental) to expose the craniotomy for the injury. The hub was filled with saline and sealed with parafilm to prevent the dura from drying. The mouse was returned to temperature-controlled housing and monitored until recovery. Figure 6-1 and Figure 6-2 show the surgical setup for craniectomy procedures on mice.



Figure 6-1: Surgery table setup for performing craniectomy surgeries on mice.

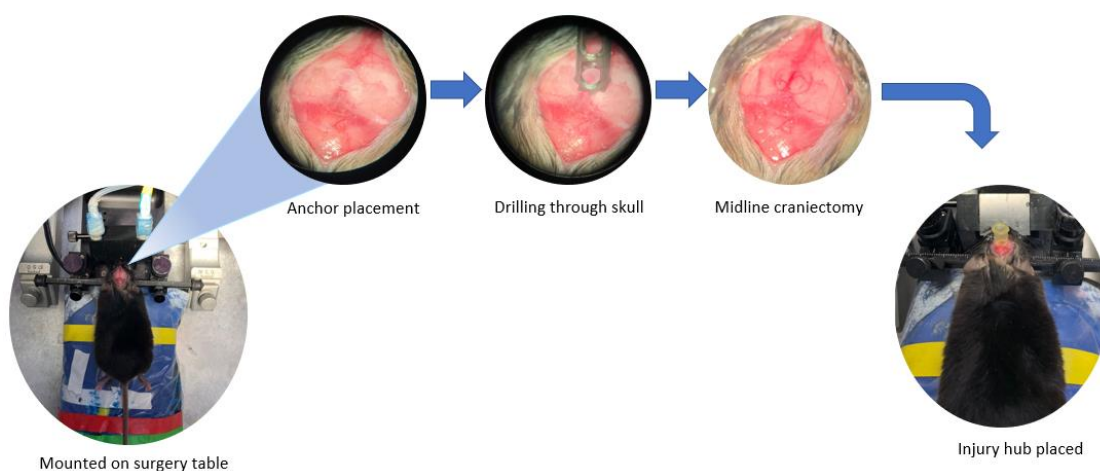


Figure 6-2: Image representing the setup of a mouse on a surgical table, the craniectomy using a trephine to expose the brain dura, and the placement of an injury hub to connect to a fluid percussion instrument for injury.

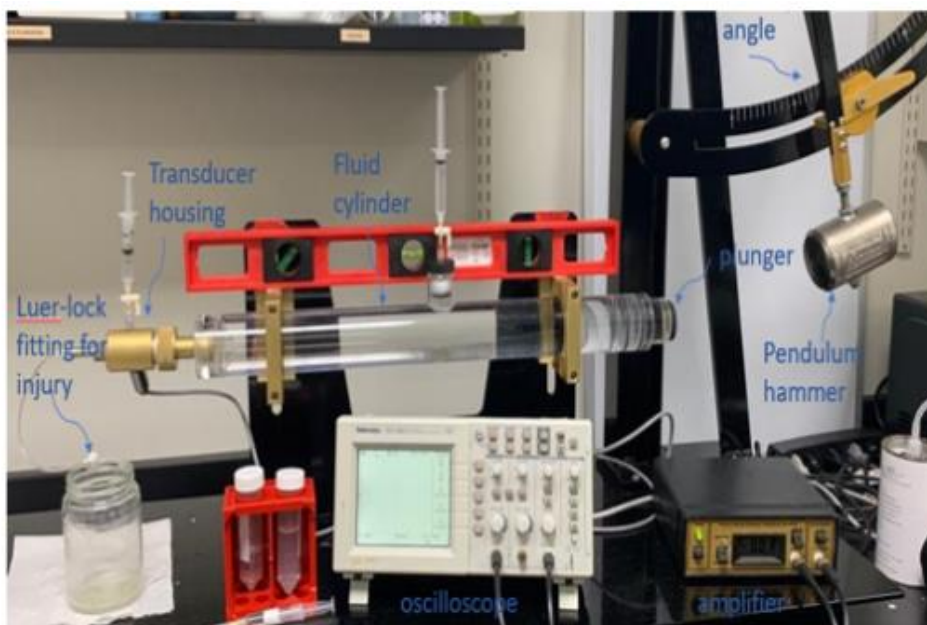
6.3.4 Midline Fluid Percussion Injury (mFPI)

Animals were randomly grouped to Sham, TBI injury with vehicle treatment, and TBI injury with therapeutic treatment and the mice would receive or not receive mFPI. The Sham group goes through all surgical procedures and receive sham injury (no fluid injury pulse will be delivered). Injuries to the mice were performed after 6 hours and not exceeding 12 hours after the surgery when they are fully mobile. The FPI device (Custom Design and Fabrication, Virginia Commonwealth University, V(A) is primed before the injury to ensure smooth signal on oscilloscope (Model TDS 1002, Tektronix), and consistent fluid pressure and checked for air bubbles in the chamber. Mice were sedated using 2% isoflurane in 500ml/min airflow using anesthesia chamber (Somnosuite digital vaporizer system (Kent Scientific Corporation, Torrington, CT, US(A)). The parafilm on the injury hub was removed and saline was filled in the hub if there were any leaks of saline after surgery. The male end of the FPI device is hooked to the female end of the injury and made sure it is hooked tightly. If the hub or hook comes off during the injury

the mice were excluded from the study. These obstructions during the injury result in dampened and inadequate injury. Once the setup is intact and the mice start to revive back to sense the hammer is dropped which is set at 17.5° angle delivering a single fluid injury pulse of ~20 ms. When the pendulum hammer after hitting piston is secured to prevent from delivering further pulses. The animal was removed from the device and brought back to the temperature-controlled housing in a supine position. The time taken for the mice to right back itself on four limbs is recorded as righting response (RR) time.

RR time is used as one of the guides to determine the severity of the injury, the other being neurological severity score (NSS). This study used moderately injury mice, RR time between 5-12 minutes is recorded as the moderate injury and anything lower than that is mild injury and excluded from the study. Mice that have RR time greater than 13 minutes but appeared healthy are included in the study and further assessed depending on the rotarod performance and NSS data. The oscilloscope traces give information about all the parameters of the injury which were recorded to calculate the injury pressure.

The mice were IN administered peptide (KAFKAK) or vehicle treatment with in the first 45 minutes of the injury by using nose cone for sedation (1% isoflurane). The injury hub was removed, cleaned, and inspected for hematomas and herniation. Mice that showed hematomas are euthanized and mice that received herniation were recorded and included in the study. The cranium is capped by using 2% agarose (in DI water) and sealed by dental acrylic to prevent infections to the brain. Figure 6-3 shows the FPI setup.



Fluid percussion injury instrument

Figure 6-3: Set up of Fluid Percussion Injury (FPI) injury system for achieving mild TBI in mice for the study.

The injury to the mice is achieved by dropping the pendulum hammer (set at an angle 17.5 for this study (shown in the image)) the creates and impact on piston, that induces fluid derived pulses through the implanted injury hub to the exposed dura. The force of the pulse generated each time is detected by the transducer at the end of the cylinder and the signal produced is amplified and sent to oscilloscope which can be visualized in mV. Conversion of voltage to pressure (atm) helps to determine the force of FPI delivered to each mouse for injury to the brain.

6.3.5 Administration of the Drug

The mice were treated with either water or 500 μM of KAFAK peptide depending on the group they belonged. Since the peptide is dissolved in water the mice were treated with water (vehicle) for control group. Initially the mouse was sedated using 2% isoflurane using anesthesia chamber, then it was moved to nose cone anesthesia with

reduced isoflurane (approx. 0.8-1%) and following the previously set protocols a total of 24 μ l of the peptide solution was administered through the nostrils using 10 μ l pipette tips. No more than 6 μ l were administered each time to prevent drowning and systemic leakage and 6 μ l volume is considered ideal to aid passage to the brain through olfactory epithelium [177]. The solution was slowly administered into alternating nares slowly with a gap of at least one minute between each dose, while the mouse was kept in reverse Trendelenburg position. After administering four doses the mouse was returned to cage and monitored until the mouse gained consciousness (Figure 6-4).



Intranasal (IN) administration



Intraperitoneal (IP) administration

Figure 6-4: (A) Intranasal administration of drug to the mouse (B) Intraperitoneal administration of drug to the mouse.

The dosages were determined based on the preliminary studies conducted to access the BBB permeability and localization of the peptide post intranasal administration. Fluorescently labelled peptide of different concentrations (300 μ M, 500 μ M and 1mM) was used for the preliminary study, the same concentration was used for ELISA's to test the therapeutic efficiency. The finalized concentration was administered for both the studies, for accessing biodistribution and access the drug effect

on behavior of the mice a 7-day study was conducted with 6-day treatments (including the day of injury), while to test the ability of KAFAK to reduce the pro-inflammatory cytokine production a single dose was administered.

A comparative study to test intraperitoneal route of administration was conducted by using mice that were randomly selected and given fluorescently labelled peptide drugs at 10% w/v of 500 μ M concentration. A single dose of drug was administered within 30 minutes post injury to test KAFAK for its anti-inflammatory effects.

6.3.6 Behavioral Test

A variety of neurobehavioral tests were conducted to assess the cognitive and acute sensorimotor deficits in the mice post traumatic brain injury. Behavioral tests provide an opportunity to access the therapeutic agent's pharmaceutical effects by monitoring functional improvements over time [43]. Rotarod, modified neurological severity score (mNSS), novel object recognition (NOR), open field (OF), and elevated plus maze (EPM) tests were performed following to the protocols. Mice were subjected to human interaction before addition to the study through rotarod training. A single operator was handling the mice throughout the study to minimize non-specific stress and operator related variabilities. All the tests were performed in the dark phase of the sleep cycle as they are active during this time (nocturnal animals). During performing this test an overhead wide-angle camera was used for recording for later analyzing the videos offline. All the animals were acclimated to the room conditions before testing. Table 6-1 presents a summary of the tests, procedures, and treatments used in the study.

Table 6-1: *Summary of Tests, Procedure, and Treatments for Each Mouse for the Biodistribution Study*

Day	Procedure/test	Treatment
-3, -2, -1	Rotarod training	N/A
0	Surgery, Injury (RR)	KAFAK (500 μ M) or vehicle (controls: TBI only and sham)
1	N/A	KAFAK (500 μ M) or vehicle (controls: TBI only and sham)
1	Rotarod, mNSS	KAFAK (500 μ M) or vehicle (controls: TBI only and sham)
3	N/A	KAFAK (500 μ M) or vehicle (controls: TBI only and sham)
4	N/A	KAFAK (500 μ M) or vehicle (controls: TBI only and sham)
5	Rotarod, mNSS	KAFAK (500 μ M) or vehicle (controls: TBI only and sham)
6	N/A	N/A
7	Rotarod, mNSS, OF, NOR, EPM, extraction of brain	saturated brain in formalin solution for 10 hours followed by 30% sucrose

6.3.7 Rotarod

Rotarod tests were performed to assess the locomotor function and learning of motor coordination in mice. This test is specifically sensitive to cerebellar dysfunctions and these tests in our lab were conducted using touchscreen rotarod (Panlab Model # 76-0770, Harvard Apparatus) [178]. This device has five separate lanes that have individual levers and timers to track the time mice stays on the rod. This system ensures that mice tested together would not interfere with other mice. As the mice land on the lever the timer is stopped, and the data can be recorded. The time the mice stays on the rod is inversely proportional to the severity of the injury [179]. Rotarod training was started three days prior to the surgery for three consecutive days, the operator and timings were kept consistent to avoid variabilities. Male and female mice were tested separately, and

the lanes were cleaned with soap solution and dried to ward off scent from previous testing.

The mice were acclimated to the room for at least 10 minutes and the surroundings were maintained to minimize external sounds that would interfere with the testing. The rotarod testing consisted of 3 steps: stationary phase for 30 seconds, constant rotational phase at 5 rpm for 15 seconds and the acceleration step where the speed accelerates at 0.2 rpm/s. All the above steps were repeated thrice with a resting period of 10 minutes between trial 2 and trial 3. During the resting period the mice were returned to the cages and for the remaining time they stay in their lanes. Stationary step helps the mice to condition to the device and balance on the rod. During this step if the mouse fell (which could happen depending on the severity of the injury) it is returned to the rod and wait until the mouse balance for at least 30 seconds. If the mice fail in this step the other steps will no longer be performed. Any time during the constant phase if the mice fell, they were returned and record the number of times they fell. The average of the two best trails were taken for each day the test was performed. The scores were normalized with the baseline score (score from the day before surgery (-1)) to minimize the variability. Figure 6-5 shows the configuration of the Rotarod device.



Figure 6-5: Configuration of the Rotarod device. During the test, the mice were separated into five lanes, as seen in the image, and their latency is automatically recorded using individual levers.

6.3.8 Modified Neurological Severity Score (mNSS)

The test is commonly performed to assess the motor (abnormal status, muscle status), sensory (visual, proprioceptive, and tactile), balance and reflex tests [43]. Mice were tested for mNSS on day 2, 5 and 7 for this study and scored on scale 0 to 8. One point was given to each task the mice failed to pass, that is score 8 reflects severe injury. The 8 tasks that were assessed in this test are: hindlimb flexion, startled response, seeking behavior, ability of mice to walk on elevated bars 3 cm, 2 cm and 1 cm width and 30 cm long (1 minute to cross from the center), ability to balance on 0.5cm wide circular rod and 0.5 cm square beam (at least for 30 seconds). Figure 6-6 illustrates the mNSS tests.

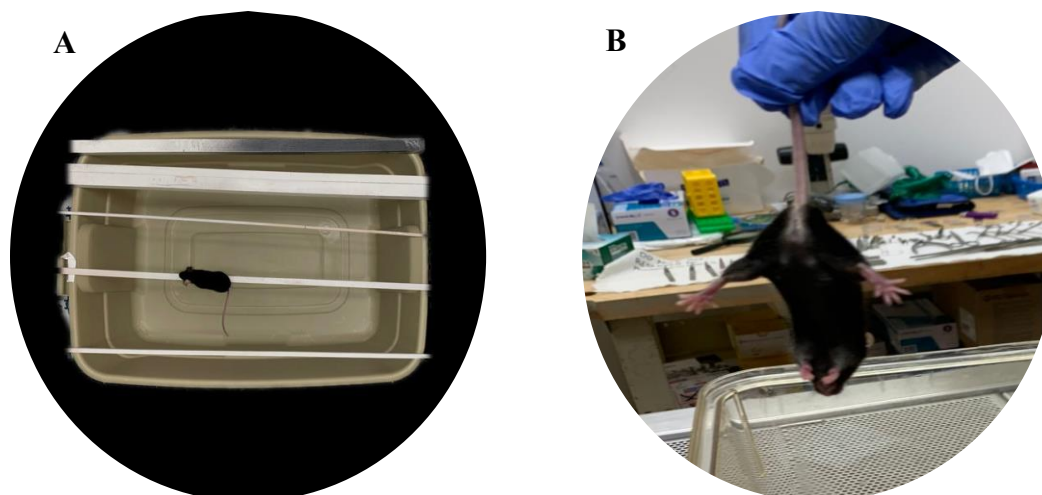


Figure 6-6: Illustrating mNSS tests: (A) represents different rods that were used for testing the mice (B) Hindlimb flexion of the mice.

6.3.9 Open Field (OF)

The purpose of the test was to evaluate the mice's exploratory behavior, anxiety levels, and overall locomotor skills. Due to social isolation, wide-open areas, and a novel environment, an open field causes anxiety in test animals [180]. This experiment was conducted in a 30 cm x 30 cm x 25 cm white wooden square box (see figure). The color white increases contrast while analyzing videos using the FIJI program. Prior to the test, mice were acclimatized to the room for 10 minutes. The mouse was then taken from its cage and placed in the center of the open field test box (Figure 6-7). A video was captured for 5 minutes as the mouse explored the box. The mouse was returned to its cage after the test. The cage was thoroughly cleaned to remove any odor from the mice that had been tested previously, and measures were taken to avoid external stimuli such as noise, bright light, temperature fluctuations, etc. Additionally, this step acts as acclimatization time for testing novel object recognition.



Figure 6-7: Mouse during the open field test as viewed through the camera for recording.

6.3.10 Novel Object Recognition (NOR)

The experiment was undertaken to test the mice's memory using their natural impulses to investigate unexpected objects [181]. This test is a low-stress test administered in the same box as OF after at least 5 minutes of acclimation. The mouse was placed in the center of the box with two identically sized objects in two adjacent corners, and its exploration of the objects for five minutes was recorded. The mouse will be returned to its cage, and one of the objects will be replaced with a new object of a different shape. The test is repeated with a new object and another 5 minutes of data are recorded. The position and selection of the fresh object were determined at random. The box was meticulously cleaned to remove any odor from previously tested mice, and precautions were taken to avoid external stimuli such as noise, strong lights, and temperature fluctuations, among others. The amount of time the mouse spent sniffing, climbing, or contacting the novel object was quantified (Figure 6-8).

Discrimination index (DI) = (time spent with new object multiplied by 100) / (time with identical object plus time with novel object).

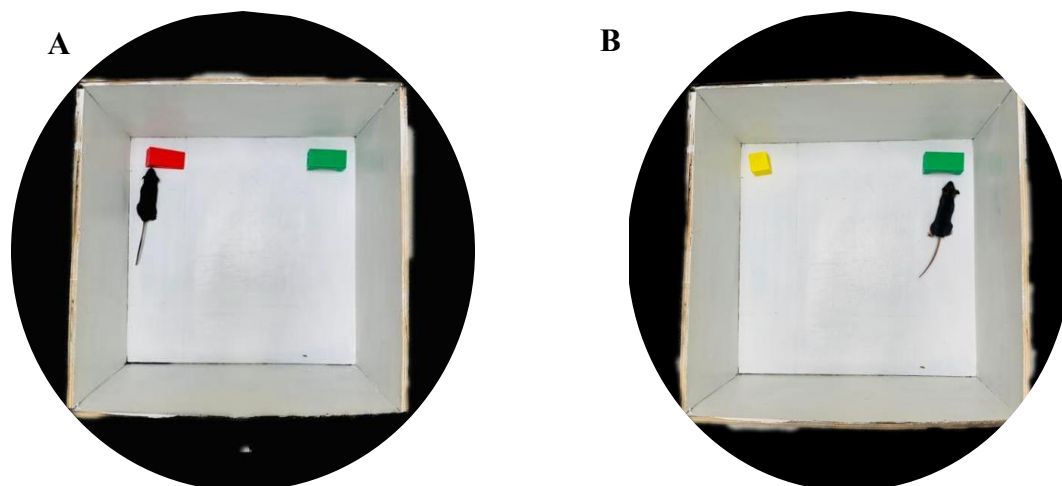


Figure 6-8: Mouse during the novel object recognition test as viewed through the camera for recording (A) NOR1 with two different objects (B) NOR2, one of the object replaced with the other.

6.3.11 Elevated Plus Maze (EPM)

The EPM test was carried out to assess the mice's behavior under anxious settings. The maze is 50 cm above the ground and features two open arms and two closed arms (25 cm high walls) at right angles to each other (see figure below). The test relies on the mice's natural tendency to avoid open spaces and stick to closed walls (thigmotaxic)[182]. The box was thoroughly cleaned to remove any scent from previously tested mice, and precautions were taken to avoid external stimuli such as noise, strong lights, and temperature fluctuations, among others. The mouse was positioned in the middle of the four arms, facing the open arm, and a five-minute video was recorded as it explored. The preference to enter the open or closed arms quantifies anxiety-like behavior. It is calculated as a proportion of entries, or the amount of time spent in the open arm. Figure 6-9 shows a mouse during the elevated plus maze test.

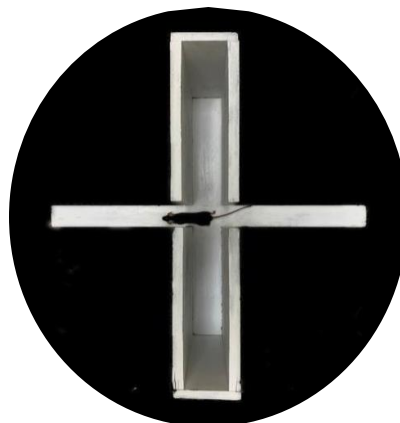


Figure 6.9: Mouse during the elevated plus maze test as viewed through the camera for recording.

6.3.12 Video Analysis

The videos obtained were converted to AVI files (Audio Video Interleave) at ten fps. The audio in the files were deleted and then uncompressed and converted to gray scale using the same software. The videos were trimmed to 300 seconds (5 minutes) and the last frame was edited to remove the mouse from the frame that was used as a background for the video. If needed the frames were cropped to square and removed the background noise to fit exactly to the OF box. After necessary edits the files were converted to multi-TIFF files that were read by plugins.

6.3.13 Extraction and Processing Brains

Post recordings on the day of the sac mice were anesthetized with 10% w/v of k/x administered intraperitoneally. Once the mice were fully anesthetized (conformed by hind toe pinching) the mice are taped on to the surgery table at forelimbs and tail in supine position. To expose the heart, a careful incision was made in the thoracic cavity. The aortic arch was nicked to allow the blood to drain, and the mice were perfused with approximately 25 ml of 1X ice cold PBS (to clear blood) followed by approximately 25

ml of 4% formalin (to fix brain) transcardially through the left ventricle via 27G needle attached to the peristaltic perfusion pump. Excess PBS was occasionally used when the liver showed red stains, and PBS was run until the liver turned pale and blood-free. The head was decapitated, and brain (including occipital lobes) was extracted from the skull using curved forceps and fixed in 4% formalin for 12 to 15 hours at 4°C. Later transferred into 30% sucrose solution at 4°C and saturated. Brains sink in the solution as they saturate, later brains were prepared for vibratome sectioning or cryo-frozen for preservation. Figure 6-10 illustrates the extraction of a mice brain.

Mice that were used for the ELISA study were sacked 12 hours after the injury. The mice were only perfused with PBS and not fixed. The brains were frozen immediately and preserved at -80 °C after extraction to prevent degradation of cytokines.

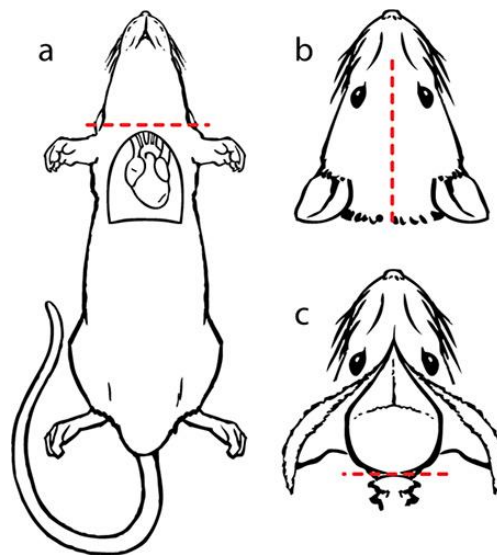


Figure 6-10: Illustrating the extraction of mice brain post perfusion from the mice[191].

6.3.14 Cryo-Preservation of Brains

To prevent degradation, brains were flash frozen using liquid nitrogen or 100% ethanol and dry ice. A slurry of dry ice and pure ethanol was made left for 5 minutes until

the mixture stops bubbling and fuming. In a small plastic container 100% anhydrous ethanol was taken let it acclimate in the slurry for a minute. Later brains were gently dapped with a clean and sterile paper towel to remove excess sucrose or PBS and dropped in the plastic container. After 30 seconds they are removed from the container into the labelled tubes and preserved at -80 °C for future use.

6.3.15 Sectioning of Brains for Visualization of Peptide

To visualize peptide uptake and distribution, brains were sectioned to a thickness of 60 µm using an oscillating tissue slicer vibratome EMS-5000 ((Electron Microscopy Sciences, Hatfield, P(A)) (Figure). Frozen brains were removed and placed outside for two minutes, whereas fresh, sucrose-saturated brains were used after surplus solution was dapped off. As illustrated in the figure, brains were cut at the brain stem to create a flat base and encased in 2% low-melting agarose PBS gel using a syringe. Low-melting point agarose minimizes tissue damage without the use of high heat. Encased brains were cooled in an ice bath and cyanoacrylate was used to adhere them to the cold mounting block. To create transverse slices of the entire brain, olfactory bulbs were positioned upwards. The block was attached to the buffer tray with screws before being inserted into the vibratome tray holder. The buffer tray was filled until the brain was submerged in ice-cold PBS, and the cold temperatures were maintained throughout sectioning. Using a soft bristle brush, brain slices were collected into a 48-well plate with PBS. To prevent loss of peptide fluorescence, slices are mounted promptly within 24 hours. Throughout the extraction, slicing, and mounting processes, care was taken to limit direct exposure to light. Unutilized samples are cryopreserved using cryo preservative solution (appendix for recipe). Figure 6-11 shows the apparatus used for slicing the brain tissue.

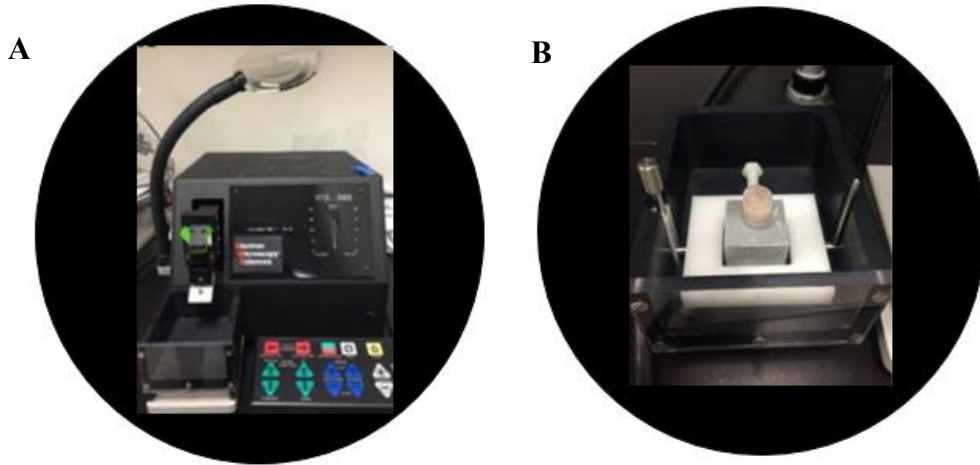


Figure 6-11: (A) Apparatus used for slicing the brains (B) brain glued onto mounting block in the ice cold buffer chamber.

6.3.16 Slide Preparation

The coronal tissue sections from various brain regions were carefully selected and separated into a small petri dish containing DAPI solution to stain the nucleus. The slices were incubated for ten minutes at 4 °C before being washed three times with PBS. After staining, the slices were saturated for 10 minutes in 30%, 50%, 70%, and 90% glycerol solutions at 4 °C. Optical clearing with glycerol minimizes background fluorescence.

The tissue sections were mounted to the slide with an adequate quantity of mounting media (anti- fade medi(A). The sections were assembled from rostral to caudal, including olfactory bulb and cortex sections. Precautions were taken to prevent section tearing. After the sections were lined up, a cover slip was gently placed on the slide. Once the slide was free of air bubbles and excess media, the ends of the cover slip were sealed with nail polish. Slides were stored in a slide box that was shielded from direct light exposure, and samples were imaged within 12 hours of preparation to ensure consistency.

6.3.17 Imaging of Samples

Using the Olympus IX51 and GFP, DAPI, and phase contrast filters, images of samples were captured. Throughout the imaging process, the settings, including light intensity and exposure, remained constant. Multiple regions of the sample were imaged with a GFP filter, followed by DAPI and phase contrast, to prevent the peptide fluorescence from being bleached by light exposure. Throughout the imaging process, care was taken to minimize fluorescence bleaching.

6.3.18 Cytokine Assay

6.3.18.1 *Homogenization of Brain Sample*

The brain samples were homogenized using a homogenizer (figure) with lysis buffer containing protease inhibitor cocktail and phosphatase inhibitor cocktail (recipes in appendix). 500 μ l of lysis buffer per half of the brain was added into the Eppendorf tube and grinded until a smooth suspension was formed. Grinding was done on ice with short pulses. Later the mixture was sonicated and left on shaker for 15 minutes at 4°C followed by centrifugation at 19,000rpm. The supernatant was collected and stored at -80°C. To avoid cytokine degradation, brains were preserved and worked in cold conditions from the time they were extracted from the mice.

6.3.18.2 *Protein Assay*

The protein concentration in the samples was quantified using Pierce Rapid gold BCA protein assay kit. The procedure uses the same copper chelating technology as the standard BCA assay. The samples dilutions and working reagents were prepared following the kit instructions. After determining the required amount of the reagent 50 parts of Rapid gold BCA reagent A was mixed with 1 part of Rapid gold BCA reagent B.

Into a 96 well plate 20 μ l of standard or sample were pipetted along with 200 μ l of working reagent. The plate was incubated for 5 minutes on a shaker and absorbance values were recorded at 480nm using plate reader from Dr. Paul Kim lab from Grambling university. A graph was plotted from the obtained values from which unknown concentration of the protein sample was determined. Based on the protein concentration of the sample, dilutions of the brain extract were estimated in accordance with the Boster ELISA kits.

6.3.18.3 *Enzyme-linked Immunosorbent Assay (ELISA) Test*

The protein concentrations of the samples were high so made up to 50-fold dilutions using lysis buffer such that the concentrations are within the range of the standard concentrations (in picograms) of the kit. Initially one sample was taken, and a series of dilutions were made to test and standardize the tests. Based on the protein concentration of each sample, dilution factors were determined for each sample. The samples were aliquoted into 3 Eppendorf tubes for three tests IL-1, IL-6 and TNF- α . The working reagents were prepared for each ELISA kits and the tests were performed in Dr. Paul Kim lab, Grambling University; according to the procedures mentioned on the Boster ELISA kits (sponsored by Dr. Paul Kim) and Thermo Fisher Invitrogen ELISA kits acquired as part of the Aspire program.

6.3.19 Statistical Analysis

Statistical analysis was conducted using pair wise comparison T tests by using normalized means. MATSAP in the MATLAB software was used for analyzing the behavioral data for EPM, NOR and OF.

6.4 Results

6.4.1 Preliminary Uptake Studies

To determine the peptide dose concentration that is required to obtain strong fluorescent signal after intranasal administration and visualize the biodistribution of the peptide in the brain preliminary tests were conducted using different concentrations of FI-KAFK at different time point. The mouse was treated with 24 μ l of 500 μ M concentration of FI-KAFK intranasally and after 4 hours the mouse was sacrificed. The brains were processed for slicing and counter stained with DAPI and imaged using Olympus fluorescence microscope. Images are presented in Figure 6-12.

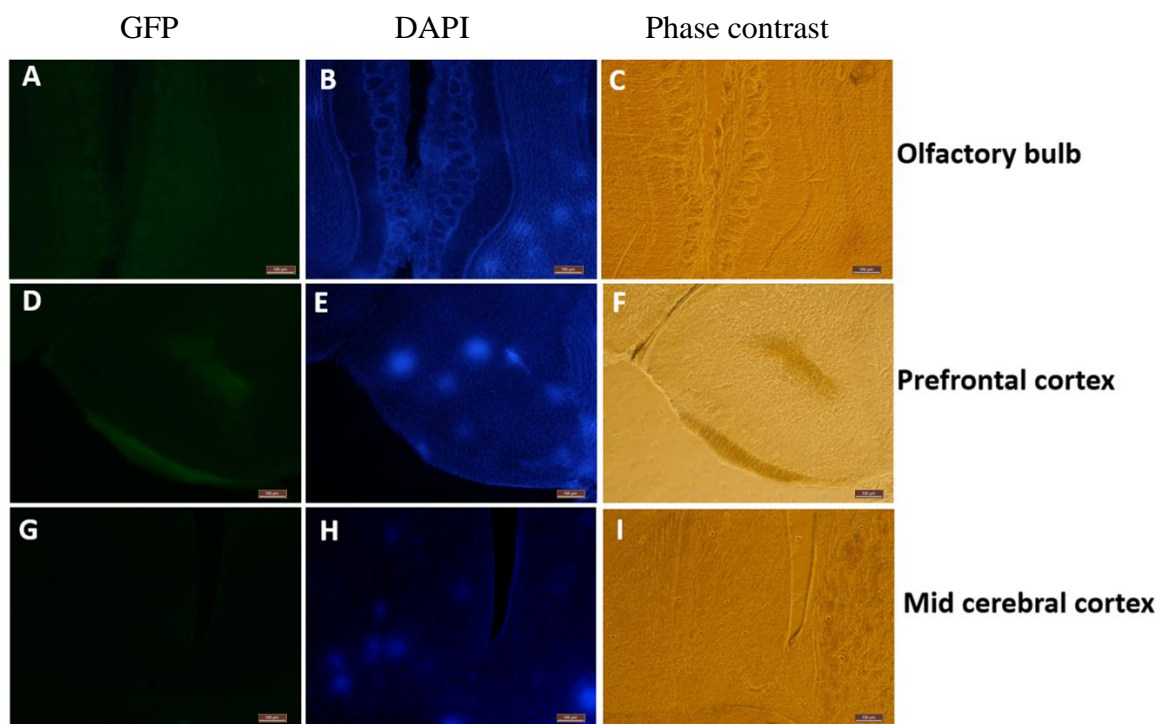


Figure 6-12: Fluorescent pictures of brain slices taken with GFP and DAPI filters after 4 hours of treatment with 500 μ M of FI-KAFK. A, B, and C are images of the olfactory bulb captured with different filters from the same location as D, E, and F from the prefrontal cortex and G, H, and I from the mid-cerebral cortex. The first column (A, D, G) shows brain slice images with the GFP filter, the second column (B, E, H) with DAPI after DAPI counterstaining the tissues, and the third column (C, F, I) with phase contrast images. The scale bar measures 100 μ m.

The olfactory bulb of mice that have been treated exhibited excellent punctate staining. In the subarachnoid spaces and ventricular portions of the prefrontal cortex, there is a modest fluorescence. Indicates that the peptide may have entered and proceeded through these regions. However, no fluorescence was detected in the cortical back areas. We speculated that this was owing to the fact that a small amount of the peptide dosages employed may have caused little peptide to reach the back, hence restricting the ability to visualize peptides via fluorescence. Due to the length of time necessary to prepare the brain slices, the minute levels of green fluorescein in the posterior parts of the brain could have been bleached (Figure 6-13).

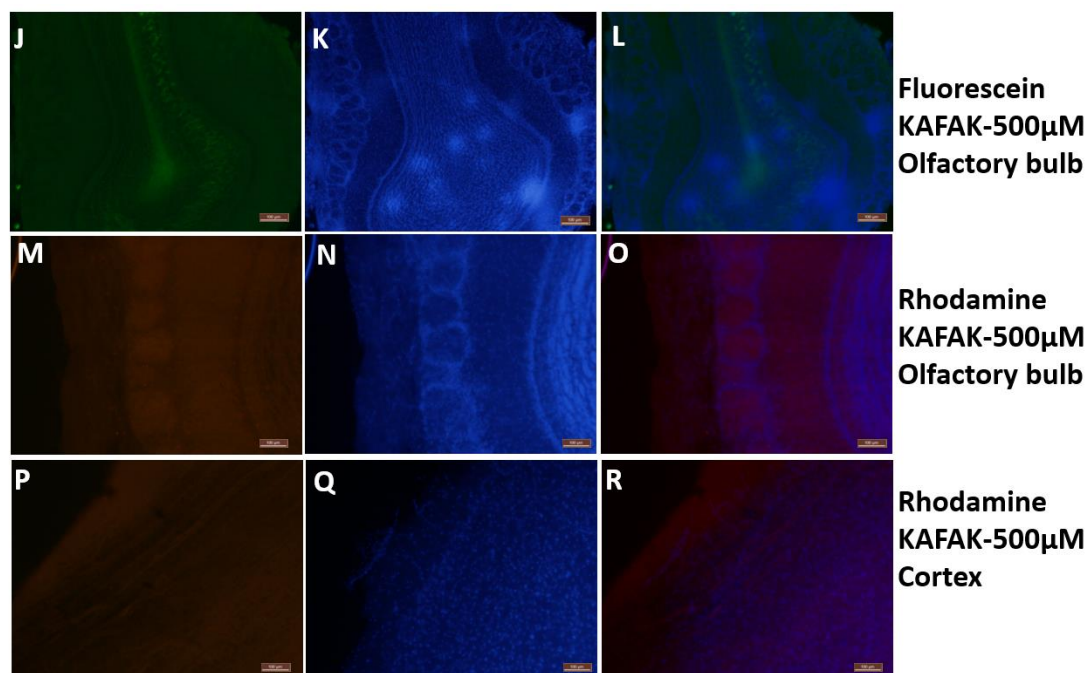


Figure 6-13: After 4 hours of treatment with 500 μM of FI-KAFK or Rh-KAFK, fluorescent images of brain slices captured using GFP, TRITC, and DAPI filters. Images J-O depict the olfactory bulb, while images P, Q, and R depict the cerebral cortex. The pictures in the second column (K, N, Q) were obtained using the DAPI filter, whereas the images in the third column (L, O, R) were merged DAPI with GFP or TRITC images. J, K, and L pictures were taken from the same location but with different filters, similarly (M, N, O) and (P, Q, R). Scale bar for the first row J, K, and L is 31.5 μm , whereas M-R is 100 μm .

To overcome the bleaching concerns, same concentrations of Rh-KAFAK were administered intranasally. Images demonstrated that Rh-KAFAK has spread throughout the brain. Nevertheless, we noticed that the intensity of fluorescence was significantly greater in the anterior areas of the brain, particularly in the olfactory regions, than in the posterior regions. This shows that KAFAK diffuses throughout the parenchyma in addition to the subarachnoid spaces.

6.4.2 Rotarod

Rotarod test helps in identifying sensory motor cognition deficits in mice. It is expected that the TBI causes the mice to lose cognition resulting in reduced time of latency. Statistical analysis was performed using T-test comparison between sham, TBI and treated mice. On day 2 Sham and TBI were treading differently however, KAFAK is also trending significantly different from TBI. This shows that there's a trend towards the kafak treated mice doing better than the tbi group but not as good as the sham group by day 2. This just means that there's a chance kafak starts having an effect as early as 2 days but not strongly enough to be properly measured. The Rotarod scores are presented in Figure 6-14.

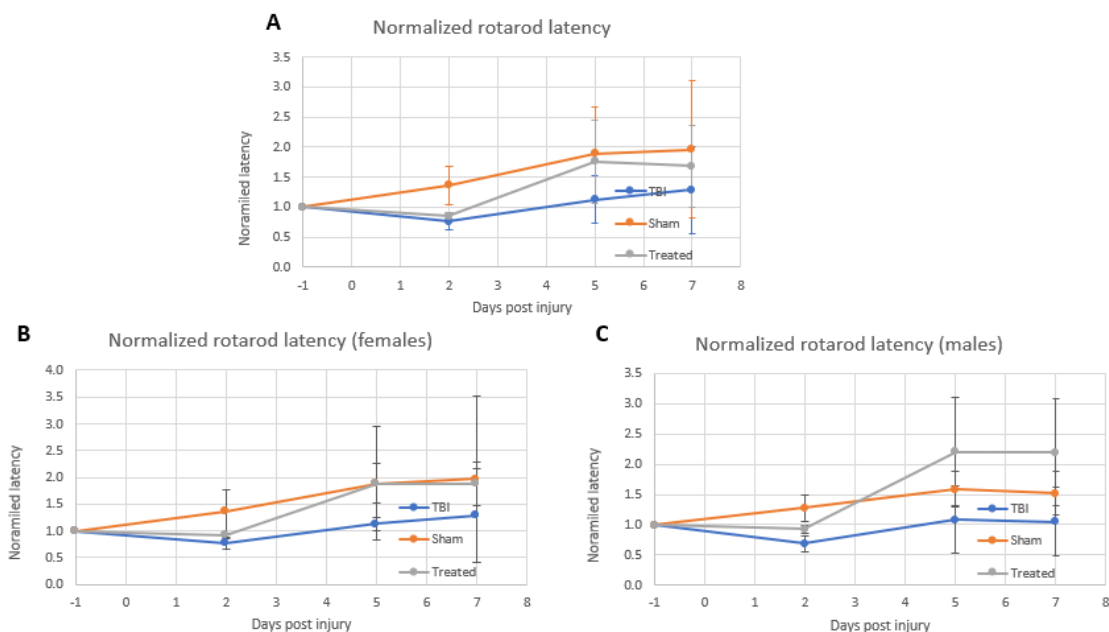


Figure 6-14: Normalised rotarod scores on day 2, 5 and 7. A represents the normalised rotarod data for all the Female mice added to each group, while B is the data of the male mice in the study and C represents the data of all the mice added to the study. Three groups sham (vehicle treatment), TBI, treated (500 μ M KAFK) (n=8 for each group) are added to the study.

From days 5 to 7, Sham and kafak strongly trend toward being statistically identical. While Kafak and TBI are becoming increasingly divergent. This demonstrates that Kafak treatment has positive effect on the mice. Although there is a considerable tendency for "kafak and sham" to be largely identical. The "tbi" group is trending toward becoming statistically similar to "the kafak and sham" groups. Thus, although it can be concluded that there is a strong trend in favor of kafak having a good influence on TBI's, additional research will be required to reach definitive results. In all treatment groups, there was no significant difference between male and female mice, except that treated males outperformed control males.

6.4.3 Modified Neurological Severity Score

The mNSS was used to evaluate the neurological deficits of mice, the higher scores indicate increased degree of neuronal damage (every failed test increases the mNSS score). Statistical analysis was conducted using pair wise T-test comparison between the groups (Figure 6-15).

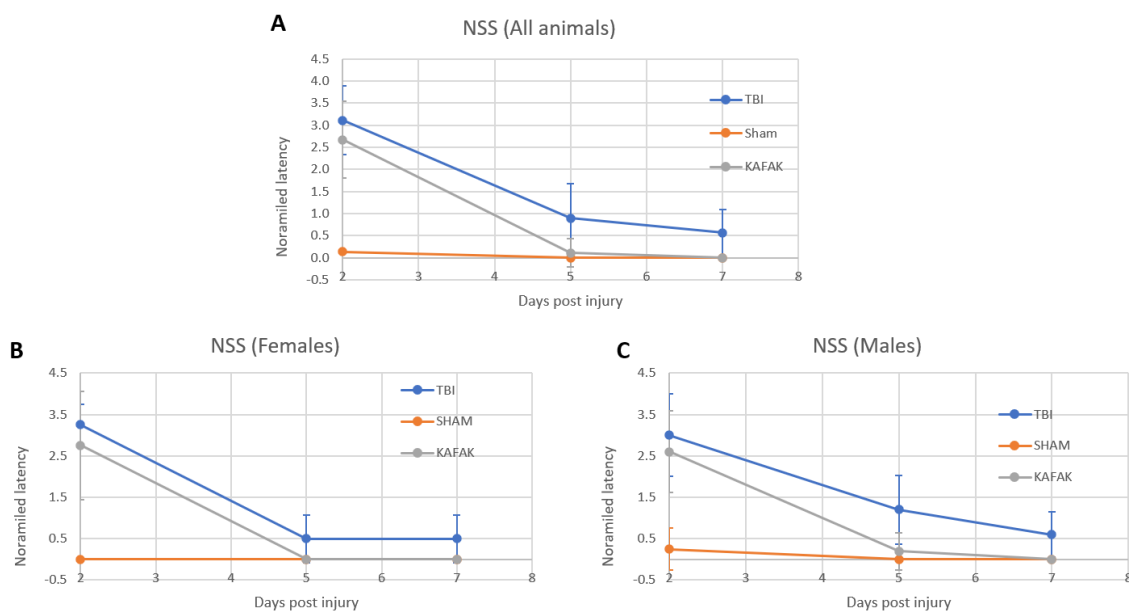


Figure 6-15: Normalised mNSS on day 2, 5 and 7. A represents the normalised mNSS for all the Female mice added to each group, while B is the data of the male mice in the study and C represents the data of all the mice added to the study. Three groups sham (vehicle treatment), TBI, treated (500 μ M KAFK) (n=8 for each group) are added to the study.

From day 2 to day 7, the trends for "sham and tbi" and "sham and Kafak" diverge significantly. It is anticipated that on day 2, there would be little difference between the TBI mice and the treated mice, as it would require some time for the drug to have its effects. On day five and beyond, Sham and Kafak trend toward being statistically identical. While Kafak and TBI are going towards significantly different, indicating KAFK has a beneficial impact on the mice's ability to do the NSS test.

6.4.4 Weights of Mice

The weights of mice in the control and treatment groups progressed similarly, whereas the weights of animals in the TBI group declined.

6.4.5 Elevated Plus Maze

This analysis was undertaken to determine the mice's anxiety levels. This can be determined by comparing the total distance traveled by mice on open versus closed arms. We expected that, compared to the TBI (vehicle) treated group, mice treated with our peptide would remain on the open arms for a length of time comparable to that of the control group. As anticipated, peptide treatment has raised the percentage of open arm stay duration, demonstrating a favorable effect of the KAFAK peptide following injury. The total distance traveled by each group was not significantly different; however, on an average the kafak group mice traveled less than the other groups even though not significantly different from other groups. Figure 6-16 and Figure 6-17 display the mean of the total distance traveled by mice in each group.

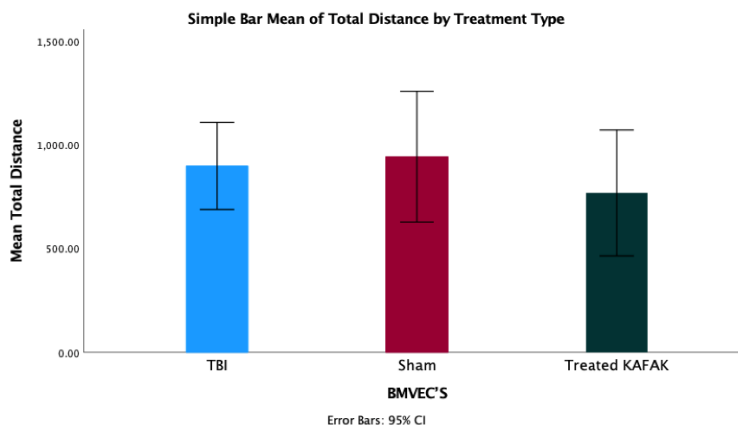


Figure 6-16: Mean of total distance traveled by mice in each group during EPM test (n=8).

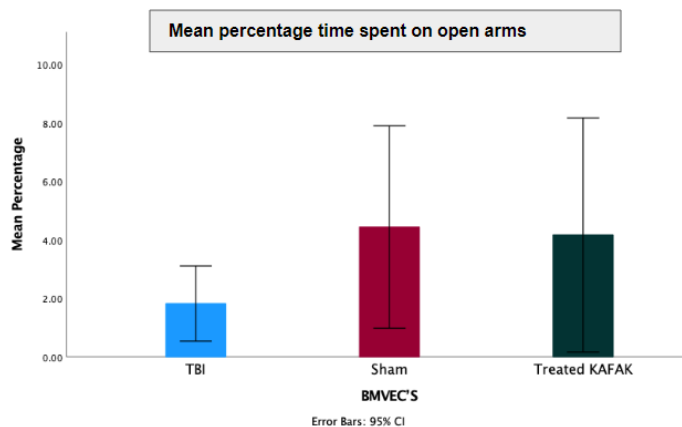


Figure 6-17: Mean of percentage time spent on open arm by each treatment group during EPM test (n=8). (* = $P < 0.05$)

6.4.6 Novel Object Recognition

This experiment was conducted based on the mice's natural propensity to investigate unfamiliar objects. It aids in memory testing and is conducted under stress-free conditions. The data suggests that the KAFK-treated mice are significantly better at identifying novel objects than the group of injured mice treated with vehicle. The graphs in Figure 6-18, Figure 6-19, Figure 6-20, and Figure 6-21 are represented as discrimination index (DI) (refer methods section).

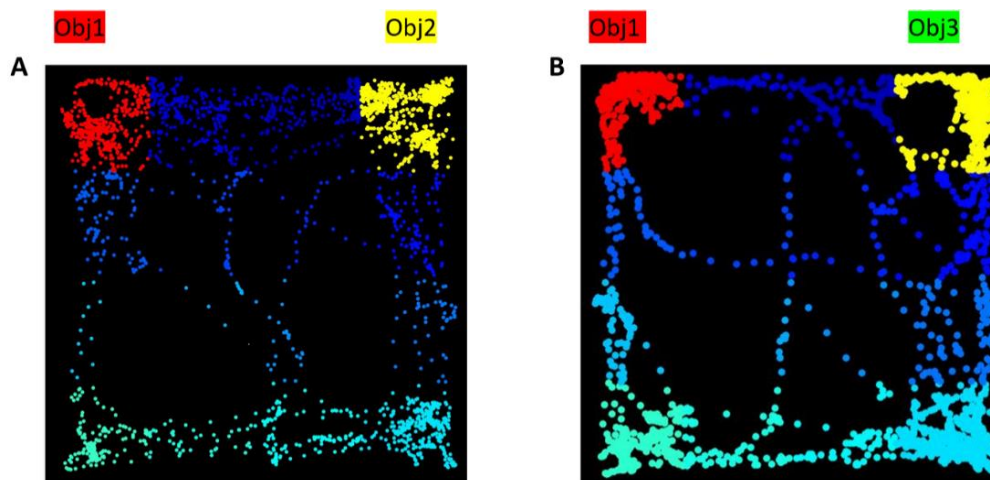


Figure 6-18: Traces of mice during the novel object recognition test. Red color represents the familiar object (not changed). Yellow color represents the novel object (changed between the tests)

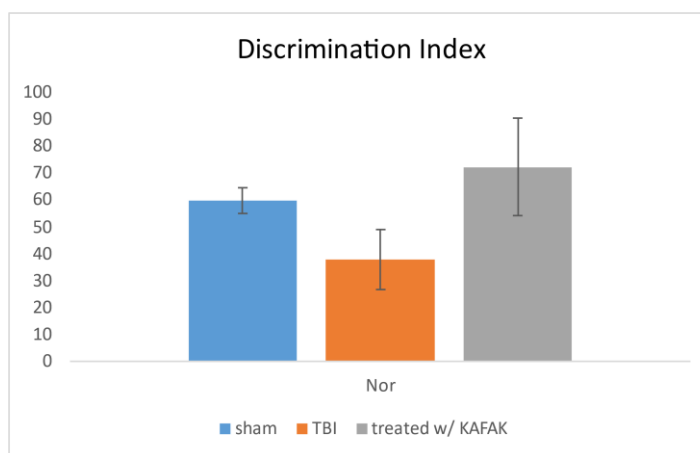
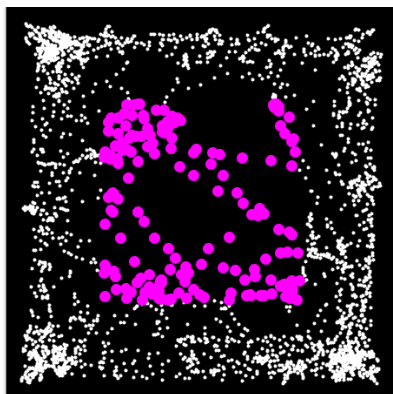


Figure 6-19: Novel object recognition test results on day 7 between sham, TBI and TBI treated with KAFK peptide. The data (n=8) is represented as mean of discrimination index with ± 2 standard error. (* =P< 0.05)

Open field

A



B

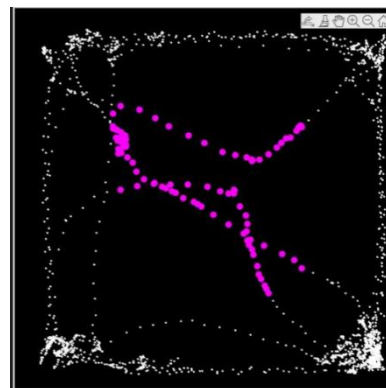


Figure 6-20: Open field mouse traces. The pink dots represent the open field's center (region of interest). White dots depict the edges of the open field wall. (A) trace of a mouse that is moderately stressed (eccentric value = 0.91 (in the most of frames) and speed (about 37.6% SAP. (B) Trace of mice that are severely stressed and remained primarily in the corners and along the walls

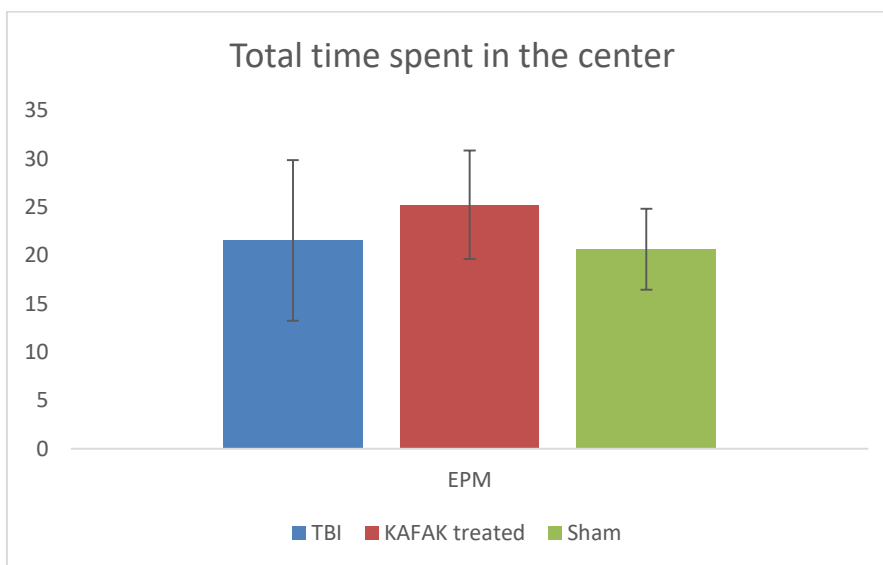


Figure 6-21: Open field test results on day 7 between sham, TBI and TBI treated with KAFAK peptide. The data (n=8) is represented as mean of discrimination index with ± 2 standard error. The data is not significantly different.

The mouse's anxiety levels in open spaces were tested using an open field. Injured mice prefer to stay near the walls and avoid exploring the center. MATLAB rodent tracker was used to calculate the percentage of time the mouse spent in the center and the

stretched attend posture (SAP). The eccentric values greater than 90% and a speed less than 8 indicates that the mice were stressed.

6.4.7 Cytokine Assay

Using Boster and Thermo fisher ELISA kits, the therapeutic efficacy of KAFK peptide to inhibit cytokine production caused by mFPI injury is evaluated. This study investigated three cytokines: IL-1 β , IL-6, and TNF α that are known to participate in the development of secondary injury. The mice were separated into four groups: sham (no injury), TBI (injured mice treated with vehicle), TBI-KAFK-IN (injured mice treated with 24 μ l of 500 μ M KAFK intranasally), and TBI-KAFK-IP (injured mice treated with 10% w/v of 500 μ M KAFK intraperitoneally). In this study, mice with moderate injuries (RR time between 6 and 12 minutes) were used. Initially, three mice were added at random to each group; following a power analysis (required 4 mice to be added), five additional mice were added to each group.

6.4.8 Power Analysis

Using the data collected between four groups, a power analysis was conducted to test the significance of the study and determine the sample size required to achieve the desired significance levels. The mean of samples in each group were calculated and power analysis was performed (Figure 6-22).

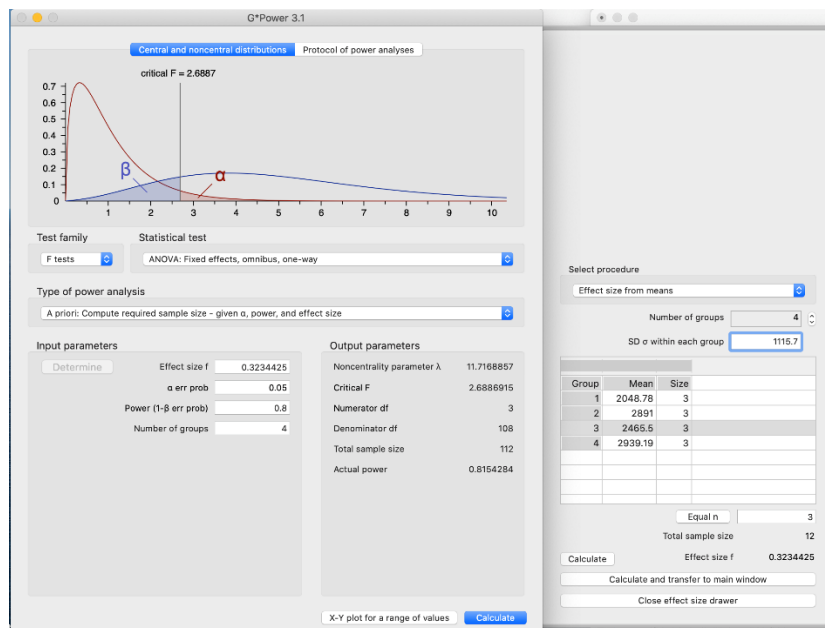


Figure 6-22: G*Power window showing the number of samples requires to achieve desired significance for the study.

6.4.9 ELISA

ELISA was performed using the supernatant of brain homogenate samples collected after 12 hours. The data demonstrates that mice treated with peptides produce less cytokines than mice not treated with peptides. For all three cytokines, intranasal administration of peptide produced more significant differences compared to the untreated control group. The intraperitoneal administration of peptide moderately decreases the levels of all three cytokines. It would have been optimal to increase the doses or concentration of the peptide administered intraperitoneally. Figure 6-23 shows the mean of the ELISA testing.

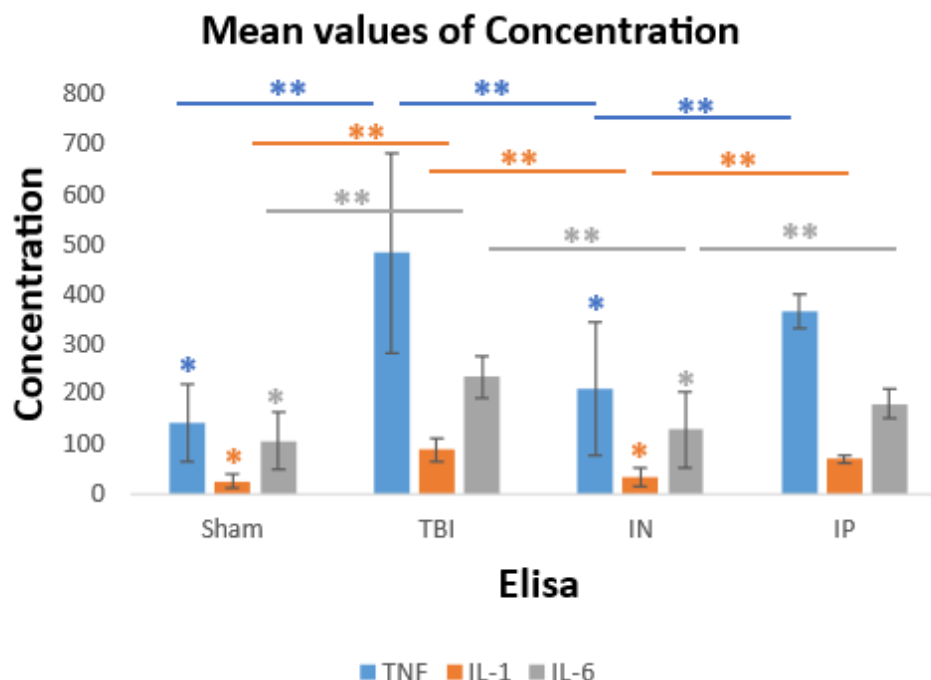


Figure 6-23: ELISA was used to quantify brain homogenate samples 12 hours after treatment (24 ul of 500uM concentration-IN and 10% w/v of 500uM concentration-IP). The treated groups differed significantly from the control untreated group (n=5). Standard error (* = $P > 0.05$; ** = $P < 0.05$).

6.5 Discussion

The anti-inflammatory effects of KAFK have been demonstrated in scientific literature and validated using hepatocytes in our laboratory. Cellular studies using primary BMVECs have suggested that KAFK can permeate the BBB (chapter 5). Therefore, the study was expanded to include in vivo studies using wild-type C57BL/6NHsd TBI mice as models. Different doses and administration routes were explored to determine the optimal method for achieving maximum permeability and therapeutic efficacy at low doses. As predicted, fluorescent microscopy images demonstrated that the peptide diffused throughout the brain with maximum intensity in the olfactory bulb after crossing the BBB. However, when the same drug concentration

was administered intraperitoneally based on body weight, no peptide-related fluorescent intensity was observed in the brain.

Using 500 μ M concentration of peptide intranasally (24 μ l) and intraperitoneally (10% w/v body weight), the therapeutic efficacy of the peptide to inhibit production of proinflammatory cytokines TNF α , IL-1 β , and IL-6 in TBI models was evaluated. These cytokines are upregulated following a TBI and are associated with secondary injury development [23], [39], [57], [184], [185]. In rat models of spinal cord injury, KFAK peptides inhibited these cytokines when implanted locally using hydrogels [110]. This is the first study to demonstrate that the KFAK peptide can traverse the BBB and exert its efficacy. We found that both intranasal and intraperitoneal administration reduced the production of all three cytokines in injured mice compared to those that received no therapeutic treatment. However, administration of peptides intranasally to mice reduced cytokine levels almost to those of control mice. Referring to uptake studies, the concentration of the peptide in the brain when administered intraperitoneally was insufficient to visualize fluorescence. Increasing the intraperitoneal concentration or dosage could increase therapeutic effectiveness. Behavioral analysis data have also evidenced the beneficial effects of KFAK on injured mice compared to injured mice that did not receive therapeutic treatment. Additional tests and research can be conducted to examine the activation of astroglia and microglia *in vivo*, as well as the half-life and toxicity of the peptide. This study can be inferred to other CNS diseases that are primarily caused by inflammation of the brain tissues, and it can be used as a peptide carrier for a variety of other medications.

CHAPTER 7

DIAZEPAM LOADED CLAY NANOTUBES PERMEATE THE BRAIN THROUGH INTRANASAL ADMINISTRATION AND SHOWS NO BEHAVIORAL CHANGES IN MICE

7.1 Abstract

The blood brain barrier (BBB) continues to be a major barrier to the permeation of therapeutics into the brain, limiting the availability of viable compounds for treatment of neurological deficits. There is a dearth need for addressing this challenge with new candidates that could potentially carry the vital molecules to the brain. HNTs are multilayer biodegradable clay nanotubes that demonstrated substantial potential in transporting a variety of drug molecules to diverse regions both in vitro and in vivo. However, these phenomenal candidates are not researched enough to test their ability to circumvent the brain and studied for the behavioral changes associated with accumulation of these components inside the brain. This study showed that HNTs can easily permeate the brain when administered intranasally for five days and accumulation of these molecules has not resulted in significant behavioral changes in the mice.

7.2 Introduction

The administration of medications to the brain is still hindered by the physio-chemical features of the BBB, which either entirely prevent permeability of certain drugs,

modify the therapeutic efficacy of the drug, or allow just sub-therapeutic doses [194], altering drugs at BBB). Although the BBB presents a hurdle for the transport of therapeutic molecules, it is of equal importance to preserve the barrier's integrity, since it plays a crucial function in maintaining homeostasis and protecting the brain from toxic substances and infections [194]–[196]. The emergence of new technology has facilitated the creation of new medication delivery systems and the enhancement of current approaches. With the expanding number of CNS diseases, however, there is still opportunity for the creation of new strategic carriers that could successfully transport therapeutic compounds to the brain. According to global figures from 2021, the prevalence of brain problems has surpassed cardiovascular diseases and cancers [195]. In addition to pathological conditions such as epilepsy, TBI, Alzheimer's, and Parkinson's, among others, increased substance abuse disorders, environmental pollutants (lead, asbestos, etc.), and COVID-related mental conditions all contribute to the rise in CNS problems that must be effectively addressed. Explosive development of nanoparticles such as HNTs as carriers has revealed exciting potential for the investigation of brain penetrating capabilities and drug delivery to the brain.

The therapeutic outcome of the medication is dependent on the route of administration. It is optimal to choose the administration of a medicine based on its physiochemical features and interactions [126]. Choice of route also depends on the amount of drug to be supplied, its solubility, pH, and the place of administration [132]. In addition, head posture, surgical interventions, distribution mechanism, delivery methods and volume affect the deposition of the drug in the nasal passages [133]. To transfer the medicine to the brain, intranasal administration has numerous advantages that overcome

the majority of disadvantages associated with parental, oral, transmucosal, and direct injections. IN administration is a noninvasive route that absorbs medicine from the nasal cavity via the trigeminal and olfactory pathways and delivers it straight to the brain parenchyma [121]. IN has numerous advantages, including self-administration and ease of administration, noninvasiveness, BBB-passage, and quick onset effect. However, some of the medications may induce nasal discomfort, and poor availability of large-molecule drugs [129]. Recent research has demonstrated that tiny peptide medicines and nano molecules are readily absorbed via nasal delivery.

Utilizing clay tubules is effective for cell membranes penetration due to the small cross-section they possess. In this case, halloysite penetrability is defined by their ten's nanometer diameter rather than a micrometer length. These nanotubes are formed by 10–15 revolutions of 0.72 nm thick aluminosilicate sheets and have diameters ranging between 40 and 60 nm, lumen diameters of 12–15 nm, and lengths within 500–900 nm [197], [198]. This nanomaterial is cheap and available in large quantities. The halloysites outer surface is composed of SiO₂, and the tube's interior is composed of Al₂O₃, which are oppositely (negative/positive) charged in the pH range of 3–9. The structure of halloysite is an advantage when loading materials or drugs such as neurotransmitters. This is due to the structural advantage and the ability to manipulate the electrochemical charges of the tube. Based on geometrical sizes of halloysite, one may conclude the maximal volume load inside the tubes of 10–12 vol.%, which may reach 15–20 wt.% with an external dug adsorption [199]. Increased drug loading means that molecules are adsorbed on the tube external surface, which may change the structural properties that are observed through zeta-potential and colloidal stability. Thus, inner adsorption of negative

molecules usually increases the electrical potential magnitude from ca. -30 mV in pristine to minus 45 – 50 mV in loaded nanotubes [200]. Drugs such as oxytetracycline, gentamicin, ciprofloxacin, vancomycin, atorvastatin, metronidazole, dexamethasone, doxorubicin, furosemide, nifedipine, curcumin, resveratrol, povidone iodine, amoxicillin, brilliant green, chlorhexidine, and DNA and viral genes were successfully loaded in halloysite [199].

Halloysite is a biocompatible material with low toxicity assessments [88], [201]–[207]. Researchers reached a consensus that these clay nanotubes are safe up to 0.5 mg/mL formation, which is less toxic than a common table salt [201]. This was tested on *in vitro* and *in vivo* systems: cell lines, micro worms, infusoria, fishes, mice, and rats [199]. An MTT assay was performed on endothelial cells lines as well to assess their cellular metabolic rate after the addition of halloysite and it did not affect it negatively at all up to 50 μ g/mL [86]. The only minor toxic effect was found with high oral halloysite consumption when acidic clay decomposes in the stomach increased Al^{3+} accumulation [204]. The mice that were orally fed with low nano clay doses (5 mg/kg mice weight, which corresponds to 3 mg of halloysite daily consumption for adult human for 1 month) have shown no oxidative stress or other toxicity signs, and even demonstrated higher growth rates.

In this study, we administered two different sized HNTs intranasally to C57BL/6NHsd wild-type mice for five days and evaluated their behavioral changes using a variety of behavioral analysis techniques, including the rotarod, neurological severity score, elevated plus maze, novel object recognition, and open field tests. The tests of HNT-treated mice were compared with those of SHAM mice to determine whether there

were any differences. All these assessments aid in identifying any stress, anxiety, memory deficits, sensory-motor cognition abnormalities, or other behavioral abnormalities that may result from the delivery of HNTs. After 4hrs, 12hrs, 24hrs, 48 hrs, 3 days, and 7 days of treatment with Rhodamine-loaded HNTs, the brains of mice were removed and examined under a fluorescent microscope to assess the brain permeation capabilities. In addition, to test the drug-carrying capabilities of HNTs to the brain, diazepam-loaded HNTs were administered to mice for six days as a control to evaluate the behavioral changes following treatment.

7.3 Materials and Methods

7.3.1 Materials

Halloysite was purchased from Sigma-Aldrich and used without further purification. Rhodamine B isothiocyanate was also obtained from Sigma-Aldrich. Ionomycin was purchased from Sigma-Aldrich. For the system analysis, scanning and transmission electron microscopes were used (EDAX-SEM, Hitachi-S4800, Japan and TEM, JEM-2100, JEOL, Japan) as well as thermogravimetric analysis (TGA, Thermal Advantage Q50, US(A), UV-vis spectrophotometer Agilent 8453, USA, fluorescent and laser confocal optical microscopy (Leica DMI 6000 B inverted microscope, USA and Nikon A1R Confocal and Super Resolution System, US(A). ZetaPlus Instrument (Brookhaven Instr, US(A) was used to determine the systems surface charge.

Ketamine hydrochloride (Vedco), 0.9% saline (Teknov(A) and xylazine (Vetone) were used to prepare 10% k/x solution. Chemicals and solutions used are PBS (Gibco), 4% formalin (Sigma Aldrich), 37% formaldehyde (Ward's science) monobasic sodium phosphate (MP biomedical), dibasic sodium phosphate (Sigm(A), DAPI (4',6-

Diamidino-2-68 Phenylindole, Dilactate (Roche Diagnostics)), Glycerol (Himedia(A), n-propyl gallate (MP Biomedicals).

7.3.2 Preparation of HNTs

After size and purity analysis of the nanotubes were concluded, the Halloysite samples were prepared by loading rhodamine B isothiocyanate (RITC) through stirring, centrifugation, and sonication at various ratios including 10 mg halloysite/1 mL DI water per 0.5, 1, and 2 mg of RITC. The solutions were then sonicated and vortexed for 1 min, then mixed on a stir plate for 24 h at room temperature. The mixture was washed once by centrifugation at 2500 RPM for 2.5 min and then dried at 70°C for 24 h.

7.3.3 Preparation of HNTS with RITC and Diazepam

After size and purity analysis of the nanotubes were concluded, the Halloysite samples were prepared by loading rhodamine B isothiocyanate (RITC) through stirring, centrifugation, and sonication at various ratios including 10 mg halloysite/1 mL DI water per 0.5, 1, and 2 mg of RITC. The solutions were then sonicated and vortexed for 1 min, then mixed on a stir plate for 24 h at room temperature. It is important to mention that there was no external surface modification of the tubules i.e., the use of polymers. The mixture was washed once by centrifugation at 2500 RPM for 2.5 min and then dried at 70°C for 24 h. When combining HNT with diazepam, the tablet is crushed with a mortar and pestle into a powder form. The ratio of crushed diazepam with pure unmodified halloysite was 1:1 ratio. Utilizing 1mg halloysite/1mL DI water then adding the specific amount of diazepam which was also 1mg. The halloysite is initially weighed and added to DI water whilst sonication is happening to create a super saturated solution of dispersed HNT. Additionally, add the diazepam 1-2min after the halloysite and allowing

it to mix for 10 minutes before stirring the solution for 24 h. at room temperature. Once the solution is finished mixing it is centrifuged at 4000 RPM for 3min. This is to remove any excess drug that has not been loaded inside the tubules. The product is then dried by vacuum suction for 24hr before analysis.

7.3.4 TGA

Thermogravimetric analysis was used to determine the samples weight change during the component burning, showing that the material was loaded inside the clay tubules and its approximate loading percentage. TGA was done on pristine halloysite with a major phase transition at 490 °C, the nanotubes loaded with Diazepam, a medication used to treat anxiety and seizures. The difference in mass decrease during heating between pristine and loaded halloysite allowed us to estimate RITC loading as 10 ± 1 wt %. The analysis for the diazepam loading into the nanotubes gave a larger 20 ± 1 wt % displaying that some of the drug has bound to the outer shell of the nanotube. The results show that in comparison to unmodified halloysite, the diazepam loading is roughly 10 wt % for (obtained as a difference).

7.3.5 Animal Care and Handling

Animal handling, care and the experimental procedures were conducted owing to the guidelines and in conformity with Louisiana Tech University Institutional Animal Care and Use Committee-approved protocols. Wild type C57BL/6NHsd were purchased from Jackson Laboratory and bred according to the need. Animals were maintained under constant environment with 12 h dark/light cycle and cared by providing food and water ad libitum. Randomly 3 female mice and 3 male mice between age groups 8-16 weeks and weight between 8-27 gms were chosen and assigned to each of the following groups.

(1) Sham treatment with vehicle water, (2) Treatment with small HNTs (3) Treatment with large HNTs.

7.3.6 Intranasal Administration

On day zero, each mouse was intranasally delivered a total of 24 μ l of 3 mg/ml HNTs freshly suspended in water. The mice were separated into individual cages and weighed. The mouse was sedated with 2% isoflurane in 500ml/min airflow via anesthetic chamber (Somnosuite digital vaporizer system (Kent Scientific Corporation, Torrington, Connecticut, United States)). After anesthesia, mice were delivered 6 μ l of 1 or 2 mg/ml HNTs into one nostril while in a supine position at 70 degrees, followed by 3 more treatments administered into alternate nostrils with a minute between each treatment. In addition, 3mg/ml (dose determined by preliminary testing) of HNT-loaded diazepam (HNT-diazepam) was administered for 5 days in a similar manner to HNT administration to mice receiving this treatment. During the therapy, the mouse was sedated using a nose cone containing 1% isoflurane. After receiving treatment, the mouse will be returned to its cage and observed for five minutes for seizures or abnormalities. The treatments were continued at the same time point for an additional five days.

7.3.7 Intraperitoneal Administration

To determine the permeability of HNTs to the brain after intraperitoneal administration, mice were given 10% w/v of 2mg/ml HNTs and sacked 4 hours later. The mouse was separated, weighed, and sedated in accordance with the above procedures. Once the mouse was completely sedated, it was positioned supine and given an intraperitoneal dose before being returned to its cage. The mouse was observed for 10 minutes after treatment for seizures or abnormalities.

7.3.8 Rotarod Test

The rotarod test begins three days (-3) prior to the administration of the HNTs. After two days of training on the rotarod (Panlab Model # 76-0770, Harvard Apparatus) (Hiromi) device, the results were recorded on the third day (-1). On -1, 2, 5, and 7 days, the time the mouse spends on the rod and its rpm were recorded. Before each test, the mice were acclimated to the environment for at least 10 minutes to lessen stress, and the rotarod lanes were thoroughly cleaned between each mouse test. Each day, three consecutive trials for each mouse were conducted with a 10-minute rest between trials two and three. The average of the two best trials was documented. This test assesses the locomotor function, coordination, and learning capacities of mice. To minimize variability, the scores were standardized relative to the baseline (-1).

7.3.9 Modified Neurological Severity Score (mNSS)

In this study, mice were assessed on days 2, 5 and 7 on a scale from 0 to 8 for any possible neurological alterations. The following eight behaviors were evaluated: hindlimb flexion, startled response, seeking behavior, capacity of mice to walk on elevated bars 3 cm, 2 cm, and 1 cm broad and 30 cm long, and ability to balance on a 0.5 cm thick circular rod and 0.5cm width square beam (at least for 30 seconds). mNSS was used to assess aberrant motor and muscular conditions, balancing ability, reflexes, visual, proprioceptive, and tactile sensory functions [47]. Each failure task resulted in one point, so an eight-point score indicates severe neurological failure.

7.3.10 Open Field (OF)

Open field tests were conducted to determine the anxiety levels and locomotor abilities of the test mouse as it explored the 30 cm x 30 cm x 25 cm white wooden box in

a controlled environment. The white box provides a contrast for video analysis and offers large open spaces, resulting in mice anxiety due to social isolation and exposure to novel environment. Prior to each test, each mouse was acclimatized to the room for at least ten minutes, and the wooden box was cleaned with alcohol to remove any scents or infections that could have been caused by the mice that had been tested earlier. After placing the mouse in the center of the wooden box, a five-minute movie was captured using a FIJI-programmed camera stationed above the box.

7.3.11 Elevated Plus Maze (EPM)

The EPM tests were conducted in a conditioned environment on a 50 cm-high maze with two open arms and two closed arms. These arms are positioned at right angles to one another, and their closed walls measure 25 cm in height. Prior to testing, mice were acclimated to the room and cleansed the maze to remove any odor from previously tested animals. Mice were then placed in the center of the maze with their backs to the open arms, and five-minute video recordings were taken as the mice explored the maze. This test examines the behavior of mice under stressful settings (high ground) since mice have an innate inclination to avoid high open areas by adhering to closed arms. The recordings were analyzed for the number of entries and the amount of time spent in the open arm.

7.3.12 Novel Object Recognition (NOR)

NOR is a low-stress test used to assess mice's memory deficiencies. This test depends on the mice's natural inclination to investigate novel objects [189]. This test was often conducted following the open field test to provide the necessary acclimatization period. If the test was not completed after OF, the mice will be habituated to their new

surroundings for 5 minutes. The mouse was placed in the center of the box, which contained two objects of identical size at each adjacent corner. The videos were captured for five minutes, then re-recorded for five more minutes during which one object was replaced with a new object of identical size but different shape. Both videos were evaluated to determine the mice's ability to memorize the novel object in relation to the amount of time spent in its vicinity. To limit external stimulation, preventive steps were implemented.

Discrimination index (DI) = $(\text{time spent with novel object} \times 100) / (\text{time spent with identical object} + \text{time spent with novel object})$.

7.3.13 Behavioral Video Analysis (MATLAB)

After being modified with image J software, the behavioral videos were analyzed using MATLAB software. Videos were initially converted to AVI (Audio Video Interleave) files at 10 fps, after which they were edited to remove audio and uncompressed to grayscale. These uncompressed recordings were precisely reduced to 5 minutes, or 300 seconds, and the final frame was modified to remove the mouse so it could be used as the video's background to eliminate background noise. The necessary adjustments, such as altering the angles to fit the square, were made, and then these files were converted to multi-TIFF files, which were then read by MATLAB plugins.

7.3.14 Perfusion and Extraction of Brain

After seven days of behavioral testing, the mice were sacrificed, and their brains were removed for further examination. Mice were sacrificed at 4, 12, 24, 48 hours, 3 days, and 7 days after treatment to assess the permeability of Rhodamine-loaded HNTs. The mouse was removed from the cages, weighed, and transferred to the anesthetic

chamber for sedation with 2% isoflurane and 500 ml/min air flow (Somnosuite digital vaporizer system, Kent Scientific Corporation, Torrington, Connecticut, United States). Once the mouse had been completely anesthetized and placed in a supine position, 10% w/v of ketamine (10mg/kg)/xylazine (1mg/kg in saline) was administered intraperitoneally. The mouse will be returned to its original cage, which will prevent it from fighting back anesthesia. After 15 minutes, a 10% booster dose may be delivered if the mouse is not sufficiently sedated, as determined by pinching the toes and observing the eye reflexes.

Once the mouse was completely sedated, its forelimbs and tail were taped to the surgery table while it was laid in supine position to expose its stomach. A cut was made to expose the thoracic cavity and heart, and then the aorta was punctured to facilitate blood drainage. Once the blood begins to drain, the left ventricle of the mouse was perfused with 25 ml of 1x ice-cold PBS and 25 ml of 4% ice-cold formalin. Utilizing a peristaltic perfusion pump, the liquid was pumped to the ventricle. Once the liver was cleansed, the mouse was decapitated, and the brain was removed using the appropriate surgical tools. The brain was then fixed in 4% formalin for eight hours, after which 30% sucrose was added until saturation at 4°C.

7.3.15 Vibratome Sectioning

Using the oscillating tissue slicer vibratome EMS-500 (Electron Microscopy Sciences, Hatfield, P(A) Fig, the fully saturated brains are sectioned for HNT visualization and distribution. The brains were wiped with a sanitized paper towel to remove any excess sucrose solution, and the brain stem was removed to create a flat base. Later, the brain was encased in a 2% solution of low-melting agarose. Later, the encased

brains were adhered to the mounting block by trimming excess agarose. Once a steady base was achieved, 60 μ m sections were cut. Throughout the process of slicing, the brain is submerged in an ice-cold buffer solution. The slices were transferred with care to a 48-well plate containing PBS solution and stored in the dark until the preparation of slides.

7.3.16 Preparation of Samples for Imaging

The tissue sections were stained with DAPI for 10 minutes at 4°C on a shaker, followed by optical clearing with varying glycerol concentrations. The sections were soaked for 10 minutes in 30%, 50%, 70%, and 90% concentrations of glycerol, respectively. After saturating the sections, they were mounted on slides containing anti-fade mounting media. The sections were arranged from rostral to caudal order, including the olfactory bulb and different regions of the cortex. A cover slip was placed on to the slide with care to avoid trapping of air bubbles that would interfere with imaging. After removing excess media, the cover slip was sealed with nail polish, and the slides were stored in the dark storage box until imaging.

7.3.17 Imaging

The Olympus IX51 was used to capture phase contrast, DAPI, and RITC images of the sections while maintaining the same settings between the images and sections. Multiple regions of the same section were imaged, and several measures were taken to prevent bleaching of the section during imaging, including reducing the light intensity, imaging time, and acquiring RITC images initially, followed by DAPI and bright light.

7.4 Results

To determine the optimal concentration for both intranasal and intraperitoneal administration, HNTs-Rhodamine in water was administered to mice at various

concentrations beginning at 0.5 mg/ml. Even at low concentrations of 1mg/ml, fluorescence has been observed throughout the brain, as per the preliminary data (not included). However, 3 mg/ml has demonstrated superior brain absorption and fluorescence. Consequently, this concentration was utilized in the study. The mice received the dosages specified in the methods section. Later, brains were extracted at various time points to visualize the rhodamine's uptake and distribution. The collected brains were sectioned into 60- μ m thick slices, stained with DAPI, and imaged with phase contrast, fluorescence filters using fluorescence microscopy. Figure 7-1, Figure 7-2, and Figure 7-3 show fluorescence images of the brain slices at different points in time.

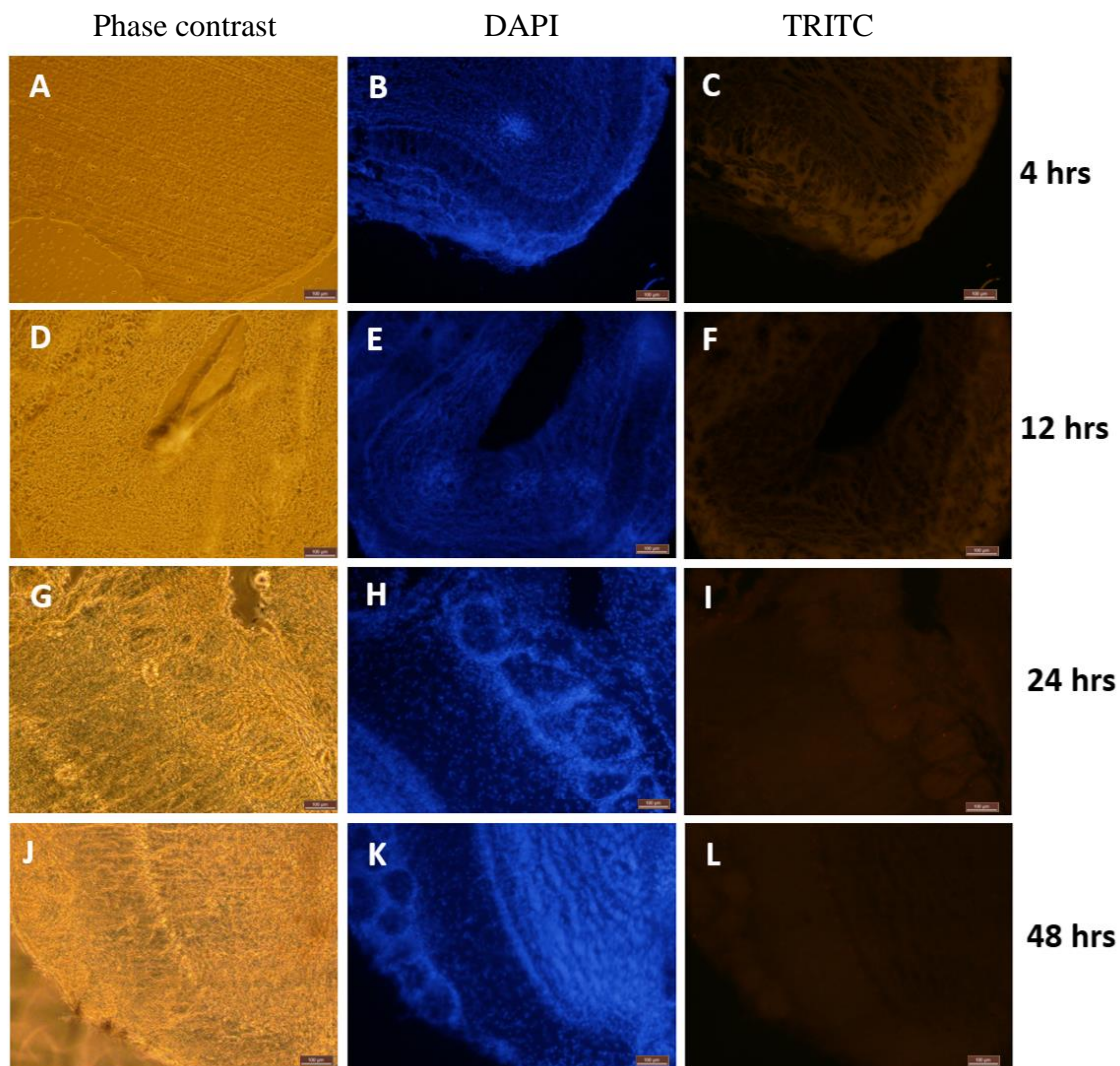


Figure 7-1: Fluorescence images of the brain slices of the olfactory bulb at time points 4, 12, 24 and 48 hours after intranasal administration of HNT-Rhodamine. Images A, D, G, J (first column) are phase contrast images. B, E, H, K (second column) are images acquired through DAPI filter and C, F, I, L (third column) are acquired through TRITC filter. Images from A through F were acquired using 10x objective and G through L were imaged through 40x objective.

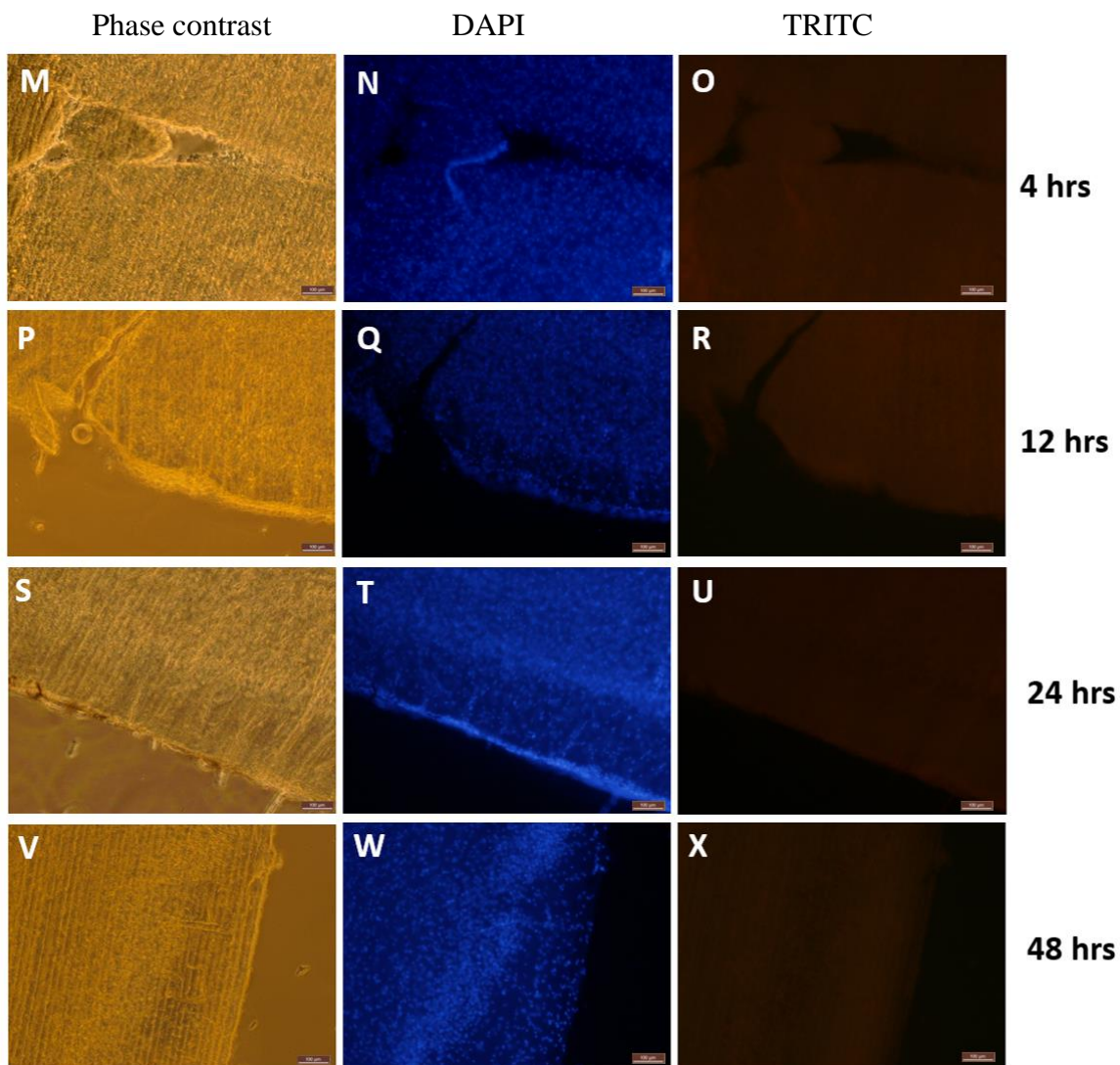


Figure 7-2: Fluorescence images of the brain slices of the cortex region at time points 4, 12, 24 and 48 hours after intranasal administration of HNT-Rhodamine. Images A, D, G, J (first column) are phase contrast images. B, E, H, K (second column) are images acquired through DAPI filter and C, F, I, L (third column) are acquired through TRITC filter. Images from M through R were acquired using 10x objective and S through X were imaged through 40x objective. The scale bar is 100 μ m for images S-X and 31.5 μ m for M-R.

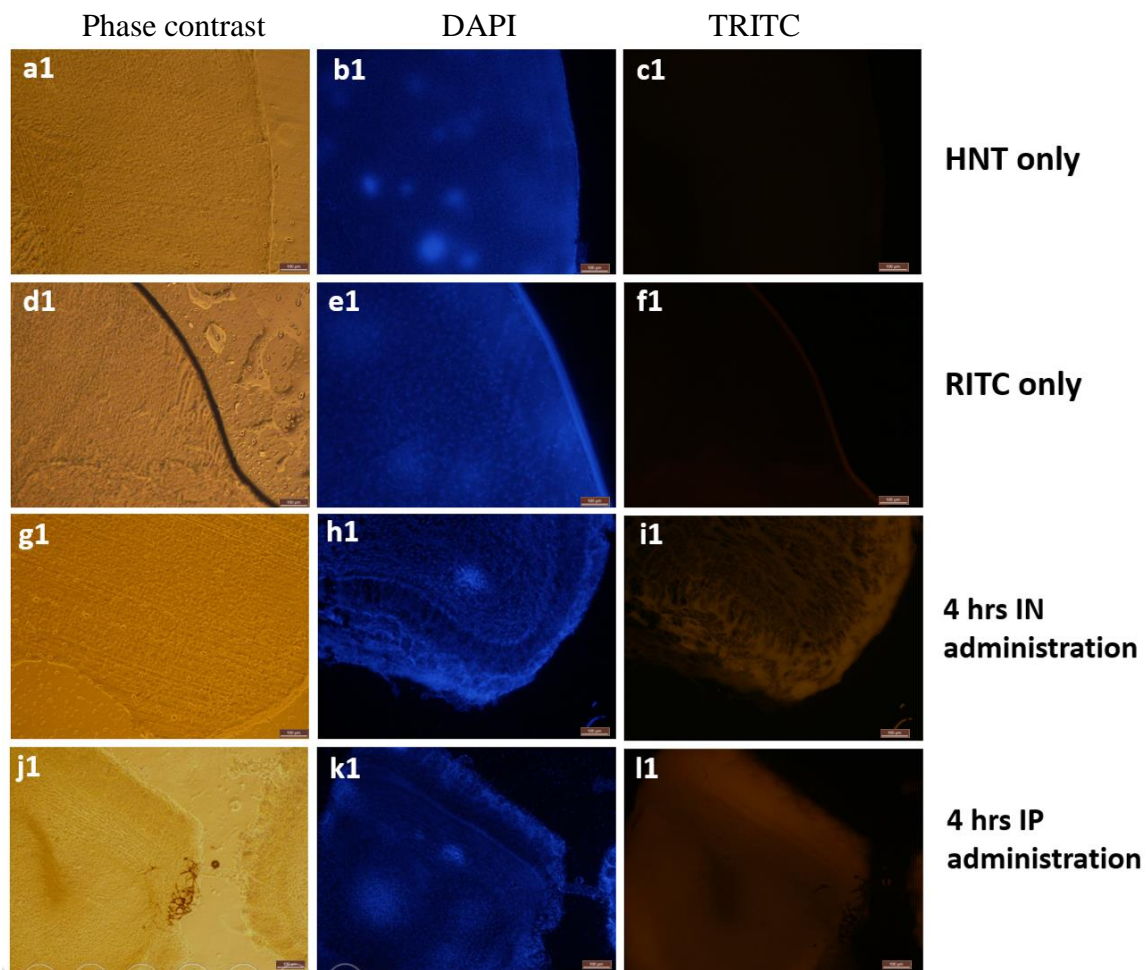


Figure 7-3: Florescence images of the mice brains that were acquired 4 hours after treatment. The first column a1, d1, g1, j1 (first column) are phase contrast images while the second column b1, e1, h1, k1 are images acquired through DAPI filter and third column c1, f1, i1, l1 were acquired using TRITC filter. The first-row images are from the brain after intranasal treatment with HNTs only while second row with intranasal RITC treatment only, third row with intranasal HNT-Rhodamine administration and fourth row was HNT-Rhodamine treatment intraperitoneally. The images were acquired using 40x for a1-i1 and 10x for j1-l1. The scale bar for j1-l1 is 31.5 μ m and a1-i1 is 100 μ m.

Punctate staining throughout the brain is visible in images taken after 4 hours of intranasal and intraperitoneal administration. Mice given HNTs only showed no fluorescence when examined with the TRITC filter at any time point. However, RITC only treated animals exhibited relatively insignificant fluorescence compared to controls. Fluorescence in the olfactory bulb was comparatively higher than the cortex in mice

given treatment for 4 and 12 hours, respectively. Intriguingly, the fluorescence was more consistent across the brain at 24, 48, and 72 hours (not included since the fluorescence was not visible at the same intensity as other time points, but after slightly revising the settings, it was visible). But after seven days, there was no trace of fluorescence anywhere in the brain.

7.4.1 Rotarod Score

Learning and motor cognition abilities were tested during the rotarod test. The greater the neurological damage the latency to fall will be shorter indicating reduced learning and motor cognition in the animal. To reduce variability, the scores from days 2, 5, and 7 were normalized with those from the previous day of treatment. Statistical analysis was conducted using SPSS software. Following data analysis with the T-test and Bonferroni correction, the normalized time of latency to fall is depicted (Figure 7-4).

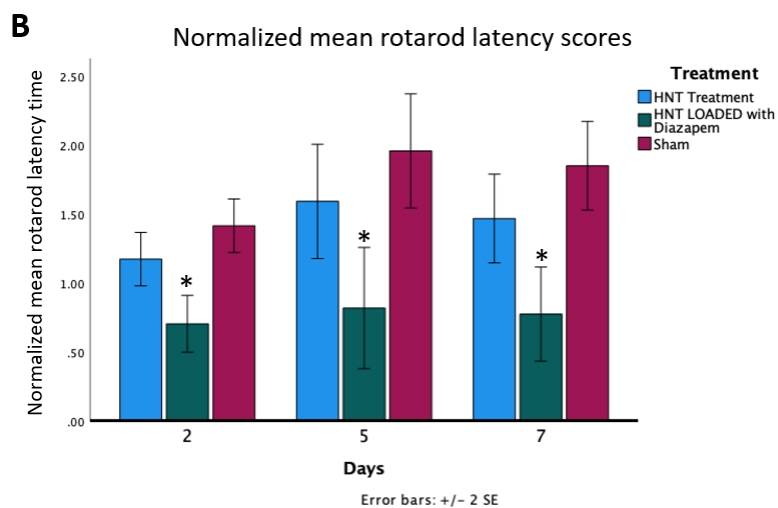


Figure 7-4: Normalized data showing time of latency to the fall on day 2, 5 and 7. The mice were treated with vehicle (sham), HNTs only, and HNT-diazepam for 6 days. Mice were divided into three treatment groups: sham (n=6), HNT (n=6), and HNT-diazepam (n=6). Using pairwise comparison and Bonferroni correction, a T-test statistical analysis was performed. The data revealed a statistically significant difference between control and HNT-diazepam by day 7 ($p=0.002$). A and B represents the same data in different graph forms. (* = $P < 0.05$).

There is a strong trend, beginning on day 2, that mice receiving HNT handle the rotarod as well as the control mice. On days five and seven, the HNTs-Diazepam-treated animals displayed low trends in comparison to both HNT-only mice and control mice. It's clear from these data that HNT-Diazepam mice are generally underperforming compared to both Sham mice and HNT-only treated mice. From the second day on, the HNT mice perform similarly to the control mice. This demonstrates that diazepam loaded HNTs successfully delivered the drug to the brain.

7.4.2 Modified Neurological Severity Score

The neurological severity assessment tests were conducted along with the rotarod test on the same days (Figure 7-5). The purpose of this test was to identify any neurological deficits in mice following treatment. The data revealed that mice treated with HNTs did not vary from control mice, however animals treated with HNT-diazepam had higher scores than the other two groups. Most of the mice that failed the test were unable to balance on thin rods due to diazepam-induced drowsiness.

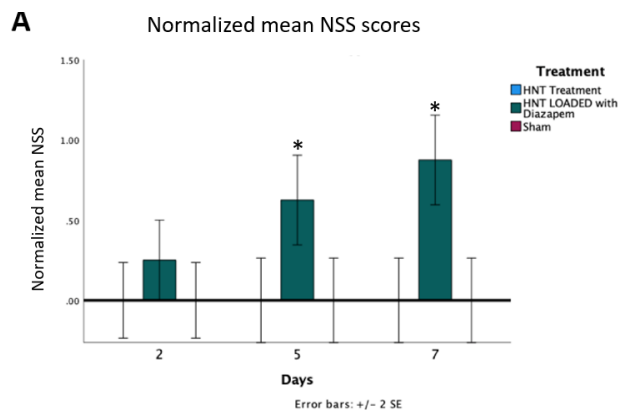


Figure 7-5: Modified neurological severity scores on day 2, 5 and 7. The mice were treated with vehicle (sham), HNTs only, and HNT-diazepam for 6 days. Mice were divided into three treatment groups: sham (n=6), HNT (n=6), and HNT-diazepam (n=6). Using pairwise comparison and Bonferroni correction, a T-test statistical analysis was performed. The data revealed a statistically significant difference between placebo, HNT, and HNT-diazepam, but no difference between placebo and HNT ($p = 1.0$). A and B represents the same data in different graph forms. (* = $P < 0.05$)

On the second day, all three treatment groups are trending towards being the same. However, as treatment days progress, the margin widens. As hypothesized, the mice treated with Diazepam became increasingly distinguishable from the other two treatment groups. This slow change is likely due to relatively minor variations in NSS scores, and the amount of HNT-diazepam dosage required to produce an effect in mice. Hence, it could have been the reason for taking longer than two days to observe the effects.

7.4.3 Weights of the Mice

The mice were weighed before adding to the study and before sacrificing them. There wasn't any significant correlation found with respect to the weights between control and treated mice.

7.4.4 Elevated Plus Maze

The data show that when compared to the sham group and the HNTs only treated group, mice given HNT-Diazepam had a higher percent open arm stay time. Diazepam, an anxiolytic drug, may have reduced stress and caused the mice to investigate the open arms. We also noticed that the overall distance traveled by mice treated with HNT-Diazepam was less than the other two treatments. Figure 7-6 shows test results of the treated and untreated mice.

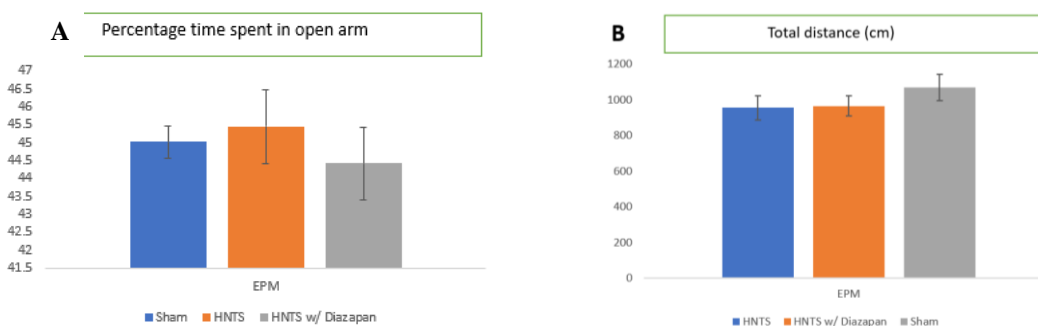


Figure 7-6: Elevated plus maze test results of control, HNT treated, and HNT-diazepam treated mice on day 7. (A) the percentage time spent on the open arm by each group (B) The total distance traveled by the mice in each group (n=6) standard error ± 2 .

7.4.5 Novel Object Recognition

The mice that received HNT alone were identical to the control group, but significantly outperformed the control group. In contrast to the other two groups, the mice treated with HNT spent significantly more time in close proximity to the objects than the other two groups (Figure 7-7). The statistics do not indicate a substantial difference between the control group and the HNT-Diazepam-treated group. In the HNT-Diazepam-treated group, mice spent considerably less time overall in the vicinity of

novel and familiar objects. We observed that mice remained close to one location or corner and moved less.

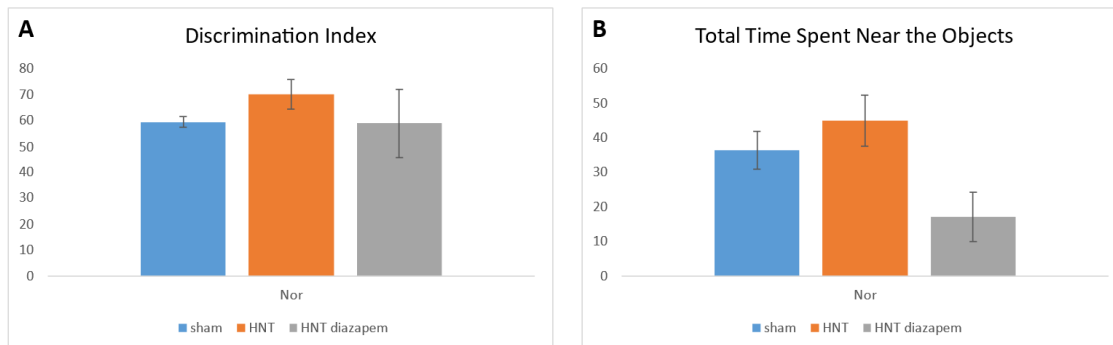


Figure 7-7: Novel object recognition test results of control, HNT, HNT-diazepam on day 7. The data was represented as mean discriminative index and total time spent on open arms (n=6) standard error ± 1 . (* = $P < 0.05$)

7.4.6 Open Field

The mice that received HNT-Diazepam has shown significant reduction in the time spent in the center indicating the effects of diazepam on the performance of the mice to explore the open field. Mice that received HNTs only treatment intranasally has not shown any difference compared to the control mice group. Figure 7-8 shows the open field results of the three test categories.

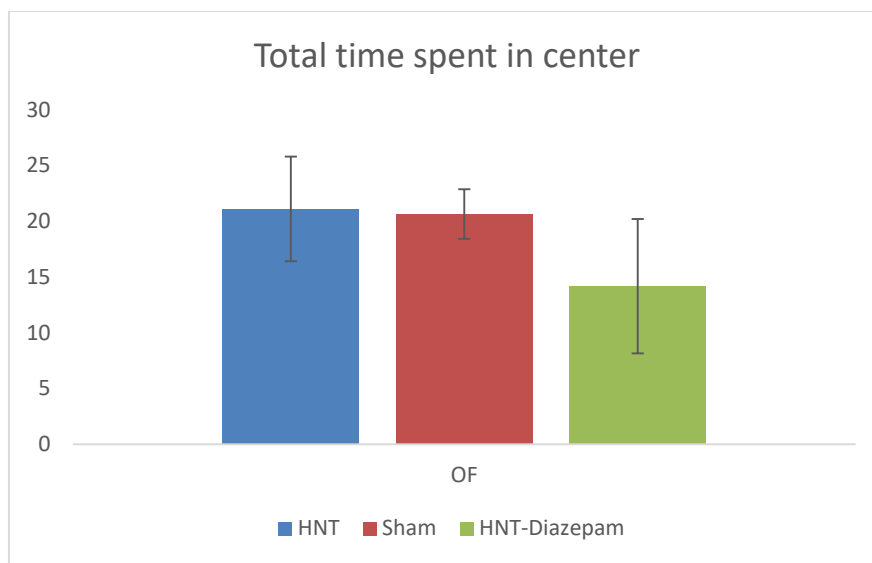


Figure 7-8: Open field results of control, HNT, HNT-diazepam on day 7. The data was represented as mean discriminative index and total time spent on open arms (n=6) standard error ± 1 .

7.4.7 TGA

Thermogravimetric analysis was used to determine the samples weight change during the component burning. Displaying that the material or substance was loaded inside the nanotubes and its approximate percentage. TGA was done on pristine halloysite with a major phase transition at 490 °C, the nanotubes loaded with RITC, and ones with diazepam which is a neurotransmitter used in research to treat brain disorders. The difference in mass decrease during heating between pristine and loaded halloysite allowed us to estimate RITC loading as 10 ± 1 wt %. A similar analysis for diazepam drug loading into the nanotubes gave a larger 20 ± 1 wt % indicating some external drug attachment. The results show that compared to pristine halloysite, diazepam loading is around 10 wt % for (obtained as a difference).

7.5 Discussion

Halloysites (HNTs) are emerging as potential carrier molecules due to their wide availability, sustained drug release capabilities and ability to transport a variety of molecules [208]. These nanotubes were modified and demonstrated their effectiveness in targeted therapy [209], [210]. Additionally, HNTs are evaluated as topical applications, which also exhibited remarkable benefits [211]. Despite efforts to test their abilities across a broad spectrum, they were not evaluated for their ability to bypass the BBB. There is a paucity of research on HNTs in terms of toxicity and behavioral changes associated with halloysites administration to the brain and BBB permeability. We examined the ability of HNTs to penetrate the brain and their distribution in the brain. When administered intranasally (noninvasive route) and intraperitoneally, our findings revealed that HNTs not only permeate the BBB, but also transport the drugs across the barrier and distribute them throughout the brain.

Our findings demonstrated that administration of nanotubules did not result in any behavioral, psychological, or neurological deficits, such as motor, sensory, or cognitive deficits. In addition, they have successfully transported the TRITC dye and diazepam molecules, as confirmed by biodistribution and behavioral analysis data. When the HNTs were administered intranasally, however, a few animals exhibited mild discomfort (gritting teeth) for a couple of minutes. This could have been the result of nasal HNT obstruction. After 72 hours, there was little fluorescence in the samples, and by the seventh day, there was no fluorescence observed. Intranasal administration has demonstrated a higher fluorescence intensity compared to intraperitoneal administration. The absence of fluorescence may be due to the removal of HNTs and RITC from the

brain, or the RITC released by HNTs may have been washed away. However, the fate of HNTs once they enter the brain, the effects of long-term administration of HNTs, and the long-term effects of HNTs on the brain must be investigated. The positive results of this preliminary test could be utilized to expand the study and conduct additional research. If these molecules are not eliminated, HNTs could be used as a single-dose emergency treatment when the patient is uncooperative because they can be administered non-invasively, particularly for conditions such as traumatic brain injury where prompt treatment can prevent secondary injury.

CHAPTER 8

SYNERGETIC EFFECT OF MINOCYCLINE AND ROLIPRAM TO ARREST PROGRESSION OF SECONDARY INJURY POST TBI IN RODENT MODELS

8.1 Introduction

The incidence of traumatic brain injury is the highest among neurological diseases with a late onset of neurological deterioration [27]. Primary or repeated injuries can set off a cascade of metabolic processes that may result in more neurological damage and secondary clinical disorders [60], [212]. Secondary injury can manifest within hours or days and persist for years [213], [214]. Hypoxia, intracranial hypertension, hypotension, hypercapnia, excitotoxicity, reactive oxygenated species (ROS), and other events can cause secondary injury. In addition, inflammatory molecules, which are created as a protective mechanism, have been associated to secondary injury and are known to increase TBI clinical symptoms such as contusion, cell death (necrosis), and cavitation [215], [216]. Recent TBI research has focused mostly on targeting these inflammatory molecules, as these are potential targets to arrest a cascade of adverse biochemical reactions [217]. Minocycline and Rolipram are highly effective anti-inflammatory compounds that are medications available today. However, these molecules' synergistic effects in TBI treatment were not evaluated.

Rolipram is a phosphodiesterase inhibitor that has been shown to promote neuroprotection and neuronal regeneration in many CNS injury models by lowering pathology and inflammation following early administration [89], [215], [218]. However, oral administration of rolipram has been associated with mild digestive discomfort, and intraperitoneal administration has been associated with gastric mucosal damage [219]. To counteract this and promote slow release, PgP nanoparticles loaded Rolipram (PgP-Rm) were intranasally given. In rat spinal cord injury models, PgP-Rm significantly decreased secondary injury and enhanced motor cognition [218]. Similar experiments conducted in our laboratory have demonstrated that minocycline can reduce neuronal varicosities and improve neuronal health [93]. By inhibiting the synthesis of pro-inflammatory molecules via multiple targets, minocycline has been shown to increase neuronal protection and decrease apoptosis in a variety of neurodegenerative disorders [25], [72], [220]. Therefore, these two medications were administered as a combination therapy to evaluate their synergistic effect on the prognosis of TBI. We hypothesized that intranasal administration of PgP-Rm after one hour of injury and intraperitoneal administration of minocycline for six days (initial dose during the first hour) would prevent secondary damage and improve neuronal health in rodent TBI models.

8.1.1 Materials and Methods

8.1.1.1 Treatments

This study includes five groups sham, TBI, Minocycline (MINO), PgP Rolipram (PgP-Rm), Minocycline and PgP Rolipram (MINO+Rm). Sham group mice received no injury and treated with vehicle (water) intranasally and vehicle (saline) intraperitoneally. TBI group received injury and treated with vehicle (water) intranasally and vehicle

(saline) intraperitoneally. MINO group received injury and treated with vehicle (water) intranasally and minocycline intraperitoneally. PgP-Rm received injury and treated with nanoparticles loaded with rolipram intranasally and vehicle (saline) intraperitoneally. MINO+Rm group received injury and treated with minocycline intranasally, and nanoparticles loaded with rolipram intranasally. Minocycline (45/kg) was administered for 6 days starting from the day of injury and a single dose of rolipram nanoparticles (1mg/ml) were administered on the day of injury. The first dose of minocycline and rolipram were administered within one hour after the injury. Rolipram nanoparticles were synthesized in Dr. Jeoung Soo Lee lab from Clemson University. 6 μ l of 1mg/ml PgP-Rm was delivered into each nostril 30 seconds apart, for a total of 24 μ l.

8.2 Results

8.2.1 Behavioral Analysis

In this study, 63 mice, including 31 females and 32 males, were utilized to evaluate the efficacy of treatments to that of untreated mice. Different behavioral tests were conducted to assess treatment-related improvements in behavior, motor cognition, psychological deficits, etc. Potential gender differences in relation to injury and treatment were also evaluated. We expected that injured mice treated with minocycline or rolipram would recover faster than animals that received no treatment. In addition, we hypothesized that mice receiving both treatments would recover faster than those receiving just one treatment. Rotarod and NSS were acquired on days 2, 5 and 7 while epm, nor, of were acquired on day 14.

8.2.2 Rotarod

In comparison to mice in the TBI group, all other groups performed better on every day the data was acquired. The average rotarod latency to fall was normalized by the average latency obtained before the day of injury (day -1). On day 2, except for the sham group, all other groups showed a drop in the mean latency scores, demonstrating injury-induced disruption of motor cognition (Figure 8-1). On days 5 and 7, the mean scores increased significantly for all groups. Even on day 7, none of the groups did as well as the control mice. In contrast to the TBI vehicle-only treated group, mice in the other three groups that received at least one medication treatment exhibited a substantial upward trend.

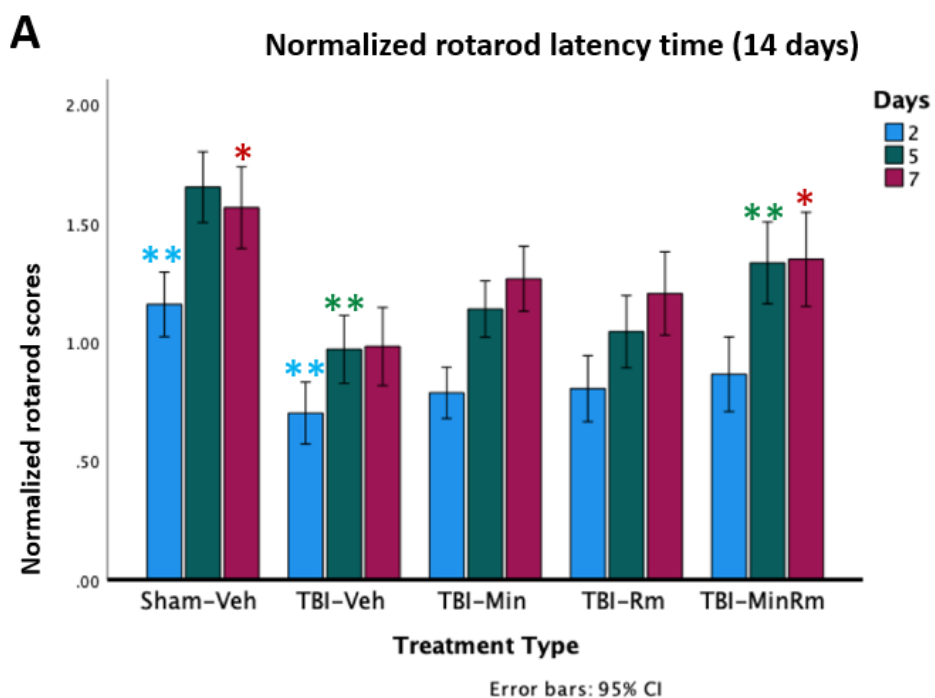


Figure 8-1: Rotarod normalized mean latency time by each groups on day 2, 5 and 7 (n=10) (* = $P > 0.05$; ** = $P < 0.05$)

8.2.3 Mnss

The normalized neurological severity score of treated mice and untreated mice is shown below. Compared to injured mice that did not receive any treatment, all injured mice groups that received at least one treatment had improved neurological scores by the 7th day. However, the group that received both treatments has not exhibited a statistically significant trend with the groups that received at least one drug treatment. All the treated groups have shown better trends compared to the injured mice that received no treatment. Figure 8-2 shows a comparison of the normalized scores.

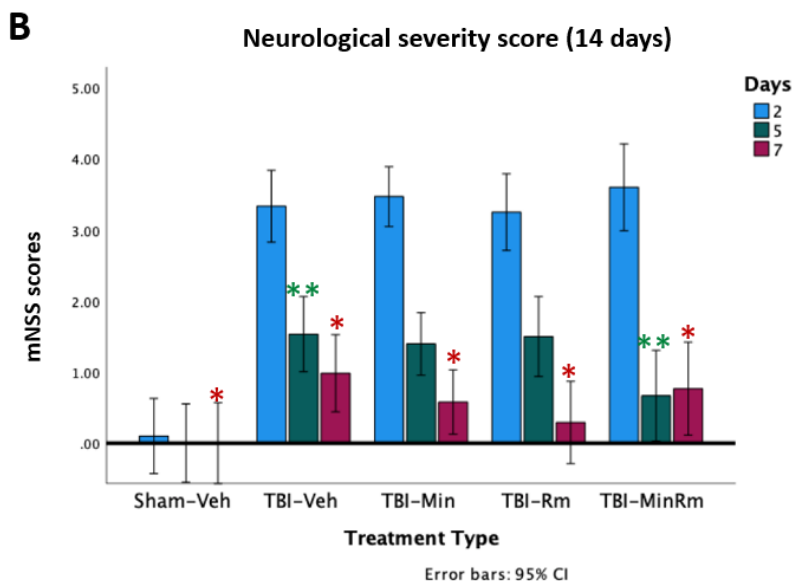


Figure 8-2: mNSS normalized score by each group on day 2, 5 and 7 (n=10). (* = $P > 0.05$; ** = $P < 0.05$)

8.2.4 EPM

The graph below depicts the time spent by mice on the open arms vs closed arms. We anticipated that the open arm stay time of mice treated with rolipram and minocycline would be greater than that of animals treated with vehicle (TBI vehicle). Our data, however, revealed differently. The EPM analysis is displayed in Figure 8-3.

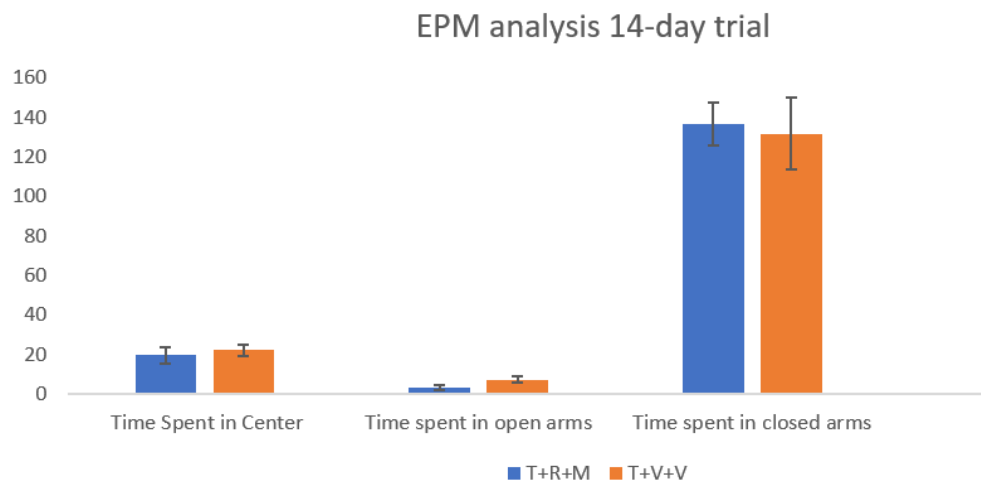


Figure 8-3: Elevated plus maze results of the mice on day 14 between TBI (vehicle) treated and TBI rolipram and minocycline treated.

8.2.5 NOR

The average amount of time each group of mice spent in proximity to the novel object and the familiar object was plotted. The data indicated that, compared to other treatment groups, mice treated with rolipram alone spent significantly more time with unfamiliar objects, with a pattern nearly identical to that of the control group. Contrary to our expectations, the group that got both treatments demonstrated decreased recognition of unfamiliar objects (Figure 8-4).

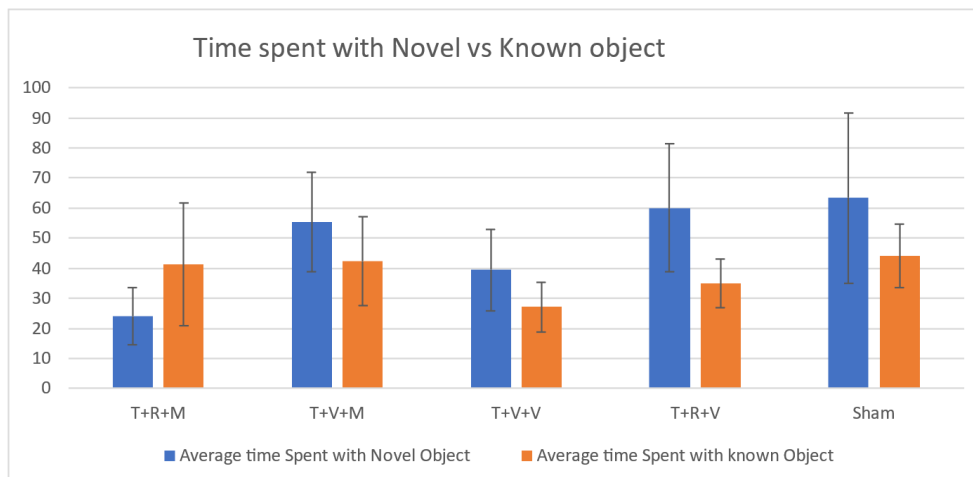


Figure 8-4: Novel object recognition on day 14 across the groups TBI rolipram and minocycline treated, TBI minocycline treated, TBI vehicle treated, TBI rolipram treated, and TBI control. Average time each group spent in proximity to novel versus familiar objects. (* = $P > 0.05$)

8.2.6 IHC Staining

The staining and the slicing procedures were carried out at LSU by Geethika Vutkuri (Dr. Xi lab). Following the IHC protocol for staining, 50 μ m-thick slices of brain tissue were stained with primary antibody to Glial fibrillary acid protein (GFAP) and then with secondary antibody. In response to inflammation or injury, activated astrocytes produce high levels of reactive oxygen species (ROS), inflammatory and proinflammatory cytokines. Activated astroglia expresses high levels of the antibody stained GFAP protein (Figure 8-5 and Figure 8-6).

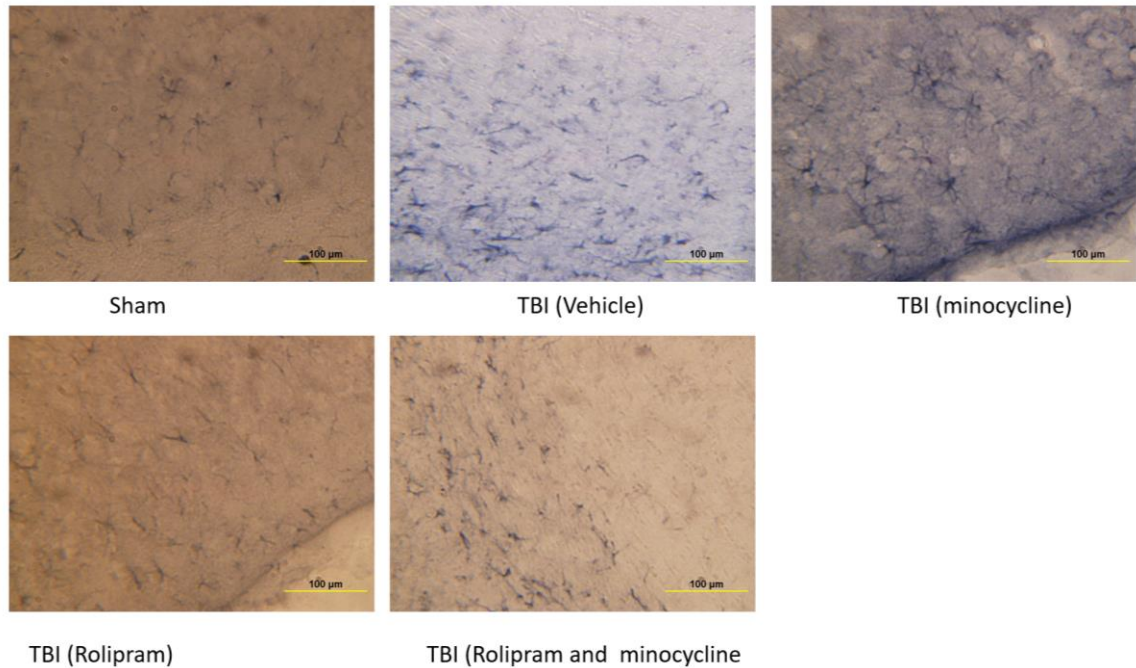


Figure 8-5: GFAP IHC staining allows for the visualization of activated astrocytes. Brain slices (50 μm) were saturated with primary GFAP antibody to detect the highly expressed GFAP protein in activated astroglia. TBI (vehicle) (B) demonstrates greater activation of astroglia than sham (A), TBI (minocycline) (C), TBI (Rolipram) (D), and TBI (Rolipram and minocycline) (E).

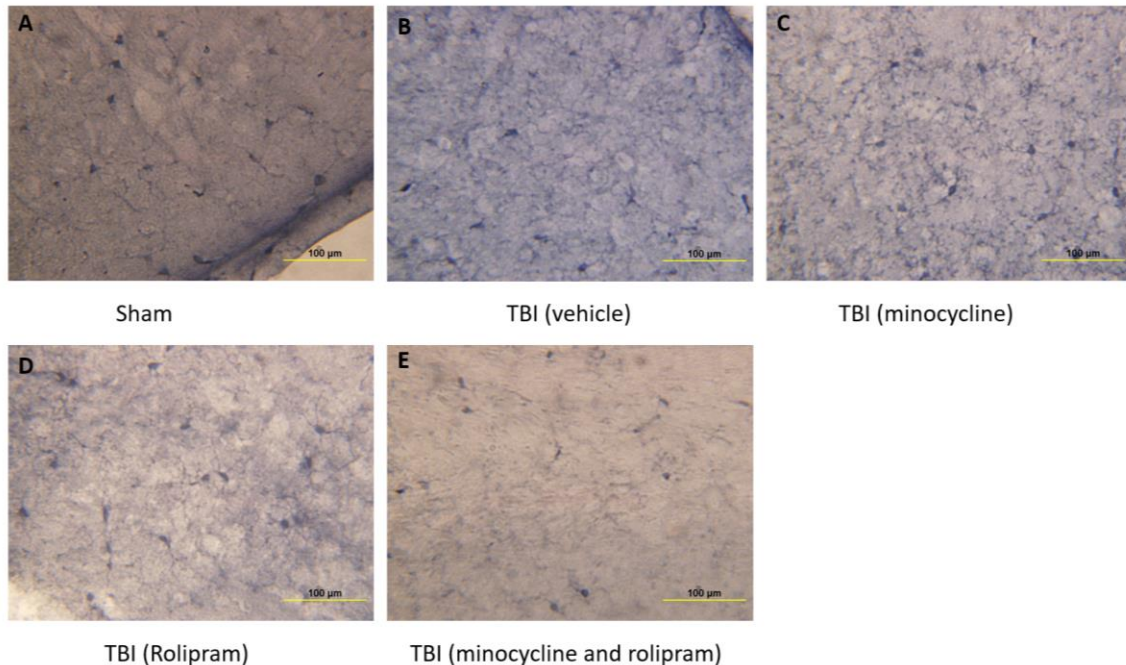


Figure 8-6: IHC staining to visualize the microglial activation (A) sham (B) TBI vehicle (C) TBI (minocycline) (D) TBI (Rolipram) (E) TBI (Minocycline and rolipram)

When activated, astrocytes retract their processes and the cell body (soma) enlarges, allowing them to migrate to the site of injury. This is evident in the stained images, where the control image displays astrocytes with small cell bodies and diffuse processes, whereas the TBI vehicle image displays astrocytes with large cell bodies and small processes. Compared to TBI minocycline treatment, TBI rolipram treatment results in a notably lower number of activated astrocytes. The treatment of TBI with rolipram and minocycline resulted in a significantly lower number of activated astroglia than the other two treatments.

8.3 Discussion

Minocycline has promoted neuronal regeneration in TBI models by reducing inflammation and axonal varicosities. However, minocycline displayed delayed effects at

30 days [174], [175]. Rolipram, on the other hand, has demonstrated excellent neuroprotective effects when administered in early doses in rodent TBI models by acting on phosphodiesterases. Intranasal administration of rolipram-loaded PgP nanoparticles enabled sustained release of the drug and prevented gastric distress. Previous laboratory research by Dr. Claire Jones has demonstrated that PgP nanoparticles administered intranasally penetrate the brain, and that these nanoparticles release rolipram at effective concentrations for up to four days. The effect of a combination of the drugs minocycline and rolipram on TBI models over a 14-day period was studied in an effort to improve TBI outcomes compared to single drug treatment.

Compared to mice groups that did not receive any therapeutic treatment, mice groups that received at least one treatment exhibited enhanced motor and sensory cognition, and histological data revealed a reduction in the activation of astroglia. As hypothesized, there was not a substantial difference between the groups treated with either of the drugs and the group treated with both drugs. However, all treated groups exhibited similar trends to the control group.

CHAPTER 9

CONCLUSIONS AND FUTURE WORK

The primary objective of this study is to identify optimal therapeutics and carriers capable of penetrating the BBB and exercising their therapeutic effects to mitigate the inflammatory response that may initiate secondary injury following TBI. KAFAK is a CPP sequence conjugated to an anti-inflammatory peptide sequence. Initially, the efficacy of the KAFAK peptide was evaluated and compared to that of the AIP and L57 peptides in various cell types. As the results were encouraging, the study was expanded to include in-vivo studies with mice. Previous studies conducted in our lab demonstrated that minocycline is a promising candidate that improved outcomes in mice with traumatic brain injury (TBI). To enhance delayed therapeutic effects, Rolipram and minocycline were tested in combination with each other. In a separate study, we examined the ability of HNTs to transport drugs across the BBB.

Initially, the CPP was compared to other CPP (R8) and RMT (L57) peptides in order to determine the uptake efficiency in primary BMVECs, macrophage, and hepatocyte cell lines. The therapeutic efficacy of KAFAK was compared to that of AIP. The KAFAK peptide demonstrated significantly greater uptake and therapeutic efficacy than the positive control peptides utilized in this study. KAFAK has inhibited the

production of CXCL8 and TNF to levels close to those of the control and has demonstrated exceptional cell viability. Real-time visualization has revealed that the peptide is rapidly absorbed within the first few minutes, even at low concentrations. The peptide diffused throughout the cytoplasm of the cells and entered their nuclei. The fact that it has been widely adopted by primary BMVECs testifies to its ability to traverse the BBB. Following the validation of the peptide's potential by cell studies, we moved on to in vivo studies.

This is the first study to examine the ability of KAFAK to cross the BBB and induce its therapeutic effects. Therefore, preliminary research was conducted to determine the optimal concentrations, dosages, and administration routes. Significant reductions in the proinflammatory cytokines IL-6, IL-1, and TNF were observed following IP administration of KAFAK. Intriguingly, non-invasive IN administration has demonstrated superior absorption and therapeutic efficacy at significantly lower doses. Behavioral studies also demonstrated the neuronal benefits of KAFAK IN treatment. Direct access to the brain, portability, and the possibility of using lower concentrations than would be possible if the drug were administered systemically are just a few of the many demonstrated advantages of IN administration. A facile route of administration for targeting CNS diseases.

This is a preliminary study, and additional tests can be conducted to examine the KAFAK's toxicity, transport mechanism, dosing frequency, biological plausibility, tolerability, safety profile, pharmacokinetic and pharmacodynamic properties, and neuronal regeneration effects. The study used a small number of mice to examine the differences between genders, which did not reveal significant differences. Due to a lack

of resources and time, IHC staining that could have revealed the activation of astroglia and microglia was not performed. In spinal cord injury, KAFAK and BDNF have reduced inflammation and promoted neuronal regeneration [98]. KAFAK's synergistic effects with other drugs and neuroprotective agents are worth exploring.

In an additional 14-day study, the synergistic effects of minocycline and rolipram were evaluated. The rolipram-loaded nanoparticles were administered IN to counteract adverse effects and promote sustained drug release. Behavioral studies indicate that minocycline alone and rolipram alone have resulted in better outcomes. However, the drug combination therapy has not produced the expected behavioral responses. Despite the fact that IHC-stained images are promising, additional analysis is required to measure the intensity. Furthermore, changes in axonal varicosities in vivo can be investigated.

HNTs have shown promise as a powerful drug carrier, but almost no research has shown that they can cross the BBB. Tagged HNTs successfully delivered drugs to primary BMVECs (in vitro model simulating the BBB)[86]. This motivated us to conduct the first in vivo test of HNTs' capacity to transport the drug across the brain. By observing the absorption of fluorescently labeled HNTs, we were able to determine the dosages and administration routes used. Our studies demonstrated that HNTs can transport rhodamine dye and diazepam across the brain.

As a positive control, diazepam was used to test the ability of HNTs to deliver the drug to the brain and display its effects. The diazepam-related behavioral changes of the treated mice were observed. The TGA analysis revealed differences in weight between HNTs and HNT-Diazepam, which indicates drug loading. However, additional testing is required to determine whether the diazepam was loaded inside or coated on top of HNTs.

Since the behavioral studies indicate drug effects on day 7 when treatments were only administered through day 5, it's safe to assume that some of the drug has loaded inside. Additional tests can be conducted to investigate the HNT's toxicity, safety profile, pharmacokinetics, dosing frequency, transport mechanism, and pharmacodynamics.

Overall, this is a diverse investigation to identify optimal carriers for transporting a wide range of potent molecules available on the market across the BBB without altering the therapeutic concentrations and structural changes that are most prevalent at the BBB's tight junctions. This study may be utilized to design potential biomarkers or nanoparticles conjugated with markers for targeted drug therapy. The promising findings of these preliminary studies can be replicated in subsequent, more in-depth research.

9.1 Additional Work

9.1.1 Implanting Silicone Probes for Detection of Glutamate and GABA

The silicone probe was implanted surgically to detect neurotransmitter in the rat brain. As described in Chapter 6, a rat was sedated with 4-5% isoflurane for at least 5 minutes. Once the rat was sedated, ketamine HCl (75 mg/kg) and dexmedetomidine HCl (0.25 mg/kg) were administered intramuscularly to induce complete anesthesia. The rat was then returned to its cage until the absence of optical and toe pinching reflexes confirmed that it was fully sedated.

The surgical plane was shaved, and the rat was secured with ear bars on the surgery table. Eye gel was administered, and the dorsal skull was cleaned three times with alcohol and iodine. A midline incision was made from the rostral (between eye sockets) to the base of the skull. The surgical area's skin was pulled using a d 80 spreader. Using a scalpel, the connective tissue was removed, cleansed to remove blood, and

cauterized to cease blood flow. The region was afterwards washed with saline, hydrogen peroxide, and dried with gauze. For bregma sutures to be visible, the skull is cleaned with isopropyl alcohol.

Using the rat atlas, the coordinates for implanting the probe in CA1 of the hippocampus were calculated. With reference to bregma, the obtained coordinates are +3 mm lateral, -4.6 mm caudal, and 2.5 mm depth (from the pial surface). Using a 1.25mm dental burr mounted to the stereotaxic frame, four holes were drilled without damaging the pial surface. To anchor the head plate, three 1.59mm surgical screws were placed in three holes. Using a 27G needle and a surgical microscope, the pial surface was pierced after removing debris from the hole. Blood flow may have interfered with the recordings if the vasculature underneath the pial surface was damaged. The probe was carefully lowered into the brain utilizing the bulldog clamp linked to the stereotaxic frame. In addition, a reference wire was attached to one of the screws close to the bregma. Dental acrylic was utilized to secure the probe, reference wire, and screws. To counteract the anesthesia, intramuscular atipamezole hydrochloride (1 mg/kg) was administered, followed by application of analgesic and antibacterial powder at the surgery site. Rat was observed for at least ten minutes until it awakens from anesthesia and began to move in its cage. Initial recordings were taken within the first four hours to monitor the levels of GABA and glutamate and continued until day 5.

APPENDIX A
REAGENT RECIPES

Reagent Recipes

The recipes for the various reagents employed in this study are incorporated in the appendix.

Formalin (4%)

After dissolving 4 g of NaH_2PO_4 and 6.5 g of Na_2HPO_4 in 900 mls of DI water, 100 mls of 37% formaldehyde was added and made up to 1000 mls, stored at 4 °C in a glass container.

Cryopreservative

A magnetic bar was used to gently stir 300 mL of ethylene glycol, 300 mL of glycerol, and 100 mL of 0.2M PBS to make 1000 mL of cryoprotectant. After adding 300 mL of distilled water, the solution was stirred again until homogenous and stored at -20 °C or 4 °C. For cryopreservation at -20°C, the PBS from the wells containing slices was removed and add 100 µl of cryoprotectant.

Antifade Mounting Media (brain slices)

To 20mM Tris (final concentration) with a pH of 8.0, add 0.5% N-propyl gallate and warmed glycerol while continuously stirring to achieve 90% glycerol. This is stored at 4°C. A 6-8 µl of anti-fade media was used per slice for visualizing.

REFERENCES

- [1] T. Uhlig *et al.*, “The emergence of peptides in the pharmaceutical business: From exploration to exploitation,” *EuPA Open Proteomics*, vol. 4, pp. 58–69, Sep. 2014, doi: 10.1016/J.EUPROT.2014.05.003.
- [2] Y. Xiong, A. Mahmood, and M. Chopp, “Animal models of traumatic brain injury,” *Nat. Rev. Neurosci. 2013 142*, vol. 14, no. 2, pp. 128–142, Jan. 2013, doi: 10.1038/nrn3407.
- [3] V. K. Gribkoff and L. K. Kaczmarek, “The Need for New Approaches in CNS Drug Discovery: Why Drugs Have Failed, and What Can Be Done to Improve Outcomes,” *Neuropharmacology*, vol. 120, p. 11, Jul. 2017, doi: 10.1016/J.NEUROPHARM.2016.03.021.
- [4] P. S. Ledwidge, “Review of ‘Understanding Traumatic Brain Injury: Current Research and Future Directions,’ edited by Harvey S. Levin, David H. K. Shum, and Raymond C. K. Chan,” <https://doi.org/10.1080/87565641.2015.1020947>, vol. 40, no. 2, pp. 98–100, Feb. 2015, doi: 10.1080/87565641.2015.1020947.
- [5] R. Diaz-Arrastia *et al.*, “Pharmacotherapy of Traumatic Brain Injury: State of the Science and the Road Forward: Report of the Department of Defense Neurotrauma Pharmacology Workgroup,” *J. Neurotrauma*, vol. 31, no. 2, p. 135, Jan. 2014, doi: 10.1089/NEU.2013.3019.
- [6] M. Galgano, G. Toshkezi, X. Qiu, T. Russell, L. Chin, and L.-R. Zhao, “Traumatic Brain Injury: Current Treatment Strategies and Future Endeavors,” <https://doi.org/10.1177/0963689717714102>, vol. 26, no. 7, pp. 197–206, Jun. 2017, doi: 10.1177/0963689717714102.
- [7] H. E. Hinson, S. Rowell, and M. Schreiber, “Clinical evidence of inflammation driving secondary brain injury: A systematic review,” *J. Trauma Acute Care Surg.*, vol. 78, no. 1, p. 184, Jan. 2015, doi: 10.1097/TA.0000000000000468.
- [8] J. L. Lau and M. K. Dunn, “Therapeutic peptides: Historical perspectives, current development trends, and future directions,” *Bioorg. Med. Chem.*, vol. 26, no. 10, pp. 2700–2707, Jun. 2018, doi: 10.1016/J.BMC.2017.06.052.
- [9] P. MM and P. BM, “Crossing the Blood-Brain Barrier: Recent Advances in Drug Delivery to the Brain,” *CNS Drugs*, vol. 31, no. 2, pp. 109–133, Feb. 2017, doi: 10.1007/S40263-016-0405-9.

- [10] R. Shawahna, X. Decleves, and J.-M. Scherrmann, “Hurdles with Using In Vitro Models to Predict Human Blood-brain Barrier Drug Permeability: A Special Focus on Transporters and Metabolizing Enzymes,” *Curr. Drug Metab.*, vol. 14, no. 1, pp. 120–136, Feb. 2013, doi: 10.2174/1389200211309010120.
- [11] L. JL and D. MK, “Therapeutic peptides: Historical perspectives, current development trends, and future directions,” *Bioorg. Med. Chem.*, vol. 26, no. 10, pp. 2700–2707, Jun. 2018, doi: 10.1016/J.BMC.2017.06.052.
- [12] B. JL, C. BK, S. BL, and P. A, “Cell-penetrating peptides can confer biological function: regulation of inflammatory cytokines in human monocytes by MK2 inhibitor peptides,” *J. Control. Release*, vol. 155, no. 2, pp. 128–133, Oct. 2011, doi: 10.1016/J.JCONREL.2011.05.007.
- [13] S. Stalmans *et al.*, “Cell-Penetrating Peptides Selectively Cross the Blood-Brain Barrier In Vivo,” *PLoS One*, vol. 10, no. 10, p. e0139652, Oct. 2015, doi: 10.1371/JOURNAL.PONE.0139652.
- [14] W. M. Pardridge, “Blood-brain barrier delivery,” *Drug Discov. Today*, vol. 12, no. 1–2, pp. 54–61, Jan. 2007, doi: 10.1016/J.DRUDIS.2006.10.013.
- [15] W. M. Pardridge, “Blood-Brain Barrier and Delivery of Protein and Gene Therapeutics to Brain,” *Front. Aging Neurosci.*, vol. 0, p. 373, Jan. 2020, doi: 10.3389/FNAGI.2019.00373.
- [16] S. Y. Ng and A. Y. W. Lee, “Traumatic Brain Injuries: Pathophysiology and Potential Therapeutic Targets,” *Front. Cell. Neurosci.*, vol. 13, p. 528, Nov. 2019, doi: 10.3389/FNCEL.2019.00528/BIBTEX.
- [17] L. S. Chiu, R. S. Anderton, N. W. Knuckey, and B. P. Meloni, “Peptide Pharmacological Approaches to Treating Traumatic Brain Injury: a Case for Arginine-Rich Peptides,” *Mol. Neurobiol.* 2016 5410, vol. 54, no. 10, pp. 7838–7857, Nov. 2016, doi: 10.1007/S12035-016-0287-3.
- [18] B. A. Bony and F. M. Kievit, “A Role for Nanoparticles in Treating Traumatic Brain Injury,” *Pharm.* 2019, Vol. 11, Page 473, vol. 11, no. 9, p. 473, Sep. 2019, doi: 10.3390/PHARMACEUTICS11090473.
- [19] R. Vink and A. J. Nimmo, “Multifunctional Drugs for Head Injury,” *Neurotherapeutics*, vol. 6, no. 1, pp. 28–42, Jan. 2009, doi: 10.1016/J.NURT.2008.10.036.
- [20] A. Frati *et al.*, “Diffuse Axonal Injury and Oxidative Stress: A Comprehensive Review,” *Int. J. Mol. Sci.*, vol. 18, no. 12, Dec. 2017, doi: 10.3390/IJMS18122600.
- [21] J. W. Finnie and P. C. Blumbergs, “Traumatic Brain Injury,” *Vet. Pathol.*, vol. 39, no. 6, pp. 679–689, Jun. 2002, doi: 10.1354/VP.39-6-679/ASSET/IMAGES/LARGE/10.1354_VP.39-6-679-FIG3.JPEG.

- [22] A. A. B. Jamjoom, J. Rhodes, P. J. D. Andrews, and S. G. N. Grant, “The synapse in traumatic brain injury,” *Brain*, vol. 144, no. 1, p. 18, Jan. 2021, doi: 10.1093/BRAIN/AWAA321.
- [23] C. E. R. De Almeida, J. L. De Sousa Filho, J. C. Dourado, P. A. M. Gontijo, M. A. Dellaretti, and B. S. Costa, “Traumatic Brain Injury Epidemiology in Brazil,” *World Neurosurg.*, vol. 87, pp. 540–547, Mar. 2016, doi: 10.1016/J.WNEU.2015.10.020.
- [24] “Report to Congress on mild traumatic brain injury in the United States; steps to prevent a serious public health problem.” 2003, Accessed: Nov. 02, 2022. [Online]. Available: <https://stacks.cdc.gov/view/cdc/6544>.
- [25] R. B. Shultz and Y. Zhong, “Minocycline targets multiple secondary injury mechanisms in traumatic spinal cord injury,” *Neural Regen. Res.*, vol. 12, no. 5, pp. 702–713, May 2017, doi: 10.4103/1673-5374.206633.
- [26] S. Sulhan, K. A. Lyon, L. A. Shapiro, and J. H. Huang, “Neuroinflammation and blood-brain barrier disruption following traumatic brain injury: Pathophysiology and potential therapeutic targets,” *J. Neurosci. Res.*, vol. 98, no. 1, pp. 19–28, Jan. 2020, doi: 10.1002/JNR.24331.
- [27] A. I. R. Maas *et al.*, “Traumatic brain injury: progress and challenges in prevention, clinical care, and research,” *Lancet Neurol.*, vol. 21, no. 11, pp. 1004–1060, Nov. 2022, doi: 10.1016/S1474-4422(22)00309-X.
- [28] K. M. Webster, M. Sun, P. Crack, T. J. O’Brien, S. R. Shultz, and B. D. Semple, “Inflammation in epileptogenesis after traumatic brain injury,” *J. Neuroinflammation*, vol. 14, no. 1, Jan. 2017, doi: 10.1186/S12974-016-0786-1.
- [29] B. S. Varnamkhasti *et al.*, “Cell-Penetrating Peptides: As a Promising Theranostics Strategy to Circumvent the Blood-Brain Barrier for CNS Diseases,” *Curr. Drug Deliv.*, vol. 17, no. 5, pp. 375–386, Apr. 2020, doi: 10.2174/1567201817666200415111755.
- [30] X. Zhou, Q. R. Smith, and X. Liu, “Brain penetrating peptides and peptide–drug conjugates to overcome the blood–brain barrier and target CNS diseases,” *Wiley Interdiscip. Rev. Nanomedicine Nanobiotechnology*, vol. 13, no. 4, p. e1695, Jul. 2021, doi: 10.1002/WNAN.1695.
- [31] D. H. Smith, D. F. Meaney, and W. H. Shull, “Diffuse Axonal Injury in Head Trauma,” *undefined*, vol. 18, no. 4, pp. 307–316, 2003, doi: 10.1097/00001199-200307000-00003.
- [32] M. Inglese *et al.*, “Diffuse axonal injury in mild traumatic brain injury: a diffusion tensor imaging study,” *J. Neurosurg.*, vol. 103, no. 2, pp. 298–303, Aug. 2005, doi: 10.3171/JNS.2005.103.2.0298.

- [33] X. Y. Li and D. F. Feng, "Diffuse axonal injury: novel insights into detection and treatment," *J. Clin. Neurosci.*, vol. 16, no. 5, pp. 614–619, May 2009, doi: 10.1016/J.JOCN.2008.08.005.
- [34] P. C. Blumbergs, N. R. Jones, and J. B. North, "Diffuse axonal injury in head trauma," *J. Neurol. Neurosurg. Psychiatry*, vol. 52, no. 7, pp. 838–841, 1989, doi: 10.1136/JNNP.52.7.838.
- [35] J. M. Meythaler, J. D. Peduzzi, E. Eleftheriou, and T. A. Novack, "Current concepts: Diffuse axonal injury-associated traumatic brain injury," *Arch. Phys. Med. Rehabil.*, vol. 82, no. 10, pp. 1461–1471, 2001, doi: 10.1053/apmr.2001.25137.
- [36] A. Denes, P. Thornton, N. J. Rothwell, and S. M. Allan, "Inflammation and brain injury: Acute cerebral ischaemia, peripheral and central inflammation," *Brain. Behav. Immun.*, vol. 24, no. 5, pp. 708–723, Jul. 2010, doi: 10.1016/J.BBI.2009.09.010.
- [37] T. Woodcock and M. C. Morganti-Kossmann, "The role of markers of inflammation in traumatic brain injury," *Front. Neurol.*, vol. 4 MAR, p. 18, 2013, doi: 10.3389/FNEUR.2013.00018/BIBTEX.
- [38] P. M. Lenzlinger, M. C. Morganti-Kossmann, H. L. Laurer, and T. K. McIntosh, "The duality of the inflammatory response to traumatic brain injury," *Mol. Neurobiol.* 2001 241, vol. 24, no. 1, pp. 169–181, 2001, doi: 10.1385/MN:24:1-3:169.
- [39] M. C. Morganti-Kossmann, M. Rancan, P. F. Stahel, and T. Kossmann, "Inflammatory response in acute traumatic brain injury: a double-edged sword," *Curr. Opin. Crit. Care*, vol. 8, no. 2, pp. 101–105, 2002, doi: 10.1097/00075198-200204000-00002.
- [40] S. Amor, F. Puentes, D. Baker, and P. Van Der Valk, "Inflammation in neurodegenerative diseases," *Immunology*, vol. 129, no. 2, pp. 154–169, Feb. 2010, doi: 10.1111/J.1365-2567.2009.03225.X.
- [41] J. Stephenson, E. Nutma, P. van der Valk, and S. Amor, "Inflammation in CNS neurodegenerative diseases," *Immunology*, vol. 154, no. 2, pp. 204–219, Jun. 2018, doi: 10.1111/IMM.12922.
- [42] K. Shi, J. Zhang, J. fei Dong, and F. D. Shi, "Dissemination of brain inflammation in traumatic brain injury," *Cell. Mol. Immunol.* 2019 166, vol. 16, no. 6, pp. 523–530, Mar. 2019, doi: 10.1038/s41423-019-0213-5.
- [43] T. Rodney, N. Osier, and J. Gill, "Pro- and anti-inflammatory biomarkers and traumatic brain injury outcomes: A review," *Cytokine*, vol. 110, pp. 248–256, Oct. 2018, doi: 10.1016/J.CYTO.2018.01.012.

- [44] J. P. Rodrigues, N. Prajapati, M. A. DeCoster, S. Poh, and T. A. Murray, "Efficient LRP1-Mediated Uptake and Low Cytotoxicity of Peptide L57 In Vitro Shows Its Promise as CNS Drug Delivery Vector," *J. Pharm. Sci.*, vol. 110, no. 2, pp. 824–832, Feb. 2021, doi: 10.1016/J.XPHS.2020.09.019.
- [45] E. Csuka, M. C. Morganti-Kossmann, P. M. Lenzlinger, H. Joller, O. Trentz, and T. Kossmann, "IL-10 levels in cerebrospinal fluid and serum of patients with severe traumatic brain injury: relationship to IL-6, TNF- α , TGF- β 1 and blood–brain barrier function," *J. Neuroimmunol.*, vol. 101, no. 2, pp. 211–221, Nov. 1999, doi: 10.1016/S0165-5728(99)00148-4.
- [46] K. Kamm, W. VanderKolk, C. Lawrence, M. Jonker, and A. T. Davis, "The effect of traumatic brain injury upon the concentration and expression of interleukin-1 β and interleukin-10 in the rat," *J. Trauma - Inj. Infect. Crit. Care*, vol. 60, no. 1, pp. 152–157, Jan. 2006, doi: 10.1097/01.TA.0000196345.81169.A1.
- [47] K. L. Schaar, M. M. Brennehan, and S. I. Savitz, "Functional assessments in the rodent stroke model," *Exp. Transl. Stroke Med.*, vol. 2, no. 1, pp. 1–11, Jul. 2010, doi: 10.1186/2040-7378-2-13/FIGURES/4.
- [48] D. Brough, N. J. Rothwell, and S. M. Allan, "Interleukin-1 as a pharmacological target in acute brain injury," *Exp. Physiol.*, vol. 100, no. 12, pp. 1488–1494, Dec. 2015, doi: 10.1113/EP085135.
- [49] M. Galgano, G. Toshkezi, X. Qiu, T. Russell, L. Chin, and L.-R. Zhao, "Traumatic Brain Injury: Current Treatment Strategies and Future Endeavors," <https://doi.org/10.1177/0963689717714102>, vol. 26, no. 7, pp. 197–206, Jun. 2017, doi: 10.1177/0963689717714102.
- [50] J. L. Alves, "Blood-brain barrier and traumatic brain injury," *J. Neurosci. Res.*, vol. 92, no. 2, pp. 141–147, Feb. 2014, doi: 10.1002/JNR.23300.
- [51] A. Chodobski, B. J. Zink, and J. Szmydynger-Chodobska, "Blood–Brain Barrier Pathophysiology in Traumatic Brain Injury," *Transl. Stroke Res. 2011 24*, vol. 2, no. 4, pp. 492–516, Nov. 2011, doi: 10.1007/S12975-011-0125-X.
- [52] L. Price, C. Wilson, and G. Grant, "Blood–Brain Barrier Pathophysiology following Traumatic Brain Injury," *Transl. Res. Trauma. Brain Inj.*, pp. 85–96, Apr. 2016, doi: 10.1201/b18959-9.
- [53] J. L. Alves, "Blood–brain barrier and traumatic brain injury," *J. Neurosci. Res.*, vol. 92, no. 2, pp. 141–147, Feb. 2014, doi: 10.1002/JNR.23300.
- [54] A. Cash and M. H. Theus, "Mechanisms of Blood-Brain Barrier Dysfunction in Traumatic Brain Injury," *Int. J. Mol. Sci.*, vol. 21, no. 9, May 2020, doi: 10.3390/IJMS21093344.

- [55] H. Alluri, K. Wiggins-Dohlvik, M. L. Davis, J. H. Huang, and B. Tharakan, "Blood–brain barrier dysfunction following traumatic brain injury," *Metab. Brain Dis.* 2015 305, vol. 30, no. 5, pp. 1093–1104, Jan. 2015, doi: 10.1007/S11011-015-9651-7.
- [56] B. Oller-Salvia, M. Sánchez-Navarro, E. Giralt, and M. Teixidó, "Blood–brain barrier shuttle peptides: an emerging paradigm for brain delivery," *Chem. Soc. Rev.*, vol. 45, no. 17, pp. 4690–4707, Aug. 2016, doi: 10.1039/C6CS00076B.
- [57] K. Thapa, H. Khan, T. G. Singh, and A. Kaur, "Traumatic Brain Injury: Mechanistic Insight on Pathophysiology and Potential Therapeutic Targets," *J. Mol. Neurosci.* 2021 719, vol. 71, no. 9, pp. 1725–1742, May 2021, doi: 10.1007/S12031-021-01841-7.
- [58] M. B. Potts *et al.*, "Traumatic Injury to the Immature Brain: Inflammation, Oxidative Injury, and Iron-Mediated Damage as Potential Therapeutic Targets," *NeuroRX*, vol. 3, no. 2, pp. 143–153, Apr. 2006, doi: 10.1016/J.NURX.2006.01.006.
- [59] A. Jarrahi *et al.*, "Revisiting Traumatic Brain Injury: From Molecular Mechanisms to Therapeutic Interventions," *Biomed. 2020, Vol. 8, Page 389*, vol. 8, no. 10, p. 389, Sep. 2020, doi: 10.3390/BIOMEDICINES8100389.
- [60] H. M. Bramlett and W. D. Dietrich, "Long-Term Consequences of Traumatic Brain Injury: Current Status of Potential Mechanisms of Injury and Neurological Outcomes," *J. Neurotrauma*, vol. 32, no. 23, p. 1834, Dec. 2015, doi: 10.1089/NEU.2014.3352.
- [61] P. J. Hutchinson *et al.*, "Inflammation in Human Brain Injury: Intracerebral Concentrations of IL-1 α , IL-1 β , and Their Endogenous Inhibitor IL-1ra," <https://home.liebertpub.com/neu>, vol. 24, no. 10, pp. 1545–1557, Oct. 2007, doi: 10.1089/NEU.2007.0295.
- [62] Z. Shakkour *et al.*, "Drug Repurposing in Neurological Disorders: Implications for Neurotherapy in Traumatic Brain Injury," <https://doi.org/10.1177/1073858420961078>, vol. 27, no. 6, pp. 620–649, Oct. 2020, doi: 10.1177/1073858420961078.
- [63] Y. Morofuji and S. Nakagawa, "Drug Development for Central Nervous System Diseases Using In vitro Blood-brain Barrier Models and Drug Repositioning," *Curr. Pharm. Des.*, vol. 26, no. 13, pp. 1466–1485, Feb. 2020, doi: 10.2174/1381612826666200224112534.
- [64] M. K. Ghiam, S. D. Patel, A. Hoffer, W. R. Selman, B. J. Hoffer, and M. E. Hoffer, "Drug Repurposing in the Treatment of Traumatic Brain Injury," *Front. Neurosci.*, vol. 15, Mar. 2021, doi: 10.3389/FNINS.2021.635483.

- [65] A. Bhat *et al.*, “Phosphodiesterase-4 enzyme as a therapeutic target in neurological disorders,” *Pharmacol. Res.*, vol. 160, p. 105078, Oct. 2020, doi: 10.1016/J.PHRS.2020.105078.
- [66] N. Garrido-Mesa, A. Zarzuelo, and J. Gálvez, “Minocycline: far beyond an antibiotic,” *Br. J. Pharmacol.*, vol. 169, no. 2, pp. 337–352, May 2013, doi: 10.1111/BPH.12139.
- [67] K. M. Buller, M. L. Carty, H. E. Reinebrant, and J. A. Wixey, “Minocycline: A neuroprotective agent for hypoxic-ischemic brain injury in the neonate?,” *J. Neurosci. Res.*, vol. 87, no. 3, pp. 599–608, Feb. 2009, doi: 10.1002/JNR.21890.
- [68] H. S. Kim and Y. H. Suh, “Minocycline and neurodegenerative diseases,” *Behav. Brain Res.*, vol. 196, no. 2, pp. 168–179, Jan. 2009, doi: 10.1016/J.BBR.2008.09.040.
- [69] F. Yang, L. Zhou, D. Wang, Z. Wang, and Q. Y. Huang, “Minocycline ameliorates hypoxia-induced blood-brain barrier damage by inhibition of HIF-1 α through SIRT-3/PHD-2 degradation pathway.,” *Neuroscience*, vol. 304, pp. 250–259, Jul. 2015, doi: 10.1016/J.NEUROSCIENCE.2015.07.051.
- [70] J. Hroudová, “Intracellular signalling pathways and mood disorders,” *Folia Biol. (Praha)*, Jan. 2010, Accessed: Nov. 02, 2022. [Online]. Available: https://www.academia.edu/55065078/Intracellular_signalling_pathways_and_mood_disorders.
- [71] S. Cardarelli, M. Giorgi, G. Poiana, S. Biagioni, and M. Saliola, “Metabolic role of cGMP in *S. cerevisiae*: the murine phosphodiesterase-5 activity affects yeast cell proliferation by altering the cAMP/cGMP equilibrium,” *FEMS Yeast Res.*, vol. 19, no. 3, May 2019, doi: 10.1093/FEMSYR/FOZ016.
- [72] M. P. Kelly and N. J. Brandon, “Differential function of phosphodiesterase families in the brain: gaining insights through the use of genetically modified animals,” *Prog. Brain Res.*, vol. 179, no. C, pp. 67–73, Jan. 2009, doi: 10.1016/S0079-6123(09)17908-6.
- [73] A. J. Tibbo and G. S. Baillie, “Phosphodiesterase 4B: Master Regulator of Brain Signaling,” *Cells*, vol. 9, no. 5, p. 1254, May 2020, doi: 10.3390/CELLS9051254.
- [74] D. J. Titus, A. A. Oliva, N. M. Wilson, and C. M. Atkins, “Phosphodiesterase Inhibitors as Therapeutics for Traumatic Brain Injury.”
- [75] J. Zhu, E. Mix, and B. Winblad, “The Antidepressant and Antiinflammatory Effects of Rolipram in the Central Nervous System,” *CNS Drug Rev.*, vol. 7, no. 4, pp. 387–398, Dec. 2001, doi: 10.1111/J.1527-3458.2001.TB00206.X.

- [76] P. J. Bergold, "Treatment of traumatic brain injury with anti-inflammatory drugs," *Exp. Neurol.*, vol. 275 Pt 3, no. Pt 3, pp. 367–380, Jan. 2016, doi: 10.1016/J.EXPNEUROL.2015.05.024.
- [77] W. A. Banks, "Peptides and the blood–brain barrier," *Peptides*, vol. 72, pp. 16–19, Oct. 2015, doi: 10.1016/J.PEPTIDES.2015.03.010.
- [78] T. S. Salameh and W. A. Banks, "Delivery of Therapeutic Peptides and Proteins to the CNS," *Adv. Pharmacol.*, vol. 71, p. 277, 2014, doi: 10.1016/BS.APHA.2014.06.004.
- [79] A. Ermisch, H. J. Ruhle, R. Landgraf, and J. Hess, "Blood—Brain Barrier and Peptides," <http://dx.doi.org/10.1038/jcbfm.1985.49>, vol. 5, no. 3, pp. 350–357, Jun. 2016, doi: 10.1038/JCBFM.1985.49.
- [80] R. JP, P. N, D. MA, P. S, and M. TA, "Efficient LRP1-Mediated Uptake and Low Cytotoxicity of Peptide L57 In Vitro Shows Its Promise as CNS Drug Delivery Vector," *J. Pharm. Sci.*, vol. 110, no. 2, pp. 824–832, Feb. 2021, doi: 10.1016/J.XPHS.2020.09.019.
- [81] S. E. Storck, M. Kurtyka, and C. U. Pietrzik, "Brain endothelial LRP1 maintains blood–brain barrier integrity," *Fluids Barriers CNS*, vol. 18, no. 1, pp. 1–7, Dec. 2021, doi: 10.1186/S12987-021-00260-5/FIGURES/4.
- [82] S. E. Storck and C. U. Pietrzik, "Endothelial LRP1 – A Potential Target for the Treatment of Alzheimer's Disease," *Pharm. Res. 2017 3412*, vol. 34, no. 12, pp. 2637–2651, Sep. 2017, doi: 10.1007/S11095-017-2267-3.
- [83] K. Sakamoto, T. Shinohara, Y. Adachi, T. Asami, and T. Ohtaki, "A novel LRP1-binding peptide L57 that crosses the blood brain barrier," *Biochem. Biophys. Reports*, vol. 12, pp. 135–139, Dec. 2017, doi: 10.1016/J.BBREP.2017.07.003.
- [84] R. Gabathuler, "Approaches to transport therapeutic drugs across the blood–brain barrier to treat brain diseases," *Neurobiol. Dis.*, vol. 37, no. 1, pp. 48–57, Jan. 2010, doi: 10.1016/J.NBD.2009.07.028.
- [85] S. Satish, M. Tharmavaram, and D. Rawtani, "Haloysite nanotubes as a nature's boon for biomedical applications," *Nanobiomedicine*, vol. 6, Jan. 2019, doi: 10.1177/1849543519863625.
- [86] M. Y. Saleh, N. Prajapati, M. A. DeCoster, and Y. Lvov, "Tagged Haloysite Nanotubes as a Carrier for Intercellular Delivery in Brain Microvascular Endothelium," *Front. Bioeng. Biotechnol.*, vol. 8, p. 451, May 2020, doi: 10.3389/FBIOE.2020.00451/BIBTEX.
- [87] Y. Luo *et al.*, "Cellular Analysis and Chemotherapeutic Potential of a Bi-Functionalized Haloysite Nanotube," *Pharmaceutics*, vol. 12, no. 10, pp. 1–15, Oct. 2020, doi: 10.3390/PHARMACEUTICS12100962.

- [88] B. Wu, M. Jiang, X. Liu, C. Huang, Z. Gu, and Y. Cao, "Evaluation of toxicity of halloysite nanotubes and multi-walled carbon nanotubes to endothelial cells in vitro and blood vessels in vivo," *Nanotoxicology*, vol. 14, no. 8, pp. 1017–1038, Sep. 2020, doi: 10.1080/17435390.2020.1780642.
- [89] C. Macks, S. J. Gwak, M. Lynn, and J. S. Lee, "Rolipram-Loaded Polymeric Micelle Nanoparticle Reduces Secondary Injury after Rat Compression Spinal Cord Injury," *J. Neurotrauma*, vol. 35, no. 3, pp. 582–592, Feb. 2018, doi: 10.1089/NEU.2017.5092.
- [90] V. E. Johnson, D. F. Meaney, D. K. cullen, and D. H. Smith, "Animal models of traumatic brain injury," *Handb. Clin. Neurol.*, vol. 127, pp. 115–128, Jan. 2015, doi: 10.1016/B978-0-444-52892-6.00008-8.
- [91] J. Soueid, "Techniques and Methods of Animal Brain Surgery: Perfusion, Brain Removal, and Histological Techniques," *Front. Neuroengineering Ser.*, Jan. 2015, Accessed: Nov. 02, 2022. [Online]. Available: https://www.academia.edu/25577184/Techniques_and_Methods_of_Animal_Brain_Surgery_Perfusion_Brain_Removal_and_Histological_Techniques.
- [92] I. Cernak, "Animal Models of Head Trauma," *NeuroRX*, vol. 2, no. 3, pp. 410–422, Jul. 2005, doi: 10.1602/NEURORX.2.3.410.
- [93] C. D. Pernici, R. K. Rowe, P. T. Doughty, M. Madadi, J. Lifshitz, and T. A. Murray, "Longitudinal optical imaging technique to visualize progressive axonal damage after brain injury in mice reveals responses to different minocycline treatments," *Sci. Reports 2020 101*, vol. 10, no. 1, pp. 1–16, May 2020, doi: 10.1038/s41598-020-64783-x.
- [94] C. Piao, H. R. Ranaivo, A. Rusie, N. Wadhvani, S. Koh, and M. S. Wainwright, "Thrombin decreases expression of the glutamate transporter GLAST and inhibits glutamate uptake in primary cortical astrocytes via the Rho kinase pathway," *Exp. Neurol.*, vol. 273, pp. 288–300, Nov. 2015, doi: 10.1016/J.EXPNEUROL.2015.09.009.
- [95] P. C. Christensen, Z. Samadi-Bahrami, V. Pavlov, P. K. Stys, and G. R. W. Moore, "Ionotropic glutamate receptor expression in human white matter," *Neurosci. Lett.*, vol. 630, pp. 1–8, Sep. 2016, doi: 10.1016/J.NEULET.2016.07.030.
- [96] L.-L. Zou, J.-L. Ma, T. Wang, T.-B. Yang, and C.-B. Liu, "Cell-Penetrating Peptide-Mediated Therapeutic Molecule Delivery into the Central Nervous System."
- [97] E. S. Khafagy, N. Kamei, E. J. B. Nielsen, R. Nishio, and M. Takeda-Morishita, "One-month subchronic toxicity study of cell-penetrating peptides for insulin nasal delivery in rats," *Eur. J. Pharm. Biopharm.*, vol. 85, no. 3, pp. 736–743, Nov. 2013, doi: 10.1016/J.EJPB.2013.09.014.

- [98] Z. He *et al.*, “An anti-inflammatory peptide and brain-derived neurotrophic factor-modified hyaluronan-methylcellulose hydrogel promotes nerve regeneration in rats with spinal cord injury,” *Int. J. Nanomedicine*, vol. 14, p. 721, 2019, doi: 10.2147/IJN.S187854.
- [99] G. Morris, “Purification and Uptake Studies of Recombinant Human N- α -D-Acetylglucosaminidase from Sf9 Insect Cells,” *Grad. Cert. Learn. Teach. High. Educ.*, 2015, Accessed: Nov. 02, 2022. [Online]. Available: <https://dspace.library.uvic.ca/handle/1828/6583>.
- [100] Y. Fan, C. R. Evans, and J. Ling, “Rewiring Protein Synthesis: From Natural to Synthetic Amino Acids,” *Biochim. Biophys. Acta*, vol. 1861, no. 11 Pt B, p. 3024, Nov. 2017, doi: 10.1016/J.BBAGEN.2017.01.014.
- [101] V. Apostolopoulos *et al.*, “A Global Review on Short Peptides: Frontiers and Perspectives,” *Molecules*, vol. 26, no. 2, Jan. 2021, doi: 10.3390/MOLECULES26020430.
- [102] L. Malavolta and F. R. Cabral, “Peptides: important tools for the treatment of central nervous system disorders,” *Neuropeptides*, vol. 45, no. 5, pp. 309–316, Oct. 2011, doi: 10.1016/J.NPEP.2011.03.001.
- [103] K. Jahnke, H. Grubmüller, M. Igaev, and K. Göpfrich, “Choice of fluorophore affects dynamic DNA nanostructures,” *Nucleic Acids Res.*, vol. 49, no. 7, pp. 4186–4195, Apr. 2021, doi: 10.1093/NAR/GKAB201.
- [104] R. Fischer, T. Waizenegger, K. Köhler, and R. Brock, “A quantitative validation of fluorophore-labelled cell-permeable peptide conjugates: fluorophore and cargo dependence of import,” *Biochim. Biophys. Acta - Biomembr.*, vol. 1564, no. 2, pp. 365–374, Aug. 2002, doi: 10.1016/S0005-2736(02)00471-6.
- [105] L. M. Jungbauer, C. Yu, K. J. Laxton, and M. J. LaDu, “Preparation of fluorescently-labeled amyloid-beta peptide assemblies: the effect of fluorophore conjugation on structure and function,” *J. Mol. Recognit.*, vol. 22, no. 5, pp. 403–413, Sep. 2009, doi: 10.1002/JMR.948.
- [106] R. Behrendt, P. White, and J. Offer, “Advances in Fmoc solid-phase peptide synthesis,” *J. Pept. Sci.*, vol. 22, no. 1, pp. 4–27, Jan. 2016, doi: 10.1002/PSC.2836.
- [107] M. Amblard, J. A. Fehrentz, J. Martinez, and G. Subra, “Methods and protocols of modern solid phase peptide synthesis,” *Mol. Biotechnol.*, vol. 33, no. 3, pp. 239–254, Jul. 2006, doi: 10.1385/MB:33:3:239.
- [108] W. Li, N. M. O’Brien-Simpson, M. A. Hossain, and J. D. Wade, “The 9-Fluorenylmethoxycarbonyl (Fmoc) Group in Chemical Peptide Synthesis – Its Past, Present, and Future,” *undefined*, vol. 73, no. 4, pp. 271–276, Apr. 2020, doi: 10.1071/CH19427.

- [109] F. Albericio and L. A. Carpino, "Coupling reagents and activation," *Methods Enzymol.*, vol. 289, pp. 104–126, 1997, doi: 10.1016/S0076-6879(97)89046-5.
- [110] G. B. FIELDS and R. L. NOBLE, "Solid phase peptide synthesis utilizing 9-fluorenylmethoxycarbonyl amino acids," *Int. J. Pept. Protein Res.*, vol. 35, no. 3, pp. 161–214, 1990, doi: 10.1111/J.1399-3011.1990.TB00939.X.
- [111] T. G. Ma, Y. H. Ling, G. D. McClure, and M. T. Tseng, "Effects of trifluoroacetic acid, a halothane metabolite, on C6 glioma cells," *J. Toxicol. Environ. Health*, vol. 31, no. 2, pp. 147–158, Jan. 1990, doi: 10.1080/15287399009531444.
- [112] J. Cornish *et al.*, "Trifluoroacetate, a contaminant in purified proteins, inhibits proliferation of osteoblasts and chondrocytes," *Am. J. Physiol.*, vol. 277, no. 5, 1999, doi: 10.1152/AJPENDO.1999.277.5.E779.
- [113] S. Roux, E. Zékri, B. Rousseau, J. C. Cintrat, and N. Fay, "Elimination and exchange of trifluoroacetate counter-ion from cationic peptides: a critical evaluation of different approaches," *J. Pept. Sci.*, vol. 14, no. 3, pp. 354–359, Mar. 2008, doi: 10.1002/PSC.951.
- [114] C. A. Puckett and J. K. Barton, "Targeting a ruthenium complex to the nucleus with short peptides," *Bioorg. Med. Chem.*, vol. 18, no. 10, pp. 3564–3569, May 2010, doi: 10.1016/J.BMC.2010.03.081.
- [115] L. C. Wu, F. Chen, S. L. Lee, A. Raw, and L. X. Yu, "Building parity between brand and generic peptide products: Regulatory and scientific considerations for quality of synthetic peptides," *Int. J. Pharm.*, vol. 518, no. 1–2, pp. 320–334, Feb. 2017, doi: 10.1016/J.IJPHARM.2016.12.051.
- [116] A. Muheem *et al.*, "A review on the strategies for oral delivery of proteins and peptides and their clinical perspectives," *Saudi Pharm. J.*, vol. 24, no. 4, pp. 413–428, Jul. 2016, doi: 10.1016/J.JSPS.2014.06.004.
- [117] A. Shahidian, H. Afshar, M. R. Habibi, and M. Ghassemi, "Therapeutic Nanostructures: Application of Mechanical Engineering in Drug Delivery," *Nanoarchitectonics Smart Deliv. Drug Target.*, pp. 3–34, Jan. 2016, doi: 10.1016/B978-0-323-47347-7.00001-X.
- [118] X. Dong, "Current Strategies for Brain Drug Delivery," *Theranostics*, vol. 8, no. 6, p. 1481, 2018, doi: 10.7150/THNO.21254.
- [119] L. Serwer, R. Hashizume, T. Ozawa, and C. David James, "Systemic and local drug delivery for treating diseases of the central nervous system in rodent models," *J. Vis. Exp.*, no. 42, 2010, doi: 10.3791/1992.

- [120] Y. T. Kuo, A. H. Herlihy, P. W. So, K. K. Bhakoo, and J. D. Bell, "In vivo measurements of T1 relaxation times in mouse brain associated with different modes of systemic administration of manganese chloride," *J. Magn. Reson. Imaging*, vol. 21, no. 4, pp. 334–339, Apr. 2005, doi: 10.1002/JMRI.20285.
- [121] F. Erdő, L. A. Bors, D. Farkas, Á. Bajza, and S. Gizurarson, "Evaluation of intranasal delivery route of drug administration for brain targeting," *Brain Res. Bull.*, vol. 143, pp. 155–170, Oct. 2018, doi: 10.1016/J.BRAINRESBULL.2018.10.009.
- [122] J. Bolcaen *et al.*, "A perspective on the radiopharmaceutical requirements for imaging and therapy of glioblastoma," *Theranostics*, vol. 11, no. 16, pp. 7911–7947, 2021, doi: 10.7150/THNO.56639.
- [123] A. Al Shoyaib, S. R. Archie, and V. T. Karamyan, "Intraperitoneal Route of Drug Administration: Should it Be Used in Experimental Animal Studies?," *Pharm. Res.*, vol. 37, no. 1, pp. 1–17, Jan. 2020, doi: 10.1007/S11095-019-2745-X/TABLES/5.
- [124] J. McMasters, S. Poh, J. B. Lin, and A. Panitch, "Delivery of anti-inflammatory peptides from hollow PEGylated poly(NIPAM) nanoparticles reduces inflammation in an ex vivo osteoarthritis model," *J. Control. Release*, vol. 258, pp. 161–170, Jul. 2017, doi: 10.1016/J.JCONREL.2017.05.008.
- [125] R. U. Agu, M. I. Ugwoke, M. Armand, R. Kinget, and N. Verbeke, "The lung as a route for systemic delivery of therapeutic proteins and peptides," *Respir. Res.*, vol. 2, no. 4, pp. 198–209, Apr. 2001, doi: 10.1186/RR58/TABLES/1.
- [126] Jitendra, P. K. Sharma, S. Bansal, and A. Banik, "Noninvasive Routes of Proteins and Peptides Drug Delivery," *Indian J. Pharm. Sci.*, vol. 73, no. 4, p. 367, Jul. 2011, doi: 10.4103/0250-474X.95608.
- [127] G. Tosi *et al.*, "Brain-targeted polymeric nanoparticles: in vivo evidence of different routes of administration in rodents," <https://doi.org/10.2217/nnm.12.172>, vol. 8, no. 9, pp. 1373–1383, Aug. 2013, doi: 10.2217/NNM.12.172.
- [128] A. Fortuna, G. Alves, A. Serralheiro, J. Sousa, and A. Falcão, "Intranasal delivery of systemic-acting drugs: small-molecules and biomacromolecules," *Eur. J. Pharm. Biopharm.*, vol. 88, no. 1, pp. 8–27, Sep. 2014, doi: 10.1016/J.EJPB.2014.03.004.
- [129] E. T. Maggio, "Intravail: highly effective intranasal delivery of peptide and protein drugs," *Expert Opin. Drug Deliv.*, vol. 3, no. 4, pp. 529–539, Jul. 2006, doi: 10.1517/17425247.3.4.529.
- [130] C. Xiao *et al.*, "Brain transit and ameliorative effects of intranasally delivered anti-amyloid- β oligomer antibody in 5XFAD mice," *J. Alzheimers. Dis.*, vol. 35, no. 4, pp. 777–788, 2013, doi: 10.3233/JAD-122419.

- [131] A. R. Clementino *et al.*, “Structure and Fate of Nanoparticles Designed for the Nasal Delivery of Poorly Soluble Drugs,” *Mol. Pharm.*, vol. 18, no. 8, pp. 3132–3146, Aug. 2021, doi: 10.1021/ACS.MOLPHARMACEUT.1C00366/ASSET/IMAGES/LARGE/MP1C00366_0008.JPEG.
- [132] P. V Turner, T. Brabb, C. Pekow, and M. A. Vasbinder, “Administration of Substances to Laboratory Animals: Routes of Administration and Factors to Consider.”
- [133] S. V. Dhuria, L. R. Hanson, and W. H. Frey, “Intranasal delivery to the central nervous system: mechanisms and experimental considerations,” *J. Pharm. Sci.*, vol. 99, no. 4, pp. 1654–1673, 2010, doi: 10.1002/JPS.21924.
- [134] A. A. Hussain, “Intranasal drug delivery,” *Adv. Drug Deliv. Rev.*, vol. 29, no. 1–2, pp. 39–49, Jan. 1998, doi: 10.1016/S0169-409X(97)00060-4.
- [135] M. O. Freire and T. E. Van Dyke, “Natural resolution of inflammation,” *Periodontol. 2000*, vol. 63, no. 1, pp. 149–164, Oct. 2013, doi: 10.1111/PRD.12034.
- [136] O. J. Broom, B. Widjaya, J. Troelsen, J. Olsen, and O. H. Nielsen, “Mitogen activated protein kinases: A role in inflammatory bowel disease?,” *Clin. Exp. Immunol.*, vol. 158, no. 3, pp. 272–280, Dec. 2009, doi: 10.1111/J.1365-2249.2009.04033.X.
- [137] S. Soni, P. Anand, and Y. S. Padwad, “MAPKAPK2: the master regulator of RNA-binding proteins modulates transcript stability and tumor progression,” *J. Exp. Clin. Cancer Res.*, vol. 38, no. 1, pp. 121–121, Mar. 2019, doi: 10.1186/S13046-019-1115-1.
- [138] A. Borrelli, A. L. Tornesello, M. L. Tornesello, and F. M. Buonaguro, “Cell Penetrating Peptides as Molecular Carriers for Anti-Cancer Agents,” *undefined*, vol. 23, no. 2, 2018, doi: 10.3390/MOLECULES23020295.
- [139] K. Hayess and R. Benndorf, “Effect of protein kinase inhibitors on activity of mammalian small heat- shock protein (HSP25) Kinase,” *Biochem. Pharmacol.*, vol. 53, no. 9, pp. 1239–1247, May 1997, doi: 10.1016/S0006-2952(96)00877-5.
- [140] A. Kotlyarov *et al.*, “MAPKAP kinase 2 is essential for LPS-induced TNF-alpha biosynthesis,” *Nat. Cell Biol.*, vol. 1, no. 2, pp. 94–97, 1999, doi: 10.1038/10061.
- [141] E. Carballo, W. S. Lai, and P. J. Blakeshear, “Feedback Inhibition of Macrophage Tumor Necrosis Factor- α Production by Tristetraprolin,” *undefined*, vol. 281, no. 5379, pp. 1001–1005, Aug. 1998, doi: 10.1126/SCIENCE.281.5379.1001.

- [142] R. Winzen *et al.*, “Functional Analysis of KSRP Interaction with the AU-Rich Element of Interleukin-8 and Identification of Inflammatory mRNA Targets,” *undefined*, vol. 27, no. 23, pp. 8388–8400, Dec. 2007, doi: 10.1128/MCB.01493-07.
- [143] R. K. Kheder, J. Hobkirk, and C. M. Stover, “In vitro modulation of the LPS-induced proinflammatory profile of hepatocytes and macrophages—approaches for intervention in obesity?,” *Front. Cell Dev. Biol.*, vol. 4, no. JUN, Jun. 2016, doi: 10.3389/FCELL.2016.00061/PDF.
- [144] H. Raza, A. John, and J. Shafarin, “Potentiation of LPS-Induced Apoptotic Cell Death in Human Hepatoma HepG2 Cells by Aspirin via ROS and Mitochondrial Dysfunction: Protection by N-Acetyl Cysteine,” *PLoS One*, vol. 11, no. 7, p. e0159750, Jul. 2016, doi: 10.1371/JOURNAL.PONE.0159750.
- [145] M. C. Gutiérrez-Ruiz *et al.*, “Cytokines, growth factors, and oxidative stress in HepG2 cells treated with ethanol, acetaldehyde, and LPS,” *Toxicology*, vol. 134, no. 2–3, pp. 197–207, Jun. 1999, doi: 10.1016/S0300-483X(99)00044-X.
- [146] S. M. Lucas, N. J. Rothwell, and R. M. Gibson, “The role of inflammation in CNS injury and disease,” *Br. J. Pharmacol.*, vol. 147 Suppl 1, no. Suppl 1, Jan. 2006, doi: 10.1038/SJ.BJP.0706400.
- [147] R. L. Bartlett, S. Sharma, and A. Panitch, “Cell-penetrating peptides released from thermosensitive nanoparticles suppress pro-inflammatory cytokine response by specifically targeting inflamed cartilage explants,” *Nanomedicine Nanotechnology, Biol. Med.*, vol. 9, no. 3, pp. 419–427, Apr. 2013, doi: 10.1016/J.NANO.2012.09.003.
- [148] J. McMasters and A. Panitch, “Collagen-binding nanoparticles for extracellular anti-inflammatory peptide delivery decrease platelet activation, promote endothelial migration, and suppress inflammation,” *Acta Biomater.*, vol. 49, pp. 78–88, Feb. 2017, doi: 10.1016/J.ACTBIO.2016.11.023.
- [149] S. S *et al.*, “Cell-Penetrating Peptides Selectively Cross the Blood-Brain Barrier In Vivo,” *PLoS One*, vol. 10, no. 10, Oct. 2015, doi: 10.1371/JOURNAL.PONE.0139652.
- [150] T. Yin, W. Xie, J. Sun, L. Yang, and J. Liu, “Penetratin Peptide-Functionalized Gold Nanostars: Enhanced BBB Permeability and NIR Photothermal Treatment of Alzheimer’s Disease Using Ultralow Irradiance,” *ACS Appl. Mater. Interfaces*, vol. 8, no. 30, pp. 19291–19302, Aug. 2016, doi: 10.1021/ACSAMI.6B05089.
- [151] P. Frøslev, H. Franzyk, B. Ozgür, B. Brodin, and M. Kristensen, “Highly cationic cell-penetrating peptides affect the barrier integrity and facilitates mannitol permeation in a human stem cell-based blood-brain barrier model,” *Eur. J. Pharm. Sci.*, vol. 168, p. 106054, Jan. 2022, doi: 10.1016/J.EJPS.2021.106054.

- [152] A. Komin, L. M. Russell, K. A. Hristova, and P. C. Searson, "Peptide-based strategies for enhanced cell uptake, transcellular transport, and circulation: Mechanisms and challenges," *Adv. Drug Deliv. Rev.*, vol. 110–111, pp. 52–64, Feb. 2017, doi: 10.1016/J.ADDR.2016.06.002.
- [153] P. McGonigle, "Peptide therapeutics for CNS indications," *Biochem. Pharmacol.*, vol. 83, no. 5, pp. 559–566, Mar. 2012, doi: 10.1016/J.BCP.2011.10.014.
- [154] H. C. Helms *et al.*, "In vitro models of the blood-brain barrier: An overview of commonly used brain endothelial cell culture models and guidelines for their use," *J. Cereb. Blood Flow Metab.*, vol. 36, no. 5, pp. 862–890, Feb. 2015, doi: 10.1177/0271678X16630991/ASSET/IMAGES/LARGE/10.1177_0271678X16630991-FIG2.JPEG.
- [155] I. Puscas *et al.*, "IVIVC Assessment of Two Mouse Brain Endothelial Cell Models for Drug Screening," *Pharmaceutics*, vol. 11, no. 11, pp. E587–E587, Nov. 2019, doi: 10.3390/PHARMACEUTICS11110587.
- [156] O. Steiner, C. Coisne, B. Engelhardt, and R. Lyck, "Comparison of Immortalized bEnd5 and Primary Mouse Brain Microvascular Endothelial Cells as in vitro Blood–Brain Barrier Models for the Study of T Cell Extravasation," *undefined*, vol. 31, no. 1, pp. 315–327, Jan. 2011, doi: 10.1038/JCBFM.2010.96.
- [157] S. Veszelka *et al.*, "Comparison of a rat primary cell-based blood-brain barrier model with epithelial and brain endothelial cell lines: Gene expression and drug transport," *Front. Mol. Neurosci.*, vol. 11, p. 166, May 2018, doi: 10.3389/FNMOL.2018.00166/BIBTEX.
- [158] M. Shibata *et al.*, "Clearance of Alzheimer's amyloid-ss(1-40) peptide from brain by LDL receptor-related protein-1 at the blood-brain barrier," *J. Clin. Invest.*, vol. 106, no. 12, pp. 1489–1499, 2000, doi: 10.1172/JCI10498.
- [159] J. L. Scoggin *et al.*, "An enzyme-based electrochemical biosensor probe with sensitivity to detect astrocytic versus glioma uptake of glutamate in real time in vitro," *Biosens. Bioelectron.*, vol. 126, pp. 751–757, Feb. 2019, doi: 10.1016/J.BIOS.2018.11.023.
- [160] N. Karekar *et al.*, "Self-Assembled Metal-Organic Biohybrids (MOBs) Using Copper and Silver for Cell Studies," *Nanomater. (Basel, Switzerland)*, vol. 9, no. 9, Sep. 2019, doi: 10.3390/NANO9091282.
- [161] N. J. Abbott, C. C. W. Hughes, P. A. Revest, and J. Greenwood, "Development and characterisation of a rat brain capillary endothelial culture: towards an in vitro blood-brain barrier," *J. Cell Sci.*, vol. 103 (Pt 1), no. 1, pp. 23–37, 1992, doi: 10.1242/JCS.103.1.23.

- [162] Z. S. Al-Ahmady, "Selective drug delivery approaches to lesioned brain through blood brain barrier disruption," <https://doi.org/10.1080/17425247.2018.1444601>, vol. 15, no. 4, pp. 335–349, Apr. 2018, doi: 10.1080/17425247.2018.1444601.
- [163] T. Li *et al.*, "Intra-articular injection of anti-inflammatory peptide-loaded glycol chitosan/fucoidan nanogels to inhibit inflammation and attenuate osteoarthritis progression," *Int. J. Biol. Macromol.*, vol. 170, pp. 469–478, Feb. 2021, doi: 10.1016/J.IJBIOMAC.2020.12.158.
- [164] Ü. Langel, "Therapeutic Potential of CPPs," *CPP, Cell-Penetrating Pept.*, pp. 409–461, 2019, doi: 10.1007/978-981-13-8747-0_12.
- [165] P. Kim *et al.*, "Cell-Penetrating MK2 Inhibitory Peptide Blocks LPS-Induced Expression of Proinflammatory Cytokines in HepG2 Hepatocytes," *FASEB J.*, vol. 34, no. S1, pp. 1–1, Apr. 2020, doi: 10.1096/FASEBJ.2020.34.S1.09121.
- [166] T. Holm, S. E. L. Andaloussi, and U. Langel, "Comparison of CPP uptake methods.," *Methods Mol. Biol.*, vol. 683, pp. 207–217, 2011, doi: 10.1007/978-1-60761-919-2_15/COVER.
- [167] X. A. Álvarez, J. Figueroa, and D. Muresanu, "Peptidergic drugs for the treatment of traumatic brain injury," <http://dx.doi.org/10.2217/fnl.12.95>, vol. 8, no. 2, pp. 175–192, Feb. 2013, doi: 10.2217/FNL.12.95.
- [168] O. Tenovuo, R. Diaz-Arrastia, L. E. Goldstein, D. J. Sharp, J. van der Naalt, and N. D. Zasler, "Assessing the Severity of Traumatic Brain Injury-Time for a Change?," *J. Clin. Med.*, vol. 10, no. 1, pp. 1–12, Jan. 2021, doi: 10.3390/JCM10010148.
- [169] W. Heegaard and M. Biros, "Traumatic Brain Injury," *Emerg. Med. Clin. North Am.*, vol. 25, no. 3, pp. 655–678, Aug. 2007, doi: 10.1016/J.EMC.2007.07.001.
- [170] A. Hammad, L. Westacott, and M. Zaben, "The role of the complement system in traumatic brain injury: a review," *J. Neuroinflammation 2018 151*, vol. 15, no. 1, pp. 1–15, Jan. 2018, doi: 10.1186/S12974-018-1066-Z.
- [171] M. V. Russo and D. B. McGavern, "Inflammatory neuroprotection following traumatic brain injury," *Science*, vol. 353, no. 6301, p. 783, Aug. 2016, doi: 10.1126/SCIENCE.AAF6260.
- [172] K. Dohi *et al.*, "Gp91phox(NOX2) in classically activated microglia exacerbates traumatic brain injury," *J. Neuroinflammation*, vol. 7, no. 1, pp. 1–11, Jul. 2010, doi: 10.1186/1742-2094-7-41/FIGURES/6.
- [173] C. Pernici, "Development of a Longitudinal Imaging System for Murine Brain Injury Models," *Dr. Diss.*, Aug. 2018, Accessed: Oct. 21, 2021. [Online]. Available: <https://digitalcommons.latech.edu/dissertations/20>.

- [174] S. Homsí *et al.*, “Minocycline effects on cerebral edema: relations with inflammatory and oxidative stress markers following traumatic brain injury in mice,” *Brain Res.*, vol. 1291, pp. 122–132, Sep. 2009, doi: 10.1016/J.BRAINRES.2009.07.031.
- [175] S. Homsí *et al.*, “Blockade of acute microglial activation by minocycline promotes neuroprotection and reduces locomotor hyperactivity after closed head injury in mice: a twelve-week follow-up study,” *J. Neurotrauma*, vol. 27, no. 5, pp. 911–921, May 2010, doi: 10.1089/NEU.2009.1223.
- [176] N. Lou, T. Takano, Y. Pei, A. L. Xavier, S. A. Goldman, and M. Nedergaard, “Purinergic receptor P2RY12-dependent microglial closure of the injured blood-brain barrier,” *Proc. Natl. Acad. Sci. U. S. A.*, vol. 113, no. 4, pp. 1074–1079, Jan. 2016, doi: 10.1073/PNAS.1520398113/-/DCSUPPLEMENTAL.
- [177] Y. Zhou, R. Fan, B. O. A. Botchway, Y. Zhang, and X. Liu, “Infliximab Can Improve Traumatic Brain Injury by Suppressing the Tumor Necrosis Factor Alpha Pathway,” *Mol. Neurobiol.* 2021 586, vol. 58, no. 6, pp. 2803–2811, Jan. 2021, doi: 10.1007/S12035-021-02293-1.
- [178] K. N. Corps, T. L. Roth, and D. B. McGavern, “Inflammation and neuroprotection in traumatic brain injury,” *JAMA Neurol.*, vol. 72, no. 3, pp. 355–362, Mar. 2015, doi: 10.1001/JAMANEUROL.2014.3558.
- [179] J. H. Jiang *et al.*, “Intranasal MMI-0100 Attenuates A β 1–42- and LPS-Induced Neuroinflammation and Memory Impairments via the MK2 Signaling Pathway,” *Front. Immunol.*, vol. 10, p. 2707, Nov. 2019, doi: 10.3389/FIMMU.2019.02707/BIBTEX.
- [180] X. Wang, L. Xu, H. Wang, P. R. Young, M. Gaestel, and G. Z. Feuerstein, “Mitogen-activated protein kinase-activated protein (MAPKAP) kinase 2 deficiency protects brain from ischemic injury in mice,” *J. Biol. Chem.*, vol. 277, no. 46, pp. 43968–43972, Nov. 2002, doi: 10.1074/jbc.M206837200.
- [181] T. Obata, G. E. Brown, and M. B. Yaffe, “MAP kinase pathways activated by stress: the p38 MAPK pathway,” *Crit. Care Med.*, vol. 28, no. 4 Suppl, 2000, doi: 10.1097/00003246-200004001-00008.
- [182] E. Shohami, I. Ginis, and J. M. Hallenbeck, “Dual role of tumor necrosis factor alpha in brain injury,” *Cytokine Growth Factor Rev.*, vol. 10, no. 2, pp. 119–130, Jun. 1999, doi: 10.1016/S1359-6101(99)00008-8.
- [183] H. Nawashiro, D. Martin, and J. M. Hallenbeck, “Inhibition of tumor necrosis factor and amelioration of brain infarction in mice,” *J. Cereb. Blood Flow Metab.*, vol. 17, no. 2, pp. 229–232, Aug. 1997, doi: 10.1097/00004647-199702000-00013/ASSET/IMAGES/LARGE/10.1097_00004647-199702000-00013-FIG1.JPEG.

- [184] H. Nawashiro, K. Tasaki, C. A. Ruetzler, and J. M. Hallenbeck, "TNF- α pretreatment induces protective effects against focal cerebral ischemia in mice," *J. Cereb. Blood Flow Metab.*, vol. 17, no. 5, pp. 483–490, Aug. 1997, doi: 10.1097/00004647-199705000-00001/ASSET/IMAGES/LARGE/10.1097_00004647-199705000-00001-FIG1.JPEG.
- [185] R. A. Scranton, L. Fletcher, S. Sprague, D. F. Jimenez, and M. Digicaylioglu, "The rostral migratory stream plays a key role in intranasal delivery of drugs into the CNS," *PLoS One*, vol. 6, no. 4, p. e18711, 2011, doi: 10.1371/JOURNAL.PONE.0018711.
- [186] H. Shiotsuki *et al.*, "A rotarod test for evaluation of motor skill learning," *J. Neurosci. Methods*, vol. 189, no. 2, pp. 180–185, Jun. 2010, doi: 10.1016/J.JNEUMETH.2010.03.026.
- [187] R. J. Hamm, B. R. Pike, D. M. O'dell, B. G. Lyeth, and L. W. Jenkins, "The rotarod test: an evaluation of its effectiveness in assessing motor deficits following traumatic brain injury.," *J. Neurotrauma*, vol. 11, no. 2, pp. 187–196, Apr. 1994, doi: 10.1089/NEU.1994.11.187.
- [188] R. E. Nordquist, E. Meijer, F. J. van der Staay, and S. S. Arndt, "Pigs as Model Species to Investigate Effects of Early Life Events on Later Behavioral and Neurological Functions," *Anim. Model. Study Hum. Dis. Second Ed.*, pp. 1003–1030, Jan. 2017, doi: 10.1016/B978-0-12-809468-6.00039-5.
- [189] L. M. Lueptow, "Novel Object Recognition Test for the Investigation of Learning and Memory in Mice," *J. Vis. Exp.*, vol. 2017, no. 126, p. 55718, Aug. 2017, doi: 10.3791/55718.
- [190] C. Sobin and M. Golub, "Behavioral Outcome as a Primary Organizing Principle for Mechanistic Data in Developmental Neurotoxicity," *Handb. Dev. Neurotoxicology*, pp. 337–347, Jan. 2018, doi: 10.1016/B978-0-12-809405-1.00029-8.
- [191] G. J. Gage, D. R. Kipke, and W. Shain, "Whole animal perfusion fixation for rodents," *J. Vis. Exp.*, no. 65, 2012, doi: 10.3791/3564.
- [192] E. J. Ley, M. A. Clond, M. B. Singer, D. Shouhed, and A. Salim, "IL6 Deficiency Affects Function After Traumatic Brain Injury," *J. Surg. Res.*, vol. 170, no. 2, pp. 253–256, Oct. 2011, doi: 10.1016/J.JSS.2011.03.006.
- [193] S. Mashhadizadeh, Y. Farbood, M. Dianat, A. Khodadadi, and A. Sarkaki, "Therapeutic effects of ellagic acid on memory, hippocampus electrophysiology deficits, and elevated TNF- α level in brain due to experimental traumatic brain injury," *Iran. J. Basic Med. Sci.*, vol. 20, no. 4, p. 399, 2017, doi: 10.22038/IJBMS.2017.8581.

- [194] M. L. Formica, D. A. Real, M. L. Picchio, E. Catlin, R. F. Donnelly, and A. J. Paredes, "On a highway to the brain: A review on nose-to-brain drug delivery using nanoparticles," *Appl. Mater. Today*, vol. 29, p. 101631, Dec. 2022, doi: 10.1016/J.APMT.2022.101631.
- [195] F. Persano, S. Batasheva, G. Fakhrullina, G. Gigli, S. Leporatti, and R. Fakhrullin, "Recent advances in the design of inorganic and nano-clay particles for the treatment of brain disorders," *J. Mater. Chem. B*, vol. 9, no. 12, pp. 2756–2784, Apr. 2021, doi: 10.1039/D0TB02957B.
- [196] M. Agrawal *et al.*, "Recent strategies and advances in the fabrication of nano lipid carriers and their application towards brain targeting," *J. Control. Release*, vol. 321, pp. 372–415, May 2020, doi: 10.1016/J.JCONREL.2020.02.020.
- [197] M. Liu, Z. Jia, D. Jia, and C. Zhou, "Recent advance in research on halloysite nanotubes-polymer nanocomposite," *undefined*, vol. 39, no. 8, pp. 1498–1525, 2014, doi: 10.1016/J.PROGPOLYMSCI.2014.04.004.
- [198] Y. Lvov, W. Wang, L. Zhang, and R. Fakhrullin, "Halloysite Clay Nanotubes for Loading and Sustained Release of Functional Compounds," *undefined*, vol. 28, no. 6, pp. 1227–1250, Feb. 2016, doi: 10.1002/ADMA.201502341.
- [199] A. C. Santos, I. Pereira, S. Reis, F. Veiga, M. Saleh, and Y. Lvov, "Biomedical potential of clay nanotube formulations and their toxicity assessment," *undefined*, vol. 16, no. 11, pp. 1169–1182, Nov. 2019, doi: 10.1080/17425247.2019.1665020.
- [200] M. Liu, R. Fakhrullin, A. Novikov, A. Panchal, and Y. Lvov, "Tubule Nanoclay-Organic Heterostructures for Biomedical Applications.," *undefined*, vol. 19, no. 4, Apr. 2019, doi: 10.1002/MABI.201800419.
- [201] V. Vergaro *et al.*, "Cytocompatibility and uptake of halloysite clay nanotubes.," *undefined*, vol. 11, no. 3, pp. 820–826, Mar. 2010, doi: 10.1021/BM9014446.
- [202] M. R. Dзамukova, E. A. Naumenko, E. V. Rozhina, A. A. Trifonov, and R. F. Fakhrullin, "Cell surface engineering with polyelectrolyte-stabilized magnetic nanoparticles: A facile approach for fabrication of artificial multicellular tissue-mimicking clusters," *undefined*, vol. 8, no. 8, pp. 2515–2532, Aug. 2015, doi: 10.1007/S12274-015-0759-1.
- [203] X. Wang, J. Gong, Z. Gui, T. Hu, and X. Xu, "Halloysite nanotubes-induced Al accumulation and oxidative damage in liver of mice after 30-day repeated oral administration," *undefined*, vol. 33, no. 6, pp. 623–630, Jun. 2018, doi: 10.1002/TOX.22543.
- [204] R. F. Kamalievа, I. R. Ishmukhametov, S. N. Batasheva, E. V. Rozhina, and R. F. Fakhrullin, "Uptake of halloysite clay nanotubes by human cells: Colourimetric viability tests and microscopy study," *undefined*, vol. 15, pp. 54–60, Jul. 2018, doi: 10.1016/J.NANOSO.2018.03.009.

- [205] A. M. Yamina, M. Fizir, A. Itatahine, H. He, and P. Dramou, "Preparation of multifunctional PEG-graft-Halloysite Nanotubes for Controlled Drug Release, Tumor Cell Targeting, and Bio-imaging," *undefined*, vol. 170, pp. 322–329, Oct. 2018, doi: 10.1016/J.COLSURFB.2018.06.042.
- [206] G. Fakhrollina, E. Khakimova, F. Akhatova, G. Lazzara, F. Parisi, and R. Fakhrollin, "Selective antimicrobial effects of curcumin@halloysite nanoformulation: a *Caenorhabditis elegans* study.," *undefined*, vol. 11, no. 26, pp. 23050–23064, Jul. 2019, doi: 10.1021/ACSAMI.9B07499.
- [207] X. Zhao *et al.*, "Toxicity Evaluation of One-Dimensional Nanoparticles Using *Caenorhabditis elegans*: A Comparative Study of Halloysite Nanotubes and Chitin Nanocrystals," *undefined*, vol. 7, no. 23, pp. 18965–18975, Dec. 2019, doi: 10.1021/ACSSUSCHEMENG.9B04365.
- [208] J. Yang *et al.*, "Enhanced Therapeutic Efficacy of Doxorubicin for Breast Cancer Using Chitosan Oligosaccharide-Modified Halloysite Nanotubes," *ACS Appl. Mater. Interfaces*, vol. 8, no. 40, pp. 26578–26590, Oct. 2016, doi: 10.1021/ACSAMI.6B09074/SUPPL_FILE/AM6B09074_SI_001.PDF.
- [209] J. Wen, Y. Huang, T. P. Crowe, and W. H. Hsu, "Evaluation of Recent Intranasal Drug Delivery Systems to the Central Nervous System," *Pharm. 2022, Vol. 14, Page 629*, vol. 14, no. 3, p. 629, Mar. 2022, doi: 10.3390/PHARMACEUTICS14030629.
- [210] W. Li *et al.*, "Microfluidic assembly of a nano-in-micro dual drug delivery platform composed of halloysite nanotubes and a pH-responsive polymer for colon cancer therapy," *Acta Biomater.*, vol. 48, pp. 238–246, Jan. 2017, doi: 10.1016/J.ACTBIO.2016.10.042.
- [211] X. Zhang *et al.*, "Poly(l-lactide)/halloysite nanotube electrospun mats as dual-drug delivery systems and their therapeutic efficacy in infected full-thickness burns," <http://dx.doi.org/10.1177/0885328215593837>, vol. 30, no. 5, pp. 512–525, Jul. 2015, doi: 10.1177/0885328215593837.
- [212] C. Lazaridis, C. G. Rusin, and C. S. Robertson, "Secondary brain injury: Predicting and preventing insults," *Neuropharmacology*, vol. 145, no. Pt B, pp. 145–152, Feb. 2019, doi: 10.1016/J.NEUROPHARM.2018.06.005.
- [213] P. Kumar, A. Gupta, and A. Gupta, "Secondary damage in trauma and limited access dressing: a review," *Plast. Aesthetic Res.*, vol. 7, p. 29, Jun. 2020, doi: 10.20517/2347-9264.2019.71.
- [214] K. Adataia, V. F. J. Newcombe, and D. K. Menon, "Contusion Progression Following Traumatic Brain Injury: A Review of Clinical and Radiological Predictors, and Influence on Outcome," *Neurocrit. Care*, vol. 34, no. 1, pp. 312–324, Feb. 2021, doi: 10.1007/S12028-020-00994-4.

- [215] C. M. Atkins, M. L. Cepero, Y. Kang, D. J. Liebl, and W. D. Dietrich, "Effects of early rolipram treatment on histopathological outcome after controlled cortical impact injury in mice," *Neurosci. Lett.*, vol. 532, no. 1, pp. 1–6, Jan. 2013, doi: 10.1016/J.NEULET.2012.10.019.
- [216] C. A. Walleck, "Preventing secondary brain injury," *AACN Clin. Issues Crit. Care Nurs.*, vol. 3, no. 1, pp. 19–30, Feb. 1992, doi: 10.4037/15597768-1992-1003.
- [217] S. Gyoneva and R. M. Ransohoff, "Inflammatory reaction after traumatic brain injury: therapeutic potential of targeting cell-cell communication by chemokines," *Trends Pharmacol. Sci.*, vol. 36, no. 7, pp. 471–480, Jun. 2015, doi: 10.1016/J.TIPS.2015.04.003.
- [218] C. MacKs, D. Jeong, and J. S. Lee, "Therapeutic efficacy of rolipram delivered by Pgp nanocarrier on secondary injury and motor function in a rat TBI model," <https://doi.org/10.2217/nnm-2021-0271>, vol. 17, no. 7, pp. 431–445, Feb. 2022, doi: 10.2217/NNM-2021-0271.
- [219] C. Nakamura *et al.*, "Rolipram, a specific type IV phosphodiesterase inhibitor, ameliorates indomethacin-induced gastric mucosal injury in rats," *Pathophysiology*, vol. 9, no. 3, pp. 195–200, 2003, doi: 10.1016/S0928-4680(03)00005-1.
- [220] K. J. Kelly *et al.*, "Minocycline inhibits apoptosis and inflammation in a rat model of ischemic renal injury," *Am. J. Physiol. Renal Physiol.*, vol. 287, no. 4, 2004, doi: 10.1152/AJPRENAL.00050.2004.